Applied Computational Electromagnetics Society

Journal

March 2012

Vol. 27 No. 3

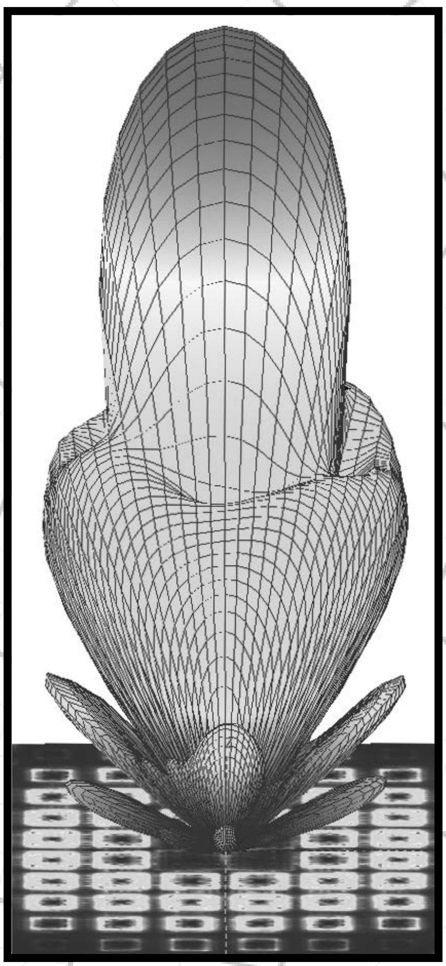

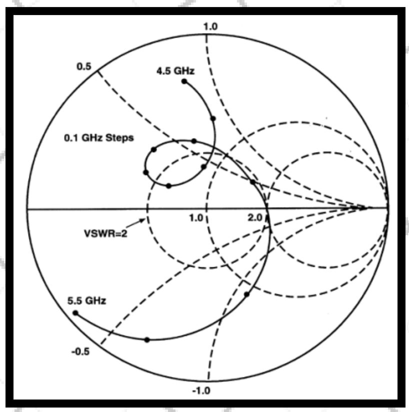

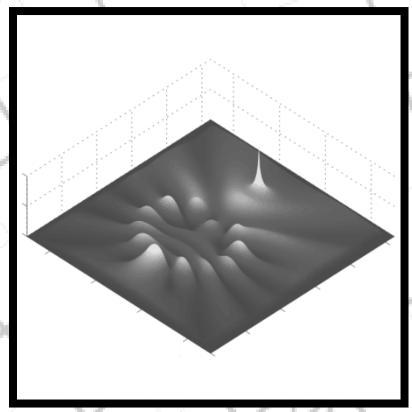

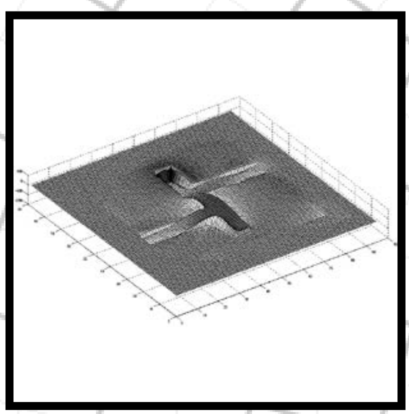

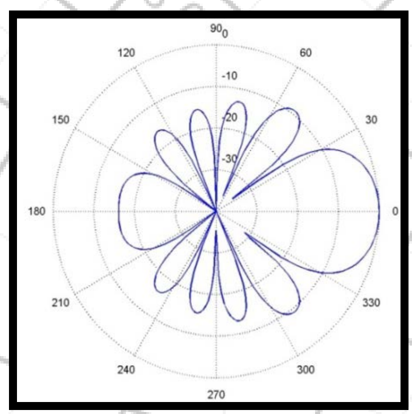

ISSN 1054-4887

GENERAL PURPOSE AND SCOPE: The Applied Computational Electromagnetics Society ***(ACES)*** Journal hereinafter known as the ***ACES Journal*** is devoted to the exchange of information in computational electromagnetics, to the advancement of the state-of-the art, and the promotion of related technical activities. The primary objective of the information exchange is to inform the scientific community on the developments of new computational electromagnetics tools and their use in electrical engineering, physics, or related areas. The technical activities promoted by this publication include code validation, performance analysis, and input/output standardization; code or technique optimization and error minimization; innovations in solution technique or in data input/output; identification of new applications for electromagnetics modeling codes and techniques; integration of computational electromagnetics techniques with new computer architectures; and correlation of computational parameters with physical mechanisms.

SUBMISSIONS: The ***ACES Journal*** welcomes original, previously unpublished papers, relating to applied computational electromagnetics. Typical papers will represent the computational electromagnetics aspects of research in electrical engineering, physics, or related disciplines. However, papers which represent research in applied computational electromagnetics itself are equally acceptable.

Manuscripts are to be submitted through the upload system of ***ACES*** web site http://aces.ee.olemiss.edu See "Information for Authors" on inside of back cover and at ***ACES*** web site. For additional information contact the Editor-in-Chief:

Dr. Atef Elsherbeni
Department of Electrical Engineering
The University of Mississippi
University, MS 386377 USA
Phone: 662-915-5382
Email: atef@olemiss.edu

SUBSCRIPTIONS: All members of the Applied Computational Electromagnetics Society are entitled to access and download the ***ACES Journal*** any published journal article available at http://aces.ee.olemiss.edu. Printed issues of the ***ACES Journal*** are delivered to institutional members. Each author of published papers receives a printed issue of the ***ACES Journal*** in which the paper is published.

Back issues, when available, are $50 each. Subscription to ***ACES*** is through the web site. Orders for back issues of the ***ACES Journal*** and change of address requests should be sent directly to ***ACES*** office at:

Department of Electrical Engineering
The University of Mississippi
University, MS 386377 USA
Phone: 662-915-7231
Email: aglisson@olemiss.edu

Allow four weeks advance notice for change of address. Claims for missing issues will not be honored because of insufficient notice, or address change, or loss in the mail unless the ***ACES*** office is notified within 60 days for USA and Canadian subscribers, or 90 days for subscribers in other countries, from the last day of the month of publication. For information regarding reprints of individual papers or other materials, see "Information for Authors".

LIABILITY. Neither ***ACES***, nor the ***ACES Journal*** editors, are responsible for any consequence of misinformation or claims, express or implied, in any published material in an ***ACES Journal*** issue. This also applies to advertising, for which only camera-ready copies are accepted. Authors are responsible for information contained in their papers. If any material submitted for publication includes material which has already been published elsewhere, it is the author's responsibility to obtain written permission to reproduce such material.

APPLIED COMPUTATIONAL ELECTROMAGNETICS SOCIETY JOURNAL

March 2012
Vol. 27 No. 3
ISSN 1054-4887

The ACES Journal is abstracted in INSPEC, in Engineering Index, DTIC, Science Citation Index Expanded, the Research Alert, and to Current Contents/Engineering, Computing & Technology.

The illustrations on the front cover have been obtained from the research groups at the Department of Electrical Engineering, The University of Mississippi.

MARCH 2012 REVIEWERS

Ahmed Abdelrahman
Robert Adams
Shirook Ali
Ayman Al-Zayed
Manuel Arrebola
Mohamed Bakr
Sami Barmada
Bevan Bates
Zikri Bayraktar
Ahmed Boutejdar
M. do Rosario Calado
Jiefu Chen
Jingyi Chen
William Coburn
Khaled El Mahgoub
Jieran Fang
Mohammed Hadi
Amir Hajiaboli
Dimitra Kaklamani
Yasushi Kanai
Nikolaos Kantartzis
Fadi Khalil
Zulfiqar Khan
Fadi Khalil
Zulfiqar Khan
Sebastien Lallechere
Yingsong Li
Mingy Lu
Alireza Mallahzadeh
Sean Mercer
Mojtaba Mighani
Yoginder Negi
Jiaran Qi
C. J. Reddy
Luca Rienzo
Cesar Mendez Ruiz
Antonio Espirito Santo
Dennis Schobert
Harvey Schuman
Abbas Shiri
Yuan Sun
Hossein Torkaman
Nikolaos Tsitsas
Shaoqiu Xiao
Hao Xin
Amir Zaghloul
Huapeng Zhao

THE APPLIED COMPUTATIONAL ELECTROMAGNETICS SOCIETY

JOURNAL

Vol. 27 No. 3 March 2012

TABLE OF CONTENTS

Cepstral Analysis of Photonic Nanojet-Illuminated Biological Cells

César Méndez Ruiz and Jamesina J. Simpson

Department of Electrical and Computer Engineering
University of New Mexico, Albuquerque, NM 87131 USA
cesar.mendez.ruiz@gmail.com, simpson@ece.unm.edu

Abstract ─ It is currently believed that nanometer-scale internal refractive index fluctuations within biological cells change significantly during the initial stages of ultra early-stage cancer development well in advance of these changes becoming more pronounced and histologically detectable. Here, backscattered cepstral results of photonic nanojet-illuminated cells are investigated as a means to offer unique advantages for determining the internal structure and composition of cells at sub-diffraction (nanometer) scales. Specifically, the finite-difference time-domain (FDTD) method is employed to obtain the backscattered cepstrum of photonic-nanojet illuminated human colorectal HT-29 cells. Analysis of the backscattered cepstrum of the HT-29 cells indicates a clear means to distinguish between cells having larger and smaller levels of internal refractive index fluctuations before these changes are histologically detectable. Further, we find that the surface reflection is reduced for the case of nanojet-illuminated cells compared to flat surfaces.

Index Terms ─ Biological media, cancer, cepstrum, FDTD, photonic nanojet.

I. INTRODUCTION

As reported in a 2008 article of the *Proceedings of the National Academy of Sciences* [1], internal refractive index fluctuations are believed to change significantly on a nano-meter scale within biological cells during the initial stages of ultra early-stage cancer development well in advance of these changes becoming more pronounced and histologically detectable. In other words, cellular changes at the nano-meter scale, the scale of some of the fundamental building blocks of cells (such as ribosomes, macromolecular complexes nuceleosomes, membranes, etc.), are expected to be occurring during cancer development in advance of changes at the micro-meter scale. For example, a less aggressive human colorectal cancer cell line (HT-29) is hypothesized in [1] to have 60×60×60 nm correlation lengths, while a more aggressive HT-29 colon cancer cell line is hypothesized to have a correlation length of 600×600×100 nm. In the case of [1], the mean refractive index n_0 of the HT-29 cell is set to 1.38, and the maximum refractive index fluctuation (Δn_{max}) is 0.02.

In this paper, HT-29 cells are analyzed in a new way for determining the characteristics of their internal refractive index fluctuations. Specifically, the backscattered cepstrum is obtained for photonic nanojet-illuminated HT-29 cells. This technique of employing the cepstrum as well as a photonic nanojet offers new advantages through unique capabilities for determining the internal structure and composition of cells at sub-diffraction scales. Further, an important advantage of the technique of this paper is that the surface reflection is reduced for cells compared to flat surfaces. This work may thus have application to ultra-early stage cancer detection.

The cepstrum is defined here as taking the discrete Fourier transform (DFT) of the magnitude of the backscattered spectrum:

$$f(t) \rightarrow DFT \rightarrow spectrum$$

$$abs(spectrum) \rightarrow DFT \rightarrow cepstrum$$

The domain of the cepstrum is termed “quefrency” and integer multiples of the fundamental quefrency are termed “rahmonics” [2]. Note that although the units of the

Submitted On: Dec 1, 2011
Accepted On: Feb. 23, 2012

independent variable for the cepstrum is seconds, the cepstrum exists neither in the frequency nor time domain. As for the coining in [2] of the word "cepstra," these terms are formed by reversing the order of the initial letters of their corresponding terms in the frequency domain.

The cepstrum is useful because it permits an analysis of the rate of change and periodicity of the spectrum over the complete frequency range of interest. Let us consider for example a simple recorded backscattered time waveform comprised of multiple reflected pulses having different delays and amplitudes:

$$x(t) = s(t) + \alpha_1 s(t-\tau_1) + \alpha_2 s(t-\tau_2) + \ldots + \alpha_{n_\tau} s(t-\tau_{n_\tau}),$$

where τ_n is the delay of the n$^{\text{th}}$ reflection ($\tau_1 < \tau_2 < \ldots < \tau_{n\tau}$), and the α's account for the scaling of the reflections from embedded features within the target as well as the shadow side surface of the target with respect to the magnitude of the reflection from the illuminated side of the target.

The spectrum magnitude of this signal is:

$$|X(f)| = |S(f)| \sqrt{1 + \sum_{i=1}^{n_\tau} \alpha_i^2 + 2\left\{ \sum_{i=1}^{n_\tau} \alpha_i \cos(2\pi\tau_i f) + \sum_{i=1}^{n_\tau - 1} A_i \right\}},$$

where

$$A_i = \alpha_i \alpha_{i+1} \cos\left(2\pi\left[\tau_{i+1} - \tau_i\right] f\right) + \alpha_i \alpha_{i+2} \cos\left(2\pi\left[\tau_{i+2} - \tau_i\right] f\right) + \ldots + \alpha_i \alpha_{n_\tau} \cos\left(2\pi\left[\tau_{n_\tau} - \tau_i\right] f\right)$$

In this case, the cepstrum will be comprised of one peak per feature of the target generating a reflection (each internal feature as well as the shadow-side surface of the target). Each of these cepstral peaks will be located along the x-axis (quefrequency, in units of seconds) at the position corresponding to the difference in round-trip propagation time between the initial reflection from the incident surface of the target and the corresponding reflection from the internal feature / shadow side surface of the target. The magnitudes of all but the last cepstral peak are affected by multiple α values.

A photonic nanojet is defined as a narrow, high-intensity beam of light that emerges from the shadow side of a plane-wave-illuminated dielectric sphere or cylinder of diameter larger than the wavelength, λ [3]. Photonic nanojets have previously been shown to provide sufficiently one-dimensional (1-D) illumination of three-dimensional (3-D) targets [4], yielding the ability to detect at distances of multiple wavelengths in the backscatter direction ultra-subwavelength inhomogeneities embedded within the dielectric targets [4].

In this paper, the cepstral analysis of [4] developed for flat, dielectric slabs is applied to the more complex scenario of HT-29 cells. Here, the backscattered cepstrum is chosen for analysis over the spectrum curve because the target's characteristics are more easily extracted from the cepstral curve than from the periodic backscattered spectrum. Compared to [4], the modeling of this paper is complicated by the surface roughness and overall curvature of the HT-29 cell, as well as by the random internal refractive index fluctuations within the cells. Specifically, the finite-difference time-domain (FDTD) method [5] is employed to obtain the backscattered cepstrum of homogeneous and inhomogeneous HT-29 cells. The 3-D FDTD grids model HT-29 cells, including their surface topography using data from atomic force microscopy (AFM) measurements [6], along with a microsphere for generating the nanojet used to illuminate the HT-29 cells. Analysis of the backscattered cepstrum of the different modeling cases indicates that (1) details of the internal composition of cells are more easily extracted from the backscatter of nanojet-illuminated cells than flat slabs; this could mean detection of smaller and earlier changes in internal refractive index fluctuations; (2) a clear means exists to distinguish between cells having larger and smaller levels of internal refractive index fluctuations before these changes are histologically detectable.

II. 3-D FDTD MODEL DESCRIPTION

First, a healthy HT-29 cell is modeled in the FDTD grid by importing AFM measurement data [6]. AFM can resolve surface fluctuations of lengths on the order of fractions of a nanometer, which is more than 1000 times better than the best resolution obtained using diffraction limited optical systems. Figure 1 illustrates a top-down view of the topography of the HT-29 cell that is imported to the FDTD model. The HT-29 cell is modeled as being submerged in water, which permits studying living cells instead of dehydrated cells. Note that it is modeled here as being stationary in the FDTD grid.

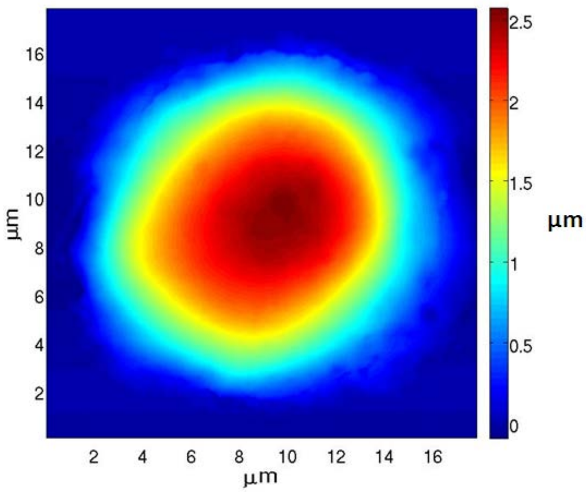

Fig. 1. AFM surface topography of a fixed human colorectal HT-29 cell, courtesy of Dr. Richter [6]. 512 sampling points are collected in each direction over a 17.8 by 17.8 µm area providing a resolution of ~3.48 nm Nanowizard II (JPK Instruments AG, Germany), uncoated NSG10 tip (NT-MDT, Russia).

Next, a 1.5-µm diameter silica sphere having a refractive index n of 1.42 is modeled in a FDTD grid. This microsphere produces a photonic nanojet as shown in Fig. 2 that is later used to probe the HT-29 cell of Fig. 1. Note that the microsphere is also submerged in water, leading to an entire microsphere-HT-29 cell system that is submerged in water. Submerging the nanojet-generating microsphere improves the length of the nanojet and also reduces unintended resonances inside the sphere due to the lower refractive index contrast of the silica sphere with water rather than free space.

In subsequent simulations, the sphere center is located 950 nm from the top (incident side) surface of the HT-29 cell. A total-field scattered-field FDTD formulation [5] is employed to illuminate the microsphere with a plane wave, which then yields the nanojet for probing the HT-29 cell. For each simulation case, the backscattered time-waveform is recorded 3.8 µm on the incident side of the microsphere for subsequent post-processing. Note that as part of the post-processing, the time-domain backscatter from the microsphere alone is subtracted from case of the microsphere plus HT-29 cell case. This permits better extraction of the backscattered signal from the HT-29 cell.

Finally, the FDTD grid unit cell size is set to 10 nm in each Cartesian direction. This value is chosen not based on the Courant limit [5], but rather from the fine details of the cell surface topography. The spacing between measuring points (in x and y directions) in the provided AFM traces is 34.8 nm, but the vertical (z-direction) resolution of AFM is on the order of fractions of a nanometer. As such, starting with a grid cell size of 30 nm, iterative FDTD simulations involving the nanojet and the homogeneous HT-29 cell (n_0 = 1.38) while using progressively smaller FDTD grid cell sizes were run until convergence of the backscattered waveform was achieved at a grid resolution of 10 nm.

III. FDTD MODELING RESULTS

A. Homogeneous case

First, the HT-29 cell of Fig. 1 is modeled as having a homogeneous permittivity of 1.38 and as being illuminated by the nanojet of Fig. 2 at its geometric center. Note from Fig. 1 that the geometric center of the cell does not correspond to its peak thickness, which is slightly off-center and to the upper right of the central point. Also, the cell AFM topography is modeled only on the front side of the illuminated cell, and the shadow-side surface of the cell is modeled as being flat. Although modeling the two-sided surface topography of the HT-29 cell would be more realistic, here, having a flat shadow side HT-29 cell provides a useful comparison of the effects of the front (AFM surface data) side and back (flat) sides of the cell on the backscattered signal.

Figure 3 illustrates the time-domain backscattered waveform of the nanojet-illuminated HT-29 cell. Also shown for comparison is the backscattered waveform of a homogeneous slab of the same n and same average thickness as the HT-29 cell (as measured from Fig. 1 only over the transverse circular area of the cell illuminated by the nanojet). The results of Fig. 3 show for both the cell / slab cases two pulses occurring together in time, and representing the reflections from the front and back sides of the cell / slab. Since the shadow-side surface of both the cell and the slab are flat, the second pulses are nearly identical for both cases. The earlier reflection from the front side, however, indicates a lower amplitude reflection from the cell compared to that of the slab. This is due to the surface topology and roughness of the cell, which scatters the incident wave in more directions than just directly backward as is the case for the flat slab.

As a result, from the results of Fig. 3, we find that an important advantage of the technique of this paper involving nanojets and the analysis of backscattered waveforms from biological cells, is that the surface reflection is reduced for cells compared to flat surfaces. This means that inhomogeneities within HT-29 cells, for example, such as internal refractive index fluctuations hypothesized to occur during the initial stages of cancer development, are more easily detectable in HT-29 cells compared to flat slabs, since the surface reflections of the cells are reduced in the backscattered direction. Further, cells having rougher or more drastically curved surfaces will permit even better detection of the internal composition of the cells. We note that a question not addressed in [1] is whether early-stage cancer is detectable by characterizing changes in the surface topology of biological cells rather than or in addition to the internal refractive index changes [7]. The technique of this paper could help answer this question.

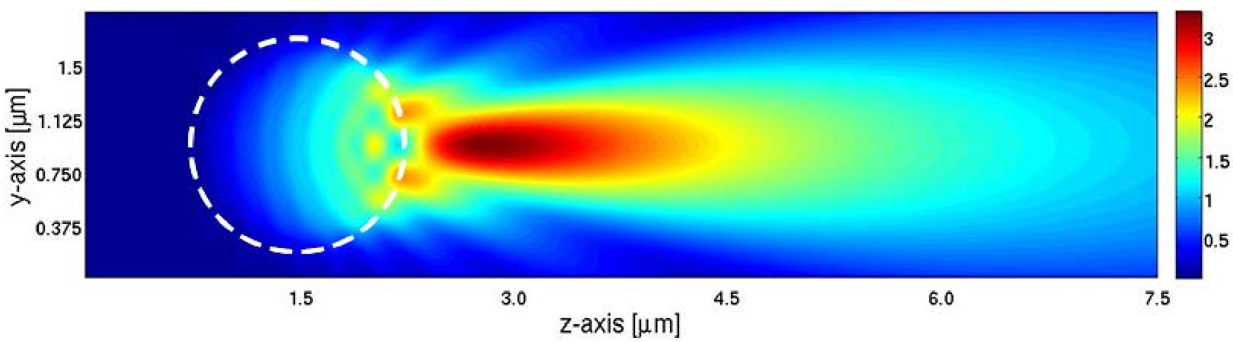

Fig. 2. Visualization of a photonic nanojet generated by a plane-wave-illuminated, 1.5-μm diameter silica microsphere submerged in water. The single frequency incident light λ is 500 nm. The steady-state electric field amplitude is plotted.

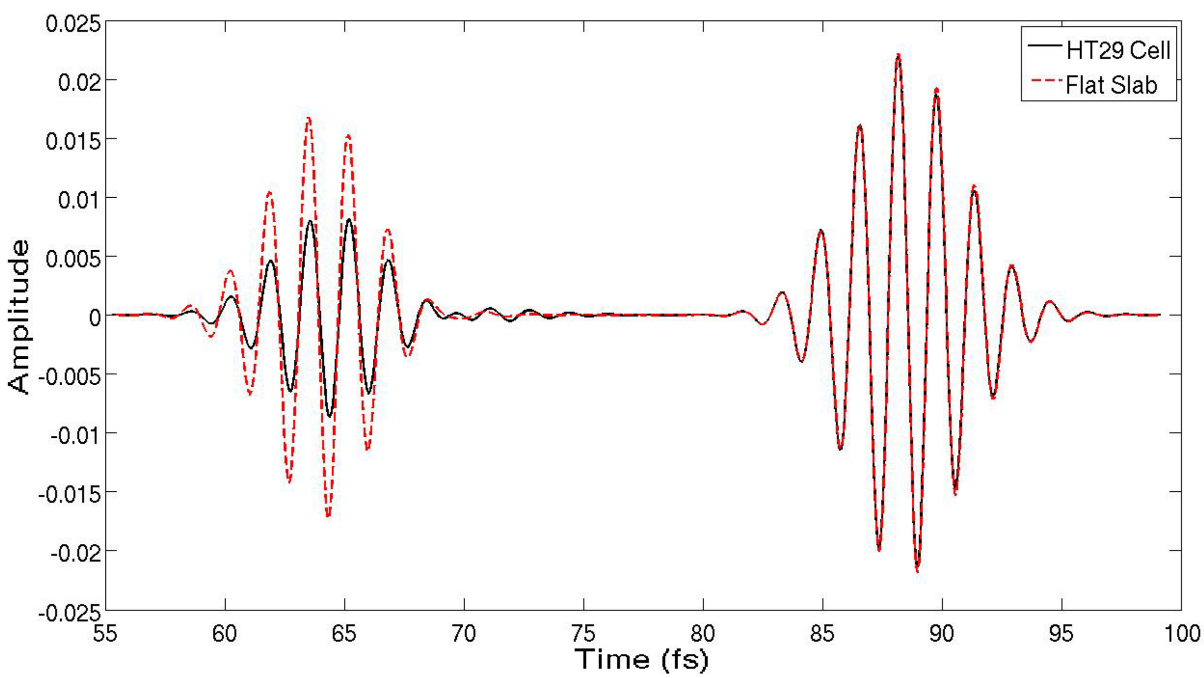

Fig. 3. Recorded time-domain backscatter from the HT-29 cell, and a dielectric slab having the same *n* and average thickness. The source is a Gaussian of half-width 3.18 fs modulating a sinusoid at 500 nm center wavelength.

B. Inhomogeneous case

Next, the HT-29 cell is modeled as having a pseudorandom *n* pattern. Fluctuations of the *n* inside of cells can arise due to varying concentrations of intracellular solids like DNA, RNA, lipids, etc. As a result, here, the intra cellular solids of the biological cell are modeled as a stationary process in the second-order cumulant approximation [8], as was done in the work of [1]. For this approximation, the *n* is determined to vary randomly with position but is held constant (homogeneous) within each block of dimension equal to a parameter termed the correlation length, *lc*. That is, the correlation function (the correlation between random variables, in this case refractive index values, at positions in space and as a function of the spatial distance between those two points) is defined by

$$\gamma(r) = \left\langle n(r_i) \cdot n(r_j) \right\rangle_r / \left\langle n^2 \right\rangle$$

where $\left\langle n^2 \right\rangle$ denotes the mean-square average of the fluctuation of the refractive index and $\left\langle n(r_i) \right\rangle$ and $\left\langle n(r_j) \right\rangle$ are the fluctuations of the refractive index at *i* and *j* positions that are a distance *r* apart. The correlation function varies from 0 when *r* is very large to 1 when *r*=0. For a random distribution of refractive index values, the correlation function can be approximated by [9]:

$$\gamma(r) = \exp\left(\frac{-r}{l_c}\right).$$

In our case, the value of *n* for each homogeneous block is determined pseudorandomly, and we choose to investigate the effects of different size blocks similar to those considered in [1]. Specifically, the *lc* value corresponds to the size of the intracellular structures within a cell, and is currently hypothesized to correlate with the cancer aggressiveness level of the cell [1]. As a result, the *lc* value is changed for the different HT-29 cells corresponding to different levels of cancer development. On the other hand, the maximum *n* variations (Δn) is proportional to the local concentration of intracellular solids. Here, for all simulation cases, the mean refractive index n_o is equal to 1.38 as in [1]. The Δn for typical biological tissue can range from 0.02 to 0.1 [10]; for this work, the maximum Δn is set to 0.1. Figure 4 shows an example 2-D geometry slice of a 3-D FDTD grid for the case of the HT-29 cell filled with 60×60×60 nm *n* blocks, along with the microsphere for generating the nanojet.

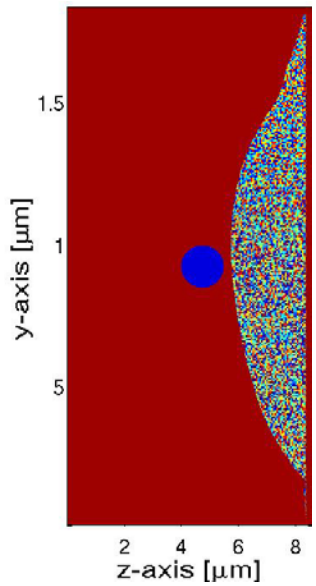

Fig. 4. 2-D slice of the geometry of the silica microsphere for generating the nanojet along with the HT-29 cell having a 60×60×60 nm pseudorandom *n* pattern.

Note that to date (as mentioned at the end of Section 3A), a systematic study of any changes possibly occurring in the cell topography during cancer development has not yet been performed. As a result, we also assume here for the inhomogeneous HT-29 cells corresponding to different levels of cancer aggressiveness the same cell topography obtained for a healthy HT-29 cell and used in Section 3A. This is because AFM topography data for HT-29 cells at different levels of cancer aggressiveness is not readily available. But we note that obtaining such data would be an important part of future work in order to understand what important changes, if any, are occurring at the cell surface during advancement of the cancer.

In the first of two studies involving random *n* fluctuations within HT-29 cells, the sensitivity of the backscatter signal due to different *lc* values is tested. Specifically, separate FDTD simulations are run involving nanojet-illuminated HT-29 cells having a pseudorandom *n* composition with homogeneous block sizes of 600×600×100 nm, 60×60×60 nm, 30×30×30 nm, and 10×10×10 nm.

The resulting cepstral curves for each case are shown in Fig. 5.

In general, the magnitude of the cepstrums in Fig. 5 indicates that a decrease of the *lc* leads to a reduction of the total backscattered energy from the cell, especially for quefrequencies above 0 fs corresponding to the initial reflection from the incident-side surface of the cell. That is, the quefrency corresponds to the delay time between the initial reflection (at 0 fs) and subsequent reflections, so a reduction between the different pseudorandom *n* cases of the magnitude between 0 and 25 fs indicates less reflection from the internal *n* blocks (a directly backscattered reflection from the shadow-side surface would occur at 25 fs). In fact, as we may expect, as the *n* blocks reduce in size, the cepstral curve converges to the case of the cell being completely homogeneous. Before this convergence, however, Fig. 5 indicates that *n* blocks as small as about 30 nm can be detected in the cepstral curve, demonstrating the nanojet's potential to detect the fundamental "building blocks" of biological cells (nucleosomes, protein complexes, cytoskeleton, etc.) that have been experimentally shown to be on the order of ~100 nm or less [1].

The maximum magnitude variation of the *n* inside the biological cell is a constant that does not depend on how advanced the carcinogenesis stage is; what determines the aggressiveness of a cell line and distinguishes it from other lines is the value of *lc* [1]. As such, in the second study involving random *n* fluctuations within HT-29 cells, two cases of cell lines are considered. One is the C-terminal Src kinase (Csk) knockdown that is represented with 600×600×100 nm rectangular homogeneous *n* blocks. The other case is the epidermal growth factor receptor (EGFR) knockdown which is less aggressive and is represented with 60×60×60 nm *n* blocks [1]. The cepstral curves from three different pseudorandom patterns per cell line are shown in Fig. 6.

In general, the more aggressive cell line (CsK) backscatters more energy than the EGFR line, but above 5 fs it is insufficient to examine the cepstral curves and unambiguously distinguish between the two cell lines. On the other hand, for all six cases, it is possible to distinguish one cell line from the other based on the magnitude at quefrency 0 fs (higher magnitudes for all three CsK cases, and lower magnitudes for all three EGFR cases). This indicates the possibility of using a cepstral analysis of the backscatter from nanojet-illuminated cells to determine the aggressiveness of cancer cells at sub-diffraction scales and before the disease provokes alterations detectable using histological techniques.

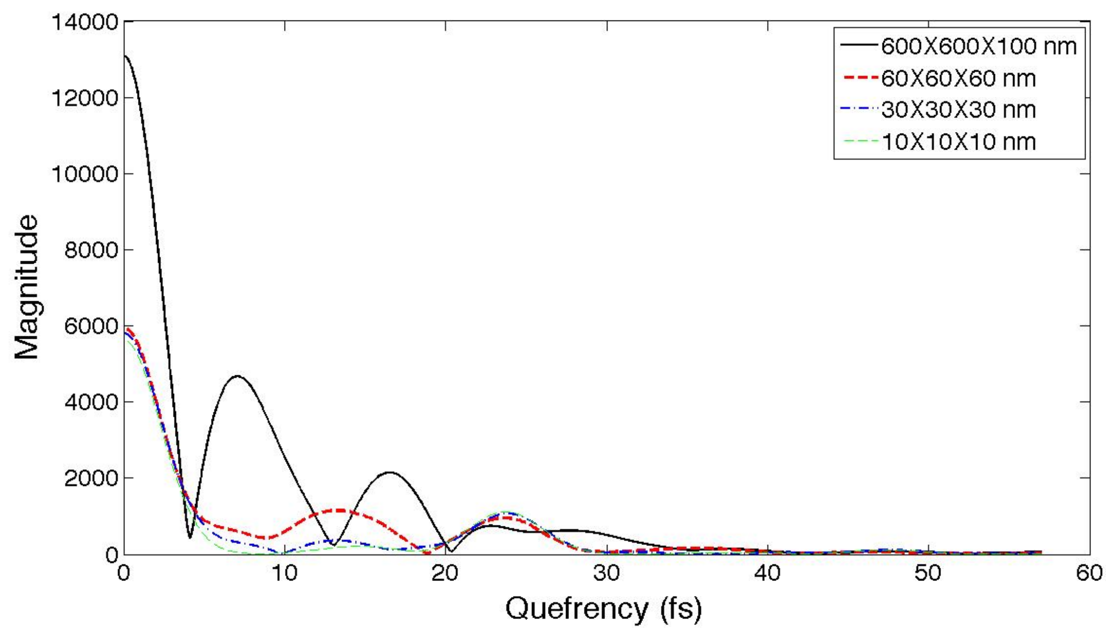

Fig. 5. Comparison of cepstral curves for HT-29 cells having n blocks of different sizes. The homogeneous case is not shown because it is a perfect match with the 10×10×10 nm blocks.

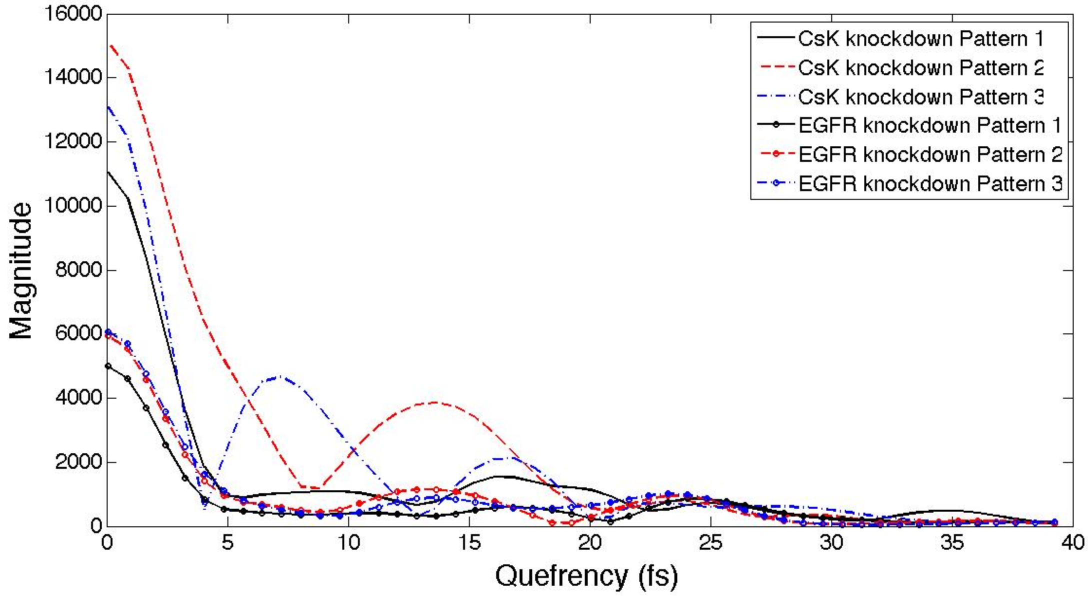

Fig. 6. Comparison of cepstral curves from CsK and EGFR cell lines. Results for three pseudorandom internal *n* fluctuation patterns are shown for each cell line.

Note again that the magnitudes at quefrequency 0 fs in all the figures of this paper, including Fig. 6, correspond to the reflection from the incident surface of the cell, whereas the larger quefrequency values correspond to later reflections involving the internal fluctuations within the cells.

IV. CONCLUSIONS AND ONGOING WORK

Analysis of the backscattered cepstrum of the photonic nanojet-illuminated HT-29 cells has demonstrated that (1) details of the internal composition of cells are more easily extracted from the backscatter of nanojet-illuminated cells than flat slabs; this could aid the detection of smaller and earlier changes in the internal refractive index fluctuations; (2) a clear means exists to distinguish between cells having larger and smaller levels of internal refractive index fluctuations before these changes are histologically detectable.

The study presented in this paper relates to a wide variety of other work being performed by other groups involving the interaction of electromagnetic waves with biological tissues and cells [11 – 13].

As part of future work, laboratory measurements will be conducted to support the computational results of this paper. This will include comprehensive AFM measurements of HT-29 cells at different stages of cancer development in order to help address the question not answered in [1]: whether early-stage cancer is detectable by characterizing changes in the surface topology of biological cells rather than or in addition to the internal refractive index changes. The use of photonic nanojets and the cepstrum may be particularly useful in answering this question, since changes in the surface topography from flatter and smoother to more curved and rough provides noticeably better detection of the internal composition of the cells.

ACKNOWLEDGMENT

This work was supported by the Engineering Research Centers Program of the National Science Foundation under NSF Cooperative Agreement No. EEC-0812056. Also, CONACYT Fellowship number 304287 supported author C. Méndez Ruiz’s (209576) graduate studies. Supercomputing resources were provided by the New Mexico Computing Applications Center and the University of New Mexico’s Center for Advanced Research Computing (CARC).

REFERENCES

[1] H. Subramanian, P. Pradhan, Y. Liu, I. Capoglu, X. Li, J. Rogers, A. Heifetz, D. Kunte, H. Roy, A. Taflove, and V. Backman, "Optical Methodology for Detecting Histologically Unapparent Nanoscale Consequences of Genetic Alterations in Biological Cells," *Proc. Natl. Acad. Sci*., vol. 105, issue 51, pp. 20124-20129, 2008.

[2] B. P. Bogert, M. J. R. Healy, J. W. Tukey, and M. Rosenblatt, "The Quefrency Analysis of Time Series for Echoes: Cepstrum, Pseudo-Autocovariance, Cross-Cepstrum, and Saphe Cracking," *in Time Series Analysis*, M. Rosenblatt, Ed., ch. 15, pp. 209–243, 1963.

[3] A. Heifetz, S.-C. Kong, A. V. Sahakian, A. Taflove, and V. Backman, "Photonic Nanojets," *J. Computational & Theoretical Nanoscience*, vol. 6, pp. 1979-1992, Sept. 2009.

[4] C. Méndez Ruiz and J. J. Simpson, "Detection of Embedded Ultra-Subwavelength-Thin Dielectric Features using Elongated Photonic Nanojets," *Optics Express*, vol. 18, iss. 16, pp. 16805-16812, 2010.

[5] A. Taflove and S. C. Hagness, Computational Electrodynamics: The Finite-Difference Time-Domain Method, 3rd edition. Norwood, MA: Artech House, 2005.

[6] Personal communications with Dr. Marc Richter of the Institute of Photonic Technology in Jena, Germany.

[7] P. Pradhan, D. Damania, H. M. Joshi, V. Turzhitsky, H. Subramanian, H. K. Roy, A. Taflove, V. P. Dravid, and V. Backman, "Quantification of Nanoscale Density Fluctuations Using Electron Microscopy: Light-Localization Properties of Biological Cells," *Phys. Biol.*, vol. 8, issue 2, 2011.

[8] S.B. Haley and P. Erdos, "Wave-Propagation in One-Dimensional Disordered Structures," *Phys Rev B*, vol. 45, issue 15, pp. 8572–8584, 1992.

[9] P. Debye, H. R. Anderson, Jr., and H. Brumberger, "Scattering by an Inhomogeneous Solid. II. The Correlation Function and Its Application," *Journal of Applied Physics*, vol. 28, no. 6, pp. 679 – 683, 1957.

[10] J. M. Schmitt and G. Kumar, "Optical Scattering Properties of Soft Tissue: A Discrete Particle Model," *Appl. Opt.*, vol. 37, issue 13, pp. 2788-2797, 1998.

[11] D. A. Woten and M. El-Shenawee, "Quantitative Analysis of Breast Skin for Tumor Detection Using Electromagnetic Waves," *Applied Computational Electromagnetics Society (ACES) Journal*, vol. 24, no. 5, pp. 458 – 463, October 2009.

[12] M. A. Eleiwa and A. Z. Elsherbeni, "Debye Constants for Biological Tissues From 30 Hz to 20 GHz," *Applied Computational Electromagnetics Society (ACES) Journal*, vol. 16, no. 3, pp. 202 – 213, November 2001.

[13] S. Caorsi, E. Bermani, and A. Massa, "A Microwave Imaging Approach Based on Amplitude-Only Data for the Reconstruction of the Electromagnetic Field Induced in Biological Phantoms," *Applied Computational Electromagnetics Society (ACES) Journal*, vol. 16, no. 2, pp. 79 – 89, July 2001.

César Méndez Ruiz was born in México City, México, on June 1, 1980. He received the B.S. diploma in Electromechanical Engineering from the Universidad Panamericana, Zapopan, Jalisco, México, in 2003, the M.S. degree in Electronic Engineering from the Universidad de Guadalajara, Guadalajara, Jalisco, México, in 2007, and the Ph.D. degree in Electrical Engineering from the University of New Mexico, Albuquerque, NM, USA.

From 2002 to 2003, he was a trainee in Hewlett-Packard (HP). He has professional experience in R&D area working as a mechanical design engineer for HP and Best in Development and Technology (BDT). Currently he is employed at Intel Corporation, Guadalajara, Mexico.

Jamesina J. Simpson received the B.S. and Ph.D. degrees in Electrical Engineering from Northwestern University, Evanston, IL, in 2003 and 2007, respectively. As a graduate student, Dr. Simpson was a recipient of the National Science Foundation Graduate Research Fellowship and the IEEE AP-S and MTT-S Research Awards.

In 2007, Dr. Simpson joined the Electrical and Computer Engineering Department at the University of New Mexico – Albuquerque as a tenure-track Assistant Professor. Her research lab encompasses the application of the full-Maxwell's equations finite-difference time-domain (FDTD) method to model a wide variety of scientific and engineering applications. In 2010, Dr. Simpson received an NSF CAREER award.

An Efficient Laguerre-FDTD Algorithm for Exact Parameter Extraction of Lossy Transmission Lines

Wei Shao and Jia-Lin Li

Institute of Applied Physics
University of Electronic Science and Technology of China, Chengdu, 610054, China
weishao@uestc.edu.cn, jialinuestc@yahoo.com.cn

Abstract ─ This paper introduces a hybrid finite-difference time-domain (FDTD) method with weighted Laguerre polynomials to extract attenuation constants of lossy transmission lines. In the case of uniform lossy transmission lines, the complex variable compact two-dimensional (2-D) Laguerre-FDTD method is suitable for extracting attenuation constants exactly. To reduce memory requirements in this method, the divergence theorem is used to obtain a memory-efficient matrix equation. A lossy coplanar waveguide (CPW) example is presented to validate the accuracy and efficiency of the hybrid algorithm.

Index Terms ─ FDTD, Laguerre polynomials, memory reduction, skin depth.

I. INTRODUCTION

Although the finite-difference time-domain (FDTD) method has been widely used for electromagnetic simulation, it often results in a long solution time for the problems with fine grid division based on the Courant-Friedrichs-Lewy (CFL) stability condition [1-3]. In recent years, much attention has been paid to the unconditionally stable techniques, such as the alternating direction implicit (ADI) FDTD [4], Crank-Nicolson (CN) FDTD [5], Laguerre-FDTD [6], and locally one-dimensional (LOD) FDTD [7].

The Laguerre-FDTD method, based on weighted Laguerre polynomials and Galerkin's testing procedure, does not have to deal with time steps and separately computes the temporal and spatial variables. It may be much more efficient than the FDTD method with too many time steps to compute the solution. However, the Laguerre-FDTD method results in an implicit relation and has to perform the matrix inversion. Its memory storage requirements and computation time is dependent on the produced sparse matrix equation. Similar to the conventional FDTD case [8], an efficient Laguerre-FDTD method combined with a memory-reduced (MR) technique is introduced for electromagnetic modeling by substituting a Maxwell's divergence relationship into one of the curl difference equations [9-10].

In the past years, some numerical algorithms have been proposed to extract circuit parameters of lossy transmission lines [11-12]. To calculate more accurate results, an iterative process is applied to the compact 2-D Laguerre-FDTD method for the exact parameter extraction in this paper. A hybrid time-domain algorithm, which combines the MR Laguerre-FDTD method with the compact 2-D complex variable technique, analyzes a lossy coplanar waveguide (CPW). Starting from the three-dimensional (3-D) Maxwell's differential equations considering the divergence equation, the hybrid method analytically deals with the partial derivatives with respect to the propagation direction and time variable, respectively, and forms an implicit relation to obtain an order-marching scheme. Then, we use an iterative process with three steps for finding the exact solution of attenuation constants by using the compact 2-D complex variable technique.

II. THEORIES

A. A MR-Laguerre-FDTD algorithm with complex variables

In the conventional compact 2-D Laguerre-FDTD method [13], only a phase shift term $e^{-j_0\beta z}$ involved in the field expressions is not enough for

Submitted On: Nov. 28, 2011
Accepted On: Feb. 4, 2012

1054-4887

lossy lines because a spatial attenuation term $e^{-\alpha z}$ is ignored, where z, α and β are the wave propagation direction, attenuation constant and phase constant, respectively. In general, however, the attenuated field components must not only vary with (x, y, t), but vary with z. Taking the spatial attenuation along z into account, the fields $U(x,y,z,t)$ can be expressed as

$$U(x,y,z,t) = u(x,y,t) \cdot e^{-(\alpha + j_0\beta)z}. \tag{1}$$

If the partial derivative with respect to z is replaced with $-(\alpha + j_0\beta)$, taking e_x and h_x for example the 3-D differential Maxwell's equations yield

$$\frac{\partial e_x}{\partial t} = \frac{1}{\varepsilon}\left[\frac{\partial h_z}{\partial y} + (\alpha + j_0\beta) h_y - \sigma e_x\right], \tag{2}$$

$$\frac{\partial h_x}{\partial t} = \frac{1}{\mu}\left[-(\alpha + j_0\beta) e_y - \frac{\partial e_z}{\partial y}\right]. \tag{3}$$

The other four equations can be constructed in a similar way.

Because of the explicit appearance of $e^{-\alpha z}$ in (1), the degenerated complex field components are not the functions of z anymore. It is apparent that, for single mode propagation, the temporal variations of field components are exactly steady oscillations.

In charge-free regions, the divergence of $\boldsymbol{D}$ can be chosen to replace (2)

$$\nabla \cdot \boldsymbol{D} = \frac{\partial e_x}{\partial x} + \frac{\partial e_y}{\partial y} - (\alpha + j_0\beta) e_z = 0. \tag{4}$$

Since the Laguerre polynomials $L_n(t)$ are orthogonal with respect to the weighting function e^{-t}, an orthogonal set $\{\varphi_0, \varphi_1, \varphi_{2,} \cdots\}$ is chosen as the basis functions

$$\varphi_n(st) = e^{-st/2} L_n(st), \tag{5}$$

where $s > 0$ is a time scale factor. Using these entire-domain temporal basis functions, the electromagnetic fields $u(x,y,t)$ can be expanded as

$$\{u(x,y,t)\} = \sum_{n=0}^{N} \{u^n(x,y)\} \varphi_n(st). \tag{6}$$

The first derivative of field components $u(x,y,t)$ with respect to time t is [14]

$$\frac{\partial u(x,y,t)}{\partial t} = s\sum_{n=0}^{N}\left[\frac{u^n(x,y)}{2} + \sum_{\substack{k=0,\\ n>0}}^{n-1} u^k(x,y)\right]\varphi_n(st). \tag{7}$$

Using a Galerkin's testing procedure in time domain and central difference in space domain, and eliminating magnetic fields, with reference to [6], we get

$$\begin{aligned} &e_x^m|_{i,j} - e_x^m|_{i-1,j} + \frac{\Delta x_i}{\Delta y_j} e_y^m|_{i,j} - \frac{\Delta x_i}{\Delta y_j} e_y^m|_{i,j-1} \\ &\quad - \Delta x_i (\alpha + j\beta) e_z^m|_{i,j} = 0, \end{aligned} \tag{8}$$

$$\begin{aligned} &-C_x^h|_{i-1,j}\, e_y^m|_{i-1,j} + \left[\frac{1 + 2\sigma_{i,j}/(s\varepsilon_{i,j})}{C_x^e|_{i,j}}\right. \\ &\quad \left. + C_x^h|_{i-1,j} + C_x^h|_{i,j} + \frac{2(\alpha + j\beta)^2 \Delta\overline{x}_i}{s\mu_{i,j}}\right] e_y^m|_{i,j} \\ &\quad - C_x^h|_{i,j}\, e_y^m|_{i+1,j} + C_y^h|_{i-1,j}\, e_x^m|_{i-1,j} \\ &\quad - C_y^h|_{i-1,j}\, e_y^m|_{i-1,j+1} - C_y^h|_{i,j}\, e_x^m|_{i,j} \\ &\quad + C_y^h|_{i,j}\, e_x^m|_{i,j+1} + (\alpha + j\beta)\Delta\overline{x}_i C_y^h|_{i,j}\, e_z^m|_{i,j} \\ &\quad - (\alpha + j\beta)\Delta\overline{x}_i C_y^h|_{i,j}\, e_z^m|_{i,j+1} \\ &= 2(\alpha + j\beta)\Delta\overline{x}_i \sum_{k=0}^{m-1} h_x^k|_{i,j} - \frac{2}{C_x^e|_{i,j}} \sum_{k=0}^{m-1} e_y^k|_{i,j} \\ &\quad - 2\sum_{k=0}^{m-1}\left(h_z^k|_{i,j} - h_z^k|_{i-1,j}\right), \end{aligned} \tag{9}$$

$$\begin{aligned} &-C_x^e|_{i,j}\, C_x^h|_{i-1,j}\, e_z^m|_{i-1,j} - C_y^e|_{i,j}\, C_y^h|_{i,j-1} \\ &\quad \times e_z^m|_{i,j-1} + \left[1 + \frac{2\sigma_{i,j}}{s\varepsilon_{i,j}} + C_x^e|_{i,j}\, C_x^h|_{i,j}\right. \\ &\quad + C_x^e|_{i,j}\, C_x^h|_{i-1,j} + C_y^e|_{i,j}\, C_y^h|_{i,j} + C_y^e|_{i,j} \\ &\quad \left.\times C_y^h|_{i,j-1}\right] e_z^m|_{i,j} - C_x^e|_{i,j}\, C_x^h|_{i,j}\, e_z^m|_{i+1,j} \\ &\quad - C_y^e|_{i,j}\, C_y^h|_{i,j}\, e_z^m|_{i,j+1} - \frac{2(\alpha + j\beta)}{s\mu_{i-1,j}} \\ &\quad \times C_x^e|_{i,j}\, e_x^m|_{i-1,j} + \frac{2(\alpha + j\beta)}{s\mu_{i,j}} C_x^e|_{i,j}\, e_x^m|_{i,j} \\ &\quad - \frac{2(\alpha + j\beta)}{s\mu_{i,j-1}} C_y^e|_{i,j}\, e_y^m|_{i,j-1} \\ &\quad + \frac{2(\alpha + j\beta)}{s\mu_{i,j}} C_y^e|_{i,j}\, e_y^m|_{i,j} \\ &= -2C_x^e|_{i,j} \sum_{k=0}^{m-1}\left(h_y^k|_{i,j} - h_y^k|_{i-1,j}\right) + 2C_y^e|_{i,j} \\ &\quad \times \sum_{k=0}^{m-1}\left(h_x^k|_{i,j} - h_x^k|_{i,j-1}\right) - 2\sum_{k=0}^{m-1} e_z^k|_{i,j}, \end{aligned} \tag{10}$$

where

$$C_x^e\,|_{i,j} = \frac{2}{s\varepsilon_{i,j}\Delta\bar{x}_i}, \tag{11}$$

$$C_y^e\,|_{i,j} = \frac{2}{s\varepsilon_{i,j}\Delta\bar{y}_j}, \tag{12}$$

$$C_x^h\,|_{i,j} = \frac{2}{s\mu_{i,j}\Delta x_i}, \tag{13}$$

$$C_y^h\,|_{i,j} = \frac{2}{s\mu_{i,j}\Delta y_j}, \tag{14}$$

where, Δx_i and Δy_j are the lengths of the lattice edge where the electric fields are located; $\Delta\bar{x}_i$ and $\Delta\bar{y}_j$ are the distances between the adjacent center nodes where magnetic fields are located.

Compared with the traditional Laguerre-FDTD method, $e_x^m\,|_{i,j}$ in the MR form has a relationship only with adjacent four electric field components from (8), which results in a reduction of nonzero e_x element storage by four-ninth, and does not need to summate from order 0 to m-1.

Then, we have a matrix form equation

$$[A]\{e^m\} = \{g\} + \{\theta^{m-1}\}, \tag{15}$$

where, $\{e^m\} = \{e_x^m, e_y^m, e_z^m\}^{\mathrm{T}}$, $\{g\} = \{g_x, g_y, 0\}^{\mathrm{T}}$ is the excitation and $\{\theta^{m-1}\}$ is the summation of terms from orders 0 to m-1.

After obtaining $\{e_x^0, e_y^0, e_z^0\}^{\mathrm{T}}$, we can solve (8), (9) and (10) in an order-marching procedure recursively for the given α and β. Thus, we can obtain the time-domain electromagnetic fields from (5) and (6) from the calculation for the expansion coefficients.

B. Iterative process for parameter extraction

Based on the above Laguerre-FDTD equation (15), an iterative process for finding the exact attenuation constant α_{exact} of a lossy transmission line is suggested. The whole process has the following three steps.

Step One: Real-Variable Laguerre-FDTD Step. For a given phase constant β, set $\alpha = 0$, and then the complex-variable Laguerre-FDTD equations degenerate into the conventional real-variable Laguerre-FDTD equations. From [13], we can obtain an approximate attenuation constant α_{approx} corresponding to the given β. The late-time field distribution of the propagation mode is saved as the full-wave excitation in the next step to shorten the early-time period.

Step Two: *Complex-Variable Laguerre-FDTD Step*. For the same phase constant β, set $\alpha_{\text{guess}} = \alpha_{\text{approx}}$. If $\alpha_{\text{guess}} = \alpha_{\text{exact}}$, the late-time response will be a steady oscillation, i.e., its amplitude will keep constant. If $\alpha_{\text{guess}} < \alpha_{\text{exact}}$, the amplitude of the late-time response will decrease exponentially in time domain. If $\alpha_{\text{guess}} > \alpha_{\text{exact}}$, it increases exponentially. The phenomena, shown in Fig. 1, can be easily understood because the exponential variations in the late-time response's amplitude will compensate partly the insufficient or excessive losses made by α_{guess}.

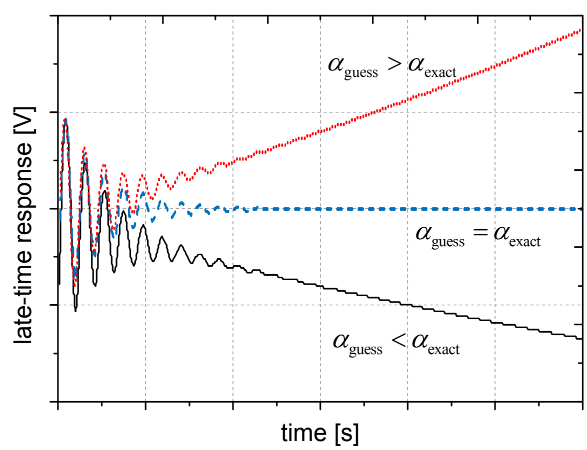

Fig. 1. Sketch of different late-time voltage responses for guessed attenuation constants.

In general, the late-time response's amplitude based on the 2-D Laguerre-FDTD equations will not keep constant. If the late-time response exponentially increases, that means $\alpha_{\text{approx}} > \alpha_{\text{exact}}$, and in this case we set $\alpha_{\min} = 0.5\alpha_{\text{approx}}$ and $\alpha_{\max} = \alpha_{\text{approx}}$. If the late-time response exponentially decreases, i.e., $\alpha_{\text{approx}} < \alpha_{\text{exact}}$, then we set $\alpha_{\min} = \alpha_{\text{approx}}$ and $\alpha_{\max} = 1.5\alpha_{\text{approx}}$. Thus, the search range $[\alpha_{\min}, \alpha_{\max}]$ for searching α_{exact} is determined.

Step Three: *Searching for* α_{exact}. For the same given β , a simple linear searching algorithm is combined with the proposed Laguerre-FDTD method to find α_{exact} between $\alpha_{\min}$ and $\alpha_{\max}$ iteratively. After several times of search, not more than twenty in general, the amplitude of the late-time response becomes constant, and the latest α is just the solution we want.

III. NUMERICAL EXAMPLE

In this example, the excitation source $\boldsymbol{J}$ is chosen as

$$\boldsymbol{J}(x,y,t) = \boldsymbol{g}(x,y)\delta(t)\,, \tag{16}$$

where the temporal variation of the excitation $\delta(t)$ is a Dirac pulse, and the spatial variation $\boldsymbol{g}(x,y)$ is a quasi-static finite-difference solution of the transverse electric fields in the transmission line.

Figure 2 shows the cross structure a lossy coplanar waveguide (CPW). The anisotropy of LiNbO3 substrate and the finite conductivity of Au are taken into consideration. The parameters of the CPW are $W = 10.4\mu\text{m}$, $G = 9.6\mu\text{m}$, $t = 4.4\mu\text{m}$, $d = 400\mu\text{m}$, $M = 200\mu\text{m}$, $\sigma = 4.1\times10^{7}\,\text{S/m}$, $\varepsilon_{\text{r}//} = 43$ and $\varepsilon_{\text{r}\perp} = 28$. The perfect electric conductors (PECs) are used as the peripheral boundary condition.

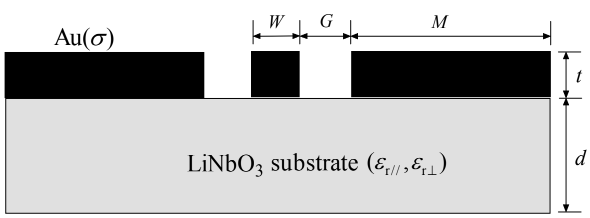

Fig. 2. Cross section of a lossy finite-ground CPW.

To consider the conductor loss in the CPW structure, the fields in conductors are analyzed and fine grid spacing is taken because of the influence of the skin depth. Graded grid division is adopted, and the minimum grid spacing is one-third of the skin depth corresponding to the maximum frequency f = 40GHz.

When only involving *Step One* of the whole three steps, the comparison of the computing time between the compact 2-D MR-Laguerre-FDTD method, conventional compact 2-D Laguerre-FDTD method and compact 2-D FDTD method for $\beta = 3.496$rad/cm is shown in Table 1. The two compact 2-D Laguerre-FDTD methods, which are free of stability constraint, show the significant improvement in computational efficiency. Moreover, the MR-Laguerre-FDTD method is more efficient than the conventional Laguerre-FDTD method because its memory storage of nonzero unknowns is reduced and 1/3 of electric field components do not need to summate from the order 0 to m-1. It is noted that it requires sixteen times of search to obtain the solution in *Step Three*.

Table 1: Comparison of the computing time when $\Delta x_{\min} = \Delta y_{\min} = 0.13\mu\text{m}$ and the whole lattice number is 51×27

Methods	**Total CPU time (s)**
MR-Laguerre-FDTD	213
Laguerre-FDTD	309
FDTD	945

The measured data in [15], numerical results with the compact 2-D Laguerre-FDTD method involving the whole three steps, and that only involving *Step One* is shown in Fig. 3, respectively. Compared with the results only involving *Step One*, the results with all three steps are in a better agreement with the measured data.

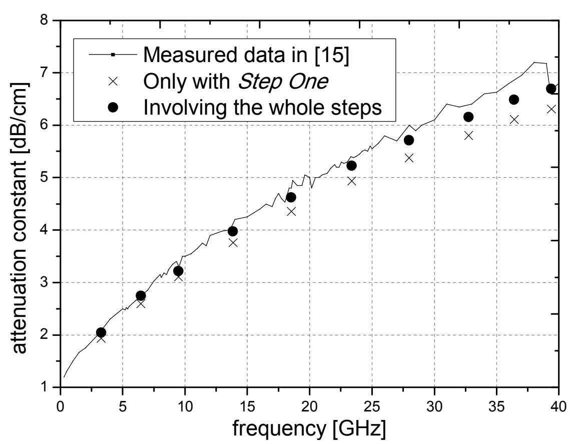

Fig. 3. Attenuation constants versus frequency for the lossy CPW.

IV. CONCLUSION

In this paper, an iterative process with complex variable technique is introduced for compact 2-D MR-Laguerre-FDTD method to analyze lossy transmission lines. With the divergence theorem, the memory storage of nonzero unknowns of e_x elements is reduced by 4/9 and 1/3 of electric field components do not need to summate from the order 0 to m-1. Under the condition of very fine grid spacing taken inside the lossy conductors, this unconditionally stable method shows improvement in computational efficiency compared with the FDTD method. Furthermore, an iterative process with complex variables is suggested to find the exact attenuation constants by using two additional steps, *Step Two* and *Step Three*. Although more CPU time is required, the hybrid method can obtain more accurate solutions than that only involving *Step One*, especially in the cases of heavily lossy lines.

ACKNOWLEDGMENT

This work was supported in part by the DPR Foundation of China (9140A03011210DZ0204 and 9140A21060211DZ0208), the Natural Science Foundation of China (60901023), and the Fundamental Research Funds for the Central Universities (ZYGX2010J043).

REFERENCES

[1] A. Taflove and S. C. Hagness, *Computational Electrodynamics: The Finite-Difference Time-Domain Method*, 2nd edition, Artech House, Boston, 2000.

[2] J. Chen and A. Zhang, "A Subgridding Scheme Based on the FDTD Method and HIE-FDTD Method," *Applied Computational Electromagnetics Society (ACES) Journal*, vol. 26, no. 1, pp. 1-7, 2011.

[3] F. L. Teixeira, "A Summary Review on 25 Years of Progress and Future Challenges in FDTD and FETD Techniques," *Applied Computational Electromagnetics Society (ACES) Journal*, vol. 25, no. 1, pp. 1-14, 2010.

[4] T. Namiki, "A New FDTD Algorithm Based on Alternating-Direction Implicit Method," *IEEE Trans. Microwave Theory and Tech.*, vol. MTT-47, pp. 2003-2007, 1999.

[5] A. P. Zhao, "More Accurate and Efficient Unconditionally Stable FDTD Method," *Electronic Letters*, vol. 39, pp. 862-863, 2002.

[6] Y.-S. Chung, T. K. Sarkar, B. H. Jung, and M. Salazar-Palma, "An Unconditionally Stable Scheme for the Finite-Difference Time-Domain Method," *IEEE Trans. Microwave Theory and Tech.*, vol. MTT-51, pp. 697-704, 2003.

[7] J. Shibayama, M. Muraki, J. Yamauchi, and H. Nakano, "Efficient Implicit FDTD Algorithm Based on Locally One-Dimensional Scheme," *Electronic Letters*, vol. 41, pp. 1046-1047, 2005.

[8] G. D. Kondylis, F. D. Flaviis, G. J. Pottie, and T. Itoh, "A Memory-Efficient Formulation of the Finite-Difference Time-Domain Method for the Solution of Maxwell Equations," *IEEE Trans. Microwave Theory and Tech.*, vol. MTT-49, pp. 1310-1320, 2001.

[9] W. Shao, B.-Z. Wang and T.-Z. Huang, "A Memory-Reduced 2-D Order-Marching Time-Domain Method for Waveguide Studies," *Journal of Electromagnetic Waves and Applications*, vol. 22, pp. 2523-2531, 2008.

[10] W. Shao, S.-J. Lai, and T. -Z. Huang, "Compact 2-D Full-Wave Order-Marching Time-Domain Method with a Memory-Reduced Technique," *Progress in Electromagnetics Research Letters*, vol. 6, pp. 157-164, 2009.

[11] T. Vaupel, "A Fast Spectral Domain Solver for the Characterization of Larger Microwave Structures in Multilayered Environments," *Applied Computational Electromagnetics Society (ACES) Journal*, vol. 24, no. 5, pp. 493-503, 2009.

[12] Y. W. Liu, D. S. Zhao, and K. K. Mei, "Implementation of Generalized Transmission - Line Equations to Transmission Line Parameter Extraction," *Applied Computational Electromagnetics Society (ACES) Journal*, vol. 18, no. 1, pp. 58-64, 2003.

[13] W. Shao, B.-Z. Wang, X.-H. Wang, and X.-F. Liu, "Efficient Compact 2-D Time-Domain Method with Weighted Laguerre Polynomials," *IEEE Trans. Electromagn. Compat.*, vol. EMC-48, pp. 442-448, 2006.

[14] I. S. Gradshteyn and I. M. Ryzhik, *Table of Integrals, Series, and Peoducts*, Academic New York, 1980.

[15] G. Ghione, M. Goano, G. Madonna, G. Omegna, M. Pirola, S. Bosso, D. Frassati, and A. Perasso, "Microwave Modeling and Characterization of Thick Coplanar Waveguides on Oxide-Coated Litheium Niobate Substrates for Electrooptical Applications," *IEEE Trans. Microwave Theory and Tech.*, vol. MTT-47, pp. 2287-2293, 1999.

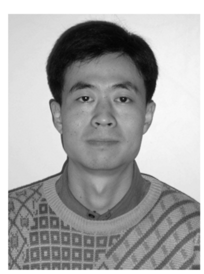

Wei Shao received the M.Sc. degree and Ph.D. degrees in Radio Physics from the University of Electronic Science and Technology of China (UESTC), Chengdu, China, in 2004 and 2006, respectively.

He joined the UESTC and is now an associate professor there. He has been a Visiting Scholar in the Electromagnetic Communication Laboratory, Pennsylvania State

University in 2010. His research interests include the computational electromagnetics, microwave passive components, and antenna technique.

Jia-Lin Li received the M.Sc. degree from UESTC, Chengdu, China, in 2004, and the Ph.D. degree from the City University of Hong Kong, Hong Kong, in 2009, both in Electronic Engineering. Since Sept. 2009, he has been with the Institute of Applied Physics, School of Physical Electronics, UESTC, where he is currently a Professor. His research interests include the computational electromagnetics, and high performance active/passive microwave/ millimeter-wave antennas, circuits and systems.

Smoothed Particle Electromagnetics Modelling on HPC-GRID Environment

Guido Ala[1] and Elisa Francomano[2]

[1] Dipartimento di Ingegneria Elettrica, Elettronica,Telecomunicazioni, di Tecnologie Chimiche, Automazione e Modelli Matematici
Università degli Studi di Palermo, Palermo, Italy Viale delle Scienze, Palermo
guido.ala@unipa.it

[2] Dipartimento di Ingegneria Chimica, Gestionale, Informatica e Meccanica
Università degli Studi di Palermo, Palermo, Italy Viale delle Scienze, Palermo
elisa.francomano@unipa.it

Abstract **─** In this paper a meshless approach on a high performance grid computing environment to run fast onerous electromagnetic numerical simulations, is presented. The grid computing and the message passing interface standard have been employed to improve the computational efficiency of the Smoothed Particle Electromagnetics meshless solver adopted. Applications involving an high number of particles can run on a grid computational environment simulating complex domains not accessible before and offer a promising approach for the coupling of particle models to continuous models. The used meshless solver is straightforward to program and fully parallelizable. The results of the parallel numerical scheme are reported and tested on a transverse electric propagation case study taken into account to assess the computational performance.

Index Terms **─** Electromagnetic Simulation, Grid Computing, Meshless method, Smoothed Particle Electromagnetics.

I. INTRODUCTION

In recent years the numerical treatment of partial differential equations with meshfree discretization has become a very active research area. Meshfree methods have undergone substantial development since the mid 1990s. The growing interest in these methods is due to the fact that they are very flexible numerical tools where node configurations have no fixed connectivity and have some advantageous features especially attractive when dealing with multiscale phenomena: a-priori knowledge about particular local behaviour of the solution can be introduced easily in the meshfree approximation space, and an enrichment of a coarse scale approximation with fine scale information is possible in a seamless way. Due to their independence of a mesh, meshfree methods can deal with diffuse in-homogeneity and complex geometry of the domain in a more easy way than standard discretization techniques [1-4]. For a large number of standard numerical methods that solve differential partial equations, the process needs the construction of a linear system and its numerical solution. This is true for finite element method (FEM), element free Galerkin (EFG) method and meshless local Petrov-Galerkin (MLPG) method, for instance. Different approaches are used in technical literature to parallelize numerical methods [5-6].

On the other hand, the approximation of the field variables in meshfree methods is usually based on processing information belonging to a local domain in the neighboring of the observation point, and the procedure has showed to be a simple way to speedup, so justifying the research for. The implementation of meshfree methods and their parallelization, requires special attention enabling to work with a wide range of complex and cumbersome applications. Smoothed Particle Hydrodynamic (SPH) was one of the first mesh-

Submitted On: Dec. 6, 2011
Accepted On: Mar. 4, 2012

1054-4887 © 2012 ACES

free methods to be proposed [7-15] and recently it has been reformulated to solve onerous time domain electromagnetic problems [16-17]. In time evolutionary simulations, the resulting meshless method, addressed as Smoothed Particles Electromagnetics (SPEM), computes the field variables by means of an integral formulation performed over a set of particles identified by a kernel function. The SPEM method, does not deal with a grid at all and the solution is computed directly for each field point using the neighboring information by avoiding the generation of a linear system. The spatial derivatives are computed by transferring the differentiation from the field variables into the kernel by employing two set of staggered particle distributions keeping information on magnetic and electric field components respectively. The method is fully parallelizable and characteristics of the collections of set and points, with implications for the performance of the algorithm, are considered and also exhibited through numerical examples. In SPEM the processing is totally independent on each field point at a given time step and, in this paper, it has been parallelized by using the Message Passing Interface (MPI) library in a grid environment. The resulting processing times are compared with the ones from sequential version. Moreover, the numerical solutions have been compared with the experimental results obtained in a sequential way obtaining a very satisfactory agreement, as confirmed by the performance analysis reported in the next of the paper. The paper is organized as follows. In section II the fundamentals of SPEM meshless solver are briefly summarized. In section III the features of the parallel approach are reported: the pre-processed computational step and the temporal step are addressed, respectively. Section IV validates the computational scheme by referring to a transverse electric (TE) simulation at different time steps.

II. THE MESHLESS SOLVER

SPH method is based on a set of points scattered in the domain involving a kernel function in order to discretize partial differential equations without any underlying mesh. In the absence of mesh, the spatial derivatives for each point of the domain have to be computed in order to proceed to the time integration. The spatial derivatives are determined into a finite domain surrounding each point of interest by means of a kernel function, and each of these points carry the discrete electric E and magnetic H field's quantities. The term kernel refers to a weighting function and defines how much each field variable contributes to the field variable at a point r.

By considering a given function $A(r)$ it is possible to convolute it by using its values and the chosen kernel function within a compact support D proportional to the so-called smoothing length, noted h, standing for the meshless equivalent of a space step used in classical mesh based methods:

$$< A(r) > = \int_D A(r')W(r - r', h)dr' . \qquad (1)$$

The convolution (1) is usually referred as *kernel approximation*. The kernel function has the following properties:

$$\int_D W(r - r', h)dr' = 1 , \qquad (2)$$

$$\underbrace{lim}_{h \to 0} \int_D W(r - r', h)dr' = \delta(r - r') . \qquad (3)$$

The kernel function depends on the distance. In this study, D is defined with a radius equal to $2h$ and the simulations have been performed by employing as kernel the standard cubic B-spline:

$$W(r - r', h) = \frac{\alpha}{h^d} \begin{cases} \frac{2}{3} - (\frac{\|r - r'\|}{h})^2 + \frac{1}{2}(\frac{\|r - r'\|}{h})^3, & 0 \le \frac{\|r - r'\|}{h} < 1 \\ \frac{1}{6}(2 - \frac{\|r - r'\|}{h})^3, & 1 \le \frac{\|r - r'\|}{h} < 2 \\ 0 & otherwise \end{cases} \qquad (4)$$

where d is the dimension of the problem domain and $\alpha = 1, \frac{15}{7\pi}, \frac{3}{2\pi}$ for $d=1,2,3$, respectively. In Fig. 1 the 2-d cubic B-spline is reported. One of the major advantages in using this kernel function is that it has compact support: particles interaction are zero at distances major than $2h$ (Fig. 2).

If $A(r')$ is known only at N discrete points $r_1, r_2, ..., r_N$ the equation (1) is discretized as follows:

$$A(r_i) = \sum_{j=1}^{N} W(r_i - r_j, h)A(r_j)dV_j . \qquad (5)$$

In a similar way, as an example, the gradient of any field function can be approximated by means of the following expression:

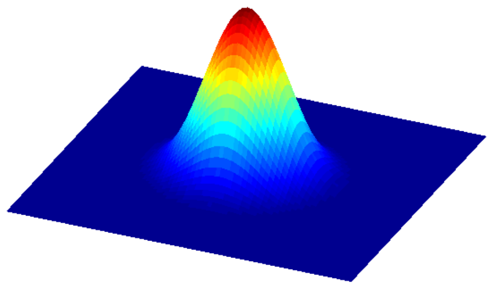

Fig. 1. 2-d cubic B-spline.

$$<\nabla_r A(r)>= \int_D \nabla_{r'} A(r') W(r-r',h)\, dr' \, , \qquad (6)$$

where $\nabla_{r'}$ indicates the derivative with respect to the primed coordinates and, in the discrete domain:

$$\nabla A(r_i) = \sum_{j=1}^{N} A(r_j) \nabla_i W(r_i - r_j, h)\, dV_j \qquad (7)$$

where ∇_i indicates the spatial derivative with respect to particle i's coordinates.

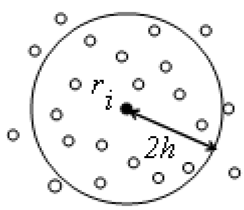

Fig. 2. Support domain of the kernel function.

Equation (7) is one of the main reason for which SPH method is so popular. It removes the need for a mesh to compute spatial derivatives. As well known, electromagnetic transients phenomena are described by Maxwell's curl equations in time domain, which in a non-dissipative medium can be written as follows:

$$\partial_t S \begin{pmatrix} E \\ H \end{pmatrix} = L \begin{pmatrix} E \\ H \end{pmatrix} \qquad (8)$$

where $S = \begin{pmatrix} \varepsilon & 0 \\ 0 & \mu \end{pmatrix}$, ε is the medium permittivity, μ the medium permeability and:

$$L = \begin{pmatrix} 0 & \nabla\times \\ \nabla\times & 0 \end{pmatrix} \qquad (9)$$

is the curl operator matrix. In contrast to general second-order problems (e.g., wave equations) where only one field, electric or magnetic, needs to be calculated, special arrangements of the particles need when the Maxwell's equations in first-order form are solved [18]. In the present paper, by following the FDTD method [19], in which the staggered Yee scheme yields second-order accuracy, two set of staggered particle distributions for E and H fields are considered. All fields components are stored in two set of nodes, E-particles and H-particles, respectively (Fig. 3) [16-17]. This position leads to two separate set of shape functions that approximate the E and H field component values, respectively (Fig. 4). The spatial derivatives of the electric field E are approximated by means of the derivatives of the kernel function centred in an E-particle and considering the H-particles as neighbouring, i.e. $\partial_q E \approx \partial_q W_E(r_i^E, r_j^H)$, $q = x,y,z$. In a similar way the spatial derivatives of the magnetic field H are approximated by means of the derivatives of the kernel function centred in an H-particle and by considering the E-particles as neighbouring, i.e. $\partial_q H \approx \partial_q W_H(r_i^H, r_j^E)$, $q = x,y,z$.

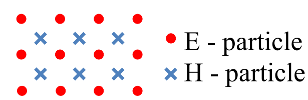

Fig. 3. E-particles and H-particles distribution.

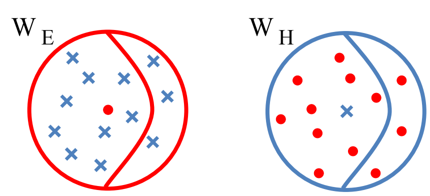

Fig. 4. Kernel functions with staggered E- and H-particles distribution.

In a transverse electric (TE) case with the E_z, H_x, H_y field components propagating in the x-y- directions, the problem is reduced to the following form:

$$\partial_t S \begin{pmatrix} E_z \\ H_x \\ H_y \end{pmatrix} = L^h \begin{pmatrix} E_z \\ H_x \\ H_y \end{pmatrix} \qquad (10)$$

E_z, H_x, H_y are vectors of length equal to the electric and magnetic field particles respectively. The matrix for TE waves contains the spatial derivatives in the x- and y-directions:

$$S = \begin{pmatrix} \varepsilon & 0 & 0 \\ 0 & \mu & 0 \\ 0 & 0 & \mu \end{pmatrix},$$

$$L^h = \begin{pmatrix} 0 & -\partial_y W_E & \partial_x W_E \\ -\partial_y W_H & 0 & 0 \\ \partial_x W_H & 0 & 0 \end{pmatrix} \tag{11}$$

In the matrix L^h, the spatial derivatives of the shape functions W_E and W_H in the x- and y-directions centred in the electric and magnetic field particles are employed, respectively:

$$\begin{aligned} \partial_q W_E &\equiv \partial_q W_E(r_i^E - r_j^H, h) \\ \partial_q W_H &= \partial_q W_H(r_i^H - r_j^E, h) \end{aligned} \qquad q=x,y \tag{12}$$

The temporal derivatives are discretized by a staggered march in time scheme and, by retaining the nomenclature of the previous section, the explicit time-domain update equations can be expressed as:

$$\begin{aligned} E^{(n+1/2)} &= E^{(n-1/2)} + \frac{\Delta t}{\varepsilon_0}\left[\partial_x W_E H_y^{(n)} - \partial_y W_E H_x^{(n)}\right] \\ H_x^{(n+1)} &= H_x^{(n)} - \frac{\Delta t}{\mu_0}\partial_y W_H E_z^{(n+1/2)} \\ H_y^{(n+1)} &= H_y^{(n)} + \frac{\Delta t}{\mu_0}\partial_x W_H E_z^{(n+1/2)} \end{aligned} \tag{13}$$

where the superscripts indicate the index of the time step, and the condition:

$$\Delta t \le min \frac{d_{min_i}}{c_0} \tag{14}$$

for the time stepping has been employed. This estimate is based on the distance to the closest neighbour of node and the speed of light c_0.

In order to simulate unbounded propagation, in SPEM the domain is truncated by introducing the well-known perfectly matched layer (PML) [20]. In this way, magnetic and electric field are progressively forced to zero within the external layer. As a consequence, the PML boundary conditions considerably reduce the numerical results corruption deriving from particles lacking outside the boundaries [8]. The particle belonging to PML are treated in the same way as for the particle in the interior domain.

III. THE PARALLEL APPROACH

In SPEM, the approximation process can be divided into two fundamentals steps. A pre-processing step for the selection of the neighbouring particles and the computation of the kernel derivatives, and a time dependent step for updating the electric and the magnetic field components values. In Fig. 4 a briefly description of the computation scheme is reported.

PRE-PROCESSING STEP
1. Computation of the distances 2. Computation of the electric field derivatives ∂W_E 3. Computation of the magnetic field derivatives ∂W_H
TEMPORAL STEP
4. Initial Condition 5. Temporal Loop 5.1 Updating of the electric field 5.2 Updating of the magnetic field

Fig. 4. Sketch of the computational process.

A. Pre-processing step

In order to avoid inefficient implementations, the particles must be carefully distributed in the problem domain. With the aim of generating a good load balancing and reducing the data transfer, the problem domain is broken up into strips among the processors. Each processor contains its own strip and it is in charge of calculating the interaction of each fixed particle with the neighboring ones. For the computation of the fields derivatives the interactions of each particle with its neighbors need, and it is performed out of the temporal step. A large part of the computational burden depends on the search procedure; it is therefore essential that efficient methods in a sequential way have been adopted for such a search. The determination of which particles are inside the interaction range, requires the computation of all pair-wise distances, whose computational time would be unpractical for large problems. This was a huge waste of CPU time since each particle gets non-zero values from only a small fraction of the total N particles. Simulations with a large number of particles are possible only if an efficient neighborhood search algorithm is employed. Working in a parallel way this bottle-neck is really reduced. Anyway, a framework of fixed cells is carried out to improve the neighboring search. For each particle, the interactions with its neighbours only within the kernel support of radius equal to *2h*, have to be computed.

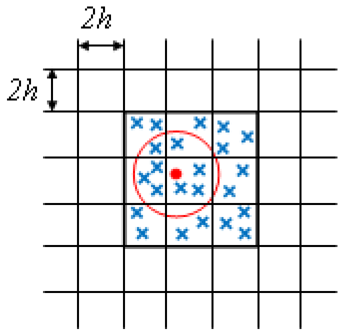

Fig. 5. Underlying grid.

Therefore firstly, a tessellation of the physical space through a cartesian grid composed of square cells with size equal to the kernel radius is carried out (Fig. 5). For a given particle a list of the particles contained in its cell, as well as in eight cells in 2-d around it have to be generated in order to find its neighbouring. Thus, only particles in the approximating area are tested, and any chance of missing an interaction is avoided. In the context of variable smoothing length, since the cell sizes may differ from the kernel radius, the number of cells to be explored is greater than nine. In this case the cell size is set as the lowest value of the smoothing length. It is important to address that the underlying grid is only used for the neighbouring search procedure.

In order to increase the speed up of the code a neighbour list for each particle is generated. A 2-d array X of cells is used to keep track of neighbours. Each cell in the grid contains two linked lists, one for the free particles in that cell and one for the boundary particles. Each cell in X was a square with side equal to *2h*, or two times the smoothing length. The reason the cells are *2h* in size is because the particles only interact up to distance minor than *2h* and thus only need to check the current cell and neighbouring cells to find all the possible particles that interact with the current ones.

B. Temporal step

In SPEM the processing is totally independent on each particle at a given time step, so the parallelization is done mainly based on particles distribution to processors. As reported in section II the algorithm uses a leap-frog integration time step: first the values must be predicted at a half step forward and then they are used to compute the changes in all variables due to interacting with neighbours.

Then all these information are used to compute the values at full time step ahead. After each time step, the buffer row is reloaded. These buffer rows include the particles that border but belonging to another processor. Only the fields computed on the particles lying on the boundaries, as shown in Fig. 6 in grey, have to be transferred to the adjacent processor. Each processor is interested in this data transfer. After the fields computation, all processors are synchronized in sending the updated fields. So working a good load balancing and a good data transfer is performed. In Fig. 7 the computational scheme at each time step t is reported by considering the P_N processors used in the computation. As reported in Fig. 7 each processor is computing the same operations: first of all the distances and the kernel derivatives are performed. The full line address the synchronization statements until all the processors end their work; at the end of the elaboration each processor produces the data regarding its region domain.

IV. VALIDATION RESULTS

In this section a *TE* case study has been addressed. A Gaussian pulse propagating in a 2-d domain of 6400 randomly placed particles is considered (Fig. 8). The source is placed in the domain in the central position and the wave propagation is to the boundaries of the domain. In Fig. 8 the simulations for computing the electric field E_z at different time steps are reported: the propagating wave crosses over the boundary and the propagation go over the space. As already underlined, in the simulation the PML [19] have been used by avoiding the wave reflections. In Table 1 the computational time for $N_P = 1$ and $N_P = 4$ processors has been reported. The code has been written by employing the MPI paradigm. For the sake of completeness, the obtained results have been compared with classic FDTD simulation. The obtained $\|\cdot\|_2$ relative error is equal to $5.61 \cdot 10^{-5}$, by using about 50 neighbors for a fixed particle [16].

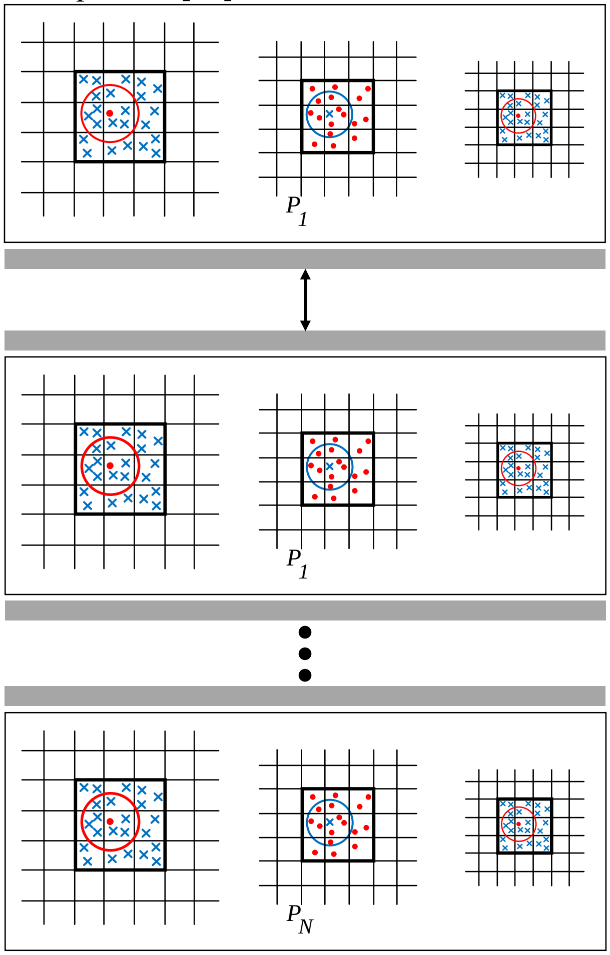

Fig. 6. Non-overlapping data regions.

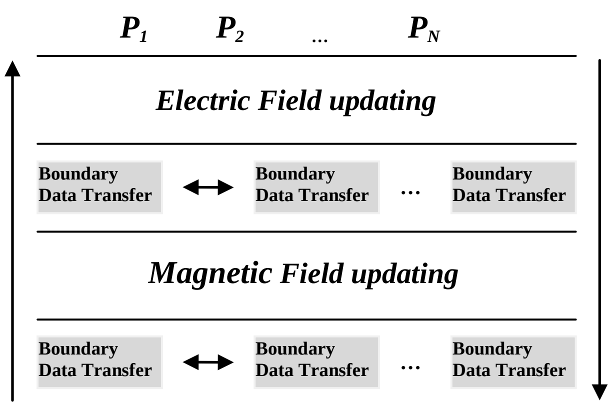

Fig. 7 . Computational scheme at each time step *t* .

The computing infrastructure is based on IBM Blade Centre H chassis each containing up to 14 IBM LS21 "blades" interconnected both with a double Gigabit Ethernet network, for normal communications with redundancy and load balancing, and a CISCO Topspin Infiniband-4X network, required to provide the Grid with high performance computing (HPC) functionalities.

Table 1: Elaboration Time [ms]

Computational stage	**N_P =1**	**N_P =4**
Pre-processing step	19217	4930
Temporal steps (*n*=4)	200	58
Total	19417	4988

The infrastructure is built with identical hardware and software at all sites. This choice was made on purpose to allow for the maximum interoperability and realizes a homogeneous environment which is a fundamental condition for an HPC Grid environment be able to run distributed parallel jobs of applications adopting the MPI paradigm. Each "blade" is equipped with 2 AMD Opteron 2218 rev. F dual-core processors with a clock rate of 2,6 GHz able to natively execute x86 32 and 64 bits binary code. Each processor has 2 GB of DDR2 RAM at 667 MHz (8 GB in total per "blade") and it is equipped with a direct communication channel to the other processor on the same motherboard. The memory controller is integrated on board. The storage infrastructure is based on IBM DS 4200 Storage Systems that provide high features of redundancy, management and reliability. In fact, a DS 4200 Storage System supports several types of RAID and has an intrinsic redundancy of all critical components (fan, power, controller, etc.) to assure maximum reliability. It allows expansions up to 56 TB each with SATA disks. Each Storage System is managed by two IBM x3655 servers that "export" the IBM GPFS parallel file system to all computing nodes. Overall, about 2000 CPU cores and more than 200 TB of disk storage space are currently available on the infrastructure. A reasonable time estimation [21] for the parallel implementation is:

$$T_p = T_s / N_P + O \qquad (15)$$

where T_s is the serial computational time, N_P is the number of processors and O is the overhead. The overhead O in the case of the proposed non-overlap paradigm is constant and is determined only by small data exchange between two adjacent processors P_i and P_{i+1}. Due to these considerations, by using the non-overlap data paradigm, a real speed-up close to the theoretical one and a highly scalable algorithm are obtained.

V. CONCLUSIONS

In this paper a parallel approach of the meshless solver SPEM to investigate transient electromagnetic propagation, is presented.

An insight is given into the relative computational burden, and some suggestions are provided on the computational and data structure of the neighborhood search by working with a GRID computational environment with HPC functionalities. Results are provided for a *TE* case study. The process involves local operators which use neighboring values to generate partial results; data strip partitioning with no data overlapping has shown to be suitable by working on distributed multiprocessor systems. Each data strip can be handled as a stand-alone problem and an exiguous amount of data transfer needs at each time step and a good task balancing is provided.

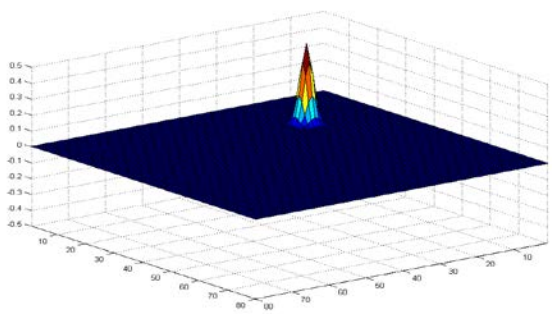

(a)

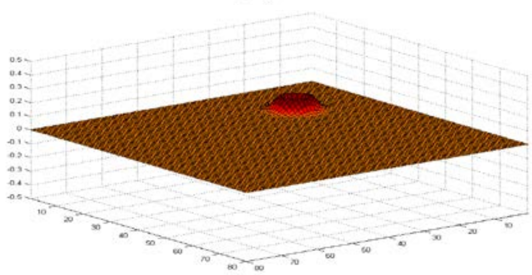

(b)

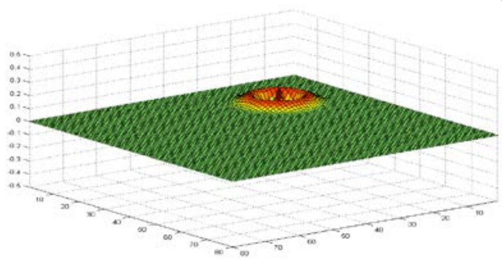

(c)

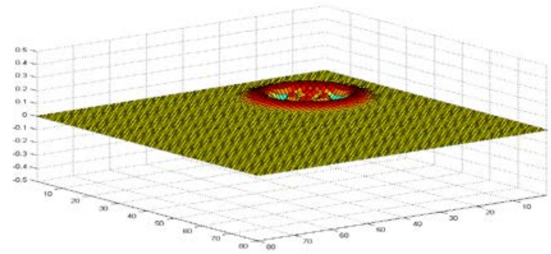

(d)

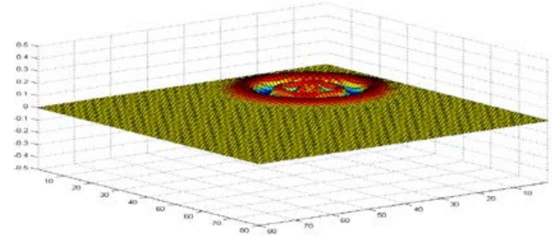

(e)

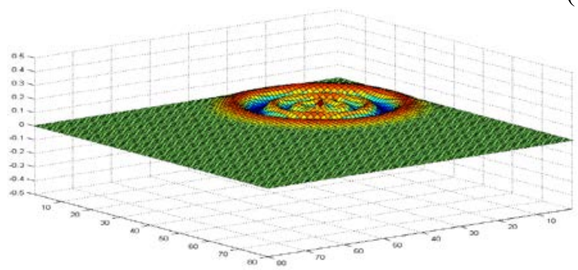

(f)

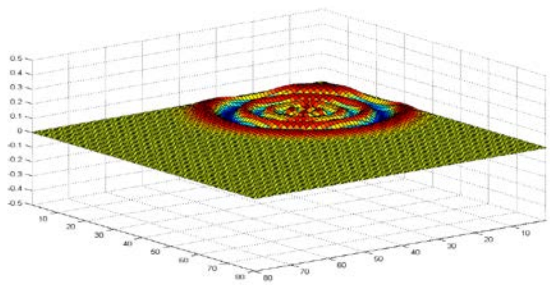

(g)

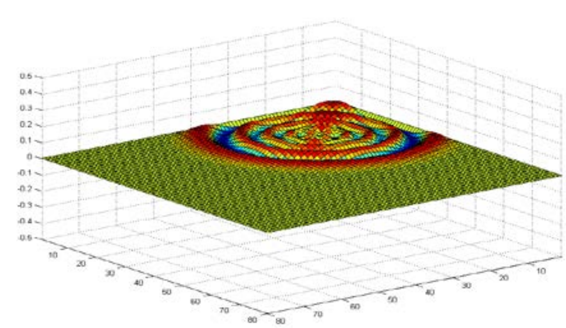

(h)

Fig. 8. Electric field E_z [V/m] propagation at different time steps, for the *TE* case study.

REFERENCES

[1] Y. Yu, Z. Chen, A 3-D Radial Point Interpolation Method for Meshless Time-Domain Modeling," *IEEE Transactions on Microwave Theory and Techniques,* vol. 57, no. 8, pp. 2015-2020, 2009.

[2] Y. Yu, Z. Chen, "Towards the development of an unconditionally stable time-domain meshless method," *IEEE Transactions on Microwave Theory and Techniques,* vol. 58, no. 3, pp. 578-586, 2010.
[3] X. Chen; Z. Chen; Y. Yu; D. Su, An Unconditionally Stable Radial Point Interpolation Meshless Method With Laguerre Polynomials," *IEEE Transactions on Microwave Theory and Techniques,* vol. 59, no. 10, pp. 3756-3763, 2011.
[4] Richard K. Gordon, W. Elliott Hutchcraft, "The Use of Multiquadric Radial Basis Functions in Open Region Problems," *Applied Computational Electromagnetics Society (ACES) Journal*, vol. 21, no. 2, pp. 127 – 134, July 2006.
[5] T. Iwashita, M. Shimasaki, J. Lu, "Parallel ICCG Solvers for a Finite-Element Eddy-Current Analysis on Heterogeneous Parallel Computation Environment," *Applied Computational Electromagnetics Society (ACES) Journal,* vol. 22, no. 2, pp. 195 – 200, July 2007.
[6] I. González, E. García, F. Saez de Adana, M. F. Cátedra, "MONURBS: A Parallelized Fast Multipole Multilevel Code Analyzing Complex Bodies Modeled by NURBS Surfaces," *Applied Computational Electromagnetics Society (ACES) Journal,* vol. 23, no. 2, pp. 134 – 142, June 2008.
[7] R. A. Gingold, J. J. Monaghan, "Smoothed Particle Hydrodynamics: Theory and Application to Non spherical Stars", *Mon. Not. Roy. Astron. Soc.*, vol.181, pp. 375-389, 1977.
[8] G. R. Liu, M. B. Liu, *Smoothed Particle Hydrodynamics - a Mesh-Free Particle Method*, World Scientic Publishing, Singapore, 2003.
[9] L. B. Lucy, "A numerical approach to the testing of fusion process", *The Astronomical Journal,* vol. 82, pp. 1013-1024, 1977.
[10] J. J. Monaghan, J. C. Lattanzio, "A refined particle method for astrophysical problems", *Astron.Astrophys,* vol. 149, pp.135–143, 1985.
[11] J. J. Monaghan, "An introduction to SPH", *Comput. Phys. Commun,* vol. 48, pp. 89-96, 1988.
[12] J. J. Monaghan, "Smoothed particle hydrodynamics", *Annu. Rev. Astron. Astrophys,* vol. 30, pp. 543–574, 1992.
[13] T. Belytschko, Y. Krongauz, D. Organ, M. Fleming, P. Krysl, "Meshless methods: an overview and recent developments", *Comput. Meth. Appl. Mech. Eng.,* vol. 139, pp. 3–47, 1996.
[14] G. R. Liu, *Mesh Free Methods—Moving beyond the Finite Element Method*, CRC Press, BocaRaton, 2003.
[15] P. Laguna, "Smoothed particle interpolation", *Astrophys. J.,* vol. 439 , pp. 814–821, 1995.
[16] G. Ala, E. Francomano, "An improved Smoothed Particle Electromagnetics method in 3D time domain simulations", *International Journal of Numerical Modelling: Electronic Networks, Devices and Fields,* DOI: 10.1002 /jnm.834, 2011.
[17] G. Ala, G. Di Blasi, E. Francomano, "A numerical meshless particle method in solving the magnetoencephalography forward problem", *International Journal of Numerical Modelling: Electronic Networks, Devices and Fields,* DOI: 10.1002 /jnm.1828, 2012.
[18] M. N. O. Sadiku, *Numerical Techniques in Electromagnetics,* CRC Press, Boca Raton, FL, 1992.
[19] D. M. Sullivan, *Electromagnetic Simulation Using the FDTD Method*, IEEE Press, New York, 2000.
[20] J. P. Berenger, "A Perfectly Matched Layer for the Absorption of Electromagnetic Waves", *Journal of Computational Physics,* vol. 114, pp. 185-200, 1994.
[21] D. P. Bertesekas, J. N. Tsitsiklis, *Parallel and Distributed Computation Numerical Methods,* Prentice Hall, 1989.

Dr. Prof. Guido Ala was born in 1964, he received the Laurea degree (Master degree) in Electrotechnical Engineering (cum laude and with honours) and the PhD degree in Electrotechnical Engineering (Electrical Sciences) from the University of Palermo, Italy, in 1989 and in 1994, respectively. After some industrial experiences he joined the Department of Electrical, Electronic and Telecommunication Engineering of the University of Palermo where he was appointed as an university researcher from 1996 to 2004. Since 2005 he is an associate professor at the same Department (now DIEETCAM). He teaches Fundamental of Circuit Theory, Principles of Electrical Engineering, Electromagnetic Compatibility, Electrical Engineering Numerical Modelling also for PhD students, and, from 2008 to 2011 he was the director of the master degree course in Electrical Engineering. His main research interests are in the fields of electromagnetic numerical methods, electromagnetic transient analysis, lightning, electromagnetic compatibility. He is also the tutor of students working with MIUR projects fellowships.

Dr. Prof. Elisa Francomano is an associate professor of Numerical Analysis, full time, from 2002 at the University of Palermo, Italy. She received the master degree in mathematics (cum laude) from the University of Palermo, in 1988. In 1989 she joined the Istituto di CAlcolo e Reti ad alte prestazioni (ICAR-National Research Council) on a fellowship, working on numerical methods and parallel computing. From 1992 to 2002, she was Senior University Researcher. Since 1989 she has been in the activities of Numerical Analysis group of the University of Palermo and she has given lectures in many courses for students in engineering, in chemistry, in mathematics and in statistics. She thought Numerical Analysis, Fundamentals of Computer Science, Parallel Algorithms, for PhD students too. She is a tutor for students working with MIUR and National Research Council projects fellowships and is in charge of national and international scientific projects. Since 2005 to 2010 she was vice-director of the Centro Interdipartimentale di Tecnologie della Conoscenza (CITC) of the University of Palermo, Italy. Her main research interests are in the fields of computational science, with major applications in electromagnetic transient analysis and in computer vision dealing with numerical linear algebra, integral and partial and differential equations, approximation theory, high-performance scientific computing.

Transient Analysis of Thin-Wire Antennas over Debye Media

Mario F. Pantoja [1], Amelia R. Bretones [1], Salvador G. García [1], X. Lucas Travassos [2], and Rafael G. Martín [1]

[1] Departamento de Electromagnetismo
Universidad de Granada, Granada, 18071, Spain
mario@ugr.es, arubio@ugr.es, salva@ugr.es, rgomez@ugr.es

[2] Department of Electrical and Computer Engineering
SENAI CIMATEC - Integrated Center of Manufacturing and Technology, Bahia, 41650-010, Brazil
travassos.senai@gmail.com

Abstract **─** This paper presents a numerical procedure to calculate the time-domain response of thin-wire antennas over Debye media. The method is based in an expansion of the electric-field integral-equation in the time-domain (EFIE-TD), which accounts for the Debye media by using a reflection-coefficient approach. Resulting extended integral equation is subsequently solved by the method of moments. Numerical examples including Debye soils show not only the accuracy of the method but also a higher computational efficiency in comparison with other hybrid numerical techniques.

Index Terms **─** Reflection coefficient approximation, time-domain integral equation, thin-wire antennas.

I. INTRODUCTION

Early formulated in the eighties [1], time-domain integral equations provide an accurate and computationally efficient solution of Maxwell's equations. Their main drawback is a lack of versatility, because in most practical cases is not possible to infer valid integral-equations for complex media, which limits their role as part of the electromagnetic numerical solvers. However, in those feasible cases, the abovementioned superior computational performance compared with differential formulations [2] makes them an interesting line of research. This paper is focused in the extension of the EFIE-TD to account for the presence of a half-space Debye media. This a problem of interest in different practical cases in which Debye-dispersive materials appear ─e.g., wet soils at ground-penetrating radar (GPR) [3] or ceramic materials for nondestructive evaluation purposes [4].

There are different approaches to account for half-space dispersive media applying both differential and integral equations. Regarding integral equations, good results have been reported by using procedures based in exact Green function's for the considered media [5], or methods which derive surface equivalent currents in the boundary of the half-space [6]. Both choices share the advantage of providing accurate solutions for antennas placed near above the dispersive media, but also pay a high price in terms of computational cost in comparison to their non-dispersive counterpart. However, most practical cases include antennas placed above the Debye media at a height enough to apply the reflection coefficient approach [7, 8], leading thus to alternative integral equations which lead to computationally efficient codes [9]. A key point to implement this reflection-coefficient (RC) method is the availability of analytical equations for the reflection coefficients in the time domain. Recently, several papers [10, 11] have presented these coefficients for Debye media both in TE and TM formulations, enabling so the application of the RC approach to model thin-wire antennas in front of Debye media. At this point, it can be pointed out that the problem of thin-wires antennas in front of complex media has

Submitted On: Sept. 23, 2011
Accepted On: Jan. 26, 2012

been also addressed by applying the FDTD method. For instance, a ground penetrating radar antenna was modeled using a hybrid FDTD-MoM technique in [12], and examples including thin-wire subcell model based on modified telegrapher`s equations were firstly presented in [13] and later applied for the analysis of thin wire antennas in a loaded cavity in [14].

This paper is structured as follows. Taking as starting point the EFIE-TD for non-dispersive case, Section II presents the proposed numerical integral-equation procedure to account for the half-space Debye media, including both a brief formulation of the reflection coefficients in the time domain and numerical expressions to solve the integral equation by the method-of-moments. Section III proceeds to validate the code, and also presents some additional results including water soil for test purposes.

II. EFIE-TD FOR THIN WIRES ABOVE DEBYE MEDIA

Thin-wire structures are those whose radius a is negligible compared with its length, and thus two-dimensional surface currents $\vec{J}_S\left(\vec{r}\,',t'\right)$ can be approximated as one-dimensional total currents $\vec{I}\left(\vec{r}\,',t'\right)=2\pi a\vec{J}_S\left(\vec{r}\,',t'\right)$, placed at the center of the thin-wire structure and flowing along its axis. PEC thin-wire antennas, widely employed in practice because of its portability, are a class of antennas which performance is very well-known [15], and constitutes a good choice for testing the accuracy and computational performance of numerical algorithms solving EFIE. When located inside a dielectric space with permittivity ε and velocity of propagation v, EFIE-TD for PEC thin-wires is:

$$\begin{aligned}\left(\vec{E}^i(\vec{r},t)\right)_{\tan} &= \left(\frac{1}{4\pi\varepsilon}\int_C \frac{1}{v^2R}\frac{\partial}{\partial t}\vec{I}(\vec{r}\,',t')ds'\right)_{\tan} \\ &+\left(\frac{1}{4\pi\varepsilon}\int_C \frac{\vec{R}}{R^3}\left(\int_0^{t'}\frac{\partial}{\partial r'}I(\vec{r}\,',\tau)d\tau\right)ds'\right)_{\tan} \\ &+\left(\frac{1}{4\pi\varepsilon}\int_C \frac{\vec{R}}{vR^2}\frac{\partial}{\partial r'}I(\vec{r}\,',t')ds'\right)_{\tan}\end{aligned} \quad (1)$$

where $\vec{r}$, $\vec{r}\,'$ and $\vec{R}$ accounts for field, source and distance vectors, respectively, and $t'=t-R/v$ is the retarded time which assures the causality of the system. C corresponds to the contour following the axis of the wire, where s' and s note the positions located in the axis and on the surface of the wire, respectively. Making use of $\hat{s}$ as the tangential unit vector on the surface of the wire, equation (1) can be expressed as:

$$\begin{aligned}\hat{s}\cdot\vec{E}^i(\vec{r},t) &= \frac{1}{4\pi\varepsilon}\int_C \frac{\hat{s}}{v^2R}\cdot\frac{\partial}{\partial t}\vec{I}(\vec{r}\,',t')ds' \\ &+\frac{1}{4\pi\varepsilon}\int_C \frac{\hat{s}\cdot\vec{R}}{R^3}\left(\int_0^{t'}\frac{\partial}{\partial r'}I(\vec{r}\,',\tau)d\tau\right)ds' \\ &+\frac{1}{4\pi\varepsilon}\int_C \frac{\hat{s}\cdot\vec{R}}{vR^2}\frac{\partial}{\partial r'}I(\vec{r}\,',t')ds'\end{aligned} \quad . (2)$$

If a ground plane is present, equation (2) is no longer valid [16, 17], because contributions from the reflected electromagnetic field in the surface are not considered. RC approximation [7] holds that total electric field in any point on the dielectric media surrounding the antenna can be expressed as a sum of a direct wave, corresponding to the scattered field in the dielectric $\vec{E}^d\left(\vec{r},t\right)$, and a reflected wave, calculated as the convolution of the time domain reflection coefficient $\Gamma^D\left(t\right)$ of the dielectric-Debye interface and the electric field coming from an image source Ψ located into the Debye media $\vec{E}^r\left(\vec{r},t\right)$:

$$\hat{s}\cdot\vec{E}^i(\vec{r},t)=\hat{s}\cdot\left(\vec{E}^d(\vec{r},t)+\Gamma^D(t)*\vec{E}^r(\vec{r},t)\right), \quad (3)$$

where

$$\begin{aligned}\vec{E}^d(\vec{r},t) &= \frac{1}{4\pi\varepsilon}\int_C \frac{1}{v^2R}\frac{\partial}{\partial t}\vec{I}(\vec{r}\,',t')ds' \\ &+\frac{1}{4\pi\varepsilon}\int_C \frac{\vec{R}}{R^3}\left(\int_0^{t'}\frac{\partial}{\partial r'}I(\vec{r}\,',\tau)d\tau\right)ds' \\ &+\frac{1}{4\pi\varepsilon}\int_C \frac{\vec{R}}{vR^2}\frac{\partial}{\partial r'}I(\vec{r}\,',t')ds'\end{aligned} \quad , (4)$$

and

$$\begin{aligned}\vec{E}^r(\vec{r},t) &= \frac{1}{4\pi\varepsilon}\int_{C_\psi} \frac{1}{v^2R}\frac{\partial}{\partial t}\vec{I}(\vec{r}\,',t')ds' \\ &+\frac{1}{4\pi\varepsilon}\int_{C_\psi} \frac{\vec{R}}{R^3}\left(\int_0^{t'}\frac{\partial}{\partial r'}I(\vec{r}\,',\tau)d\tau\right)ds' \\ &+\frac{1}{4\pi\varepsilon}\int_{C_\psi} \frac{\vec{R}}{vR^2}\frac{\partial}{\partial r'}I(\vec{r}\,',t')ds'\end{aligned} \quad , (5)$$

where contour image wires C_Ψ are located at positions according to classical image theory, involving only straightforward geometrical equations. Thus, the Debye half-space is removed of the original problem and it is substituted by an equivalent problem placed at free-space where equations based on Green's functions remain valid. It is important to remark that equation (3) is only applicable in those cases where the antenna is in the vicinity of the ground at heights h accomplishing [8]:

$$h > \frac{0.25\lambda}{\varepsilon_r\sqrt{1+\frac{\sigma}{j\omega\varepsilon_r\varepsilon_0}}} \quad . (6)$$

Analytical equations of $\Gamma^D(t)$ are available [10], expressed in terms on the polarization of the plane-wave incident to the ground plane. Naming $\hat{n}$ as the unit vector normal to the ground plane in the point of incidence, and $\Gamma^D_{TM}(t)$ and $\Gamma^D_{TE}(t)$ as the time-domain RC in the case of vertically and horizontally polarized waves, respectively, equation (5) can be decomposed as [18]:

$$\begin{aligned}&\hat{s}\cdot\vec{E}^i(\vec{r},t)=\hat{s}\cdot\vec{E}^d(\vec{r},t)+\hat{s}\cdot\left\{\Gamma^D_{TE}(t)*\left(\vec{E}^r(\vec{r},t)\cdot\hat{n}\right)\hat{n}\right\}\\&+\hat{s}\cdot\left\{\Gamma^D_{TM}(t)*\left[\vec{E}^r(\vec{r},t)-\left(\vec{E}^r(\vec{r},t)\cdot\hat{n}\right)\hat{n}\right]\right\}=\\&\hat{s}\cdot\vec{E}^d(\vec{r},t)+\hat{s}\cdot\left\{\Gamma^D_{TM}(t)*\vec{E}^r(\vec{r},t)\right\}\\&+\hat{s}\cdot\left\{\left[\Gamma^D_{TE}(t)-\Gamma^D_{TM}(t)\right]*\left(\vec{E}^r(\vec{r},t)\cdot\hat{n}\right)\hat{n}\right\}\end{aligned}, \quad (7)$$

which is, by substituting of equations (4) and (5), the thin-wires EFIE-TD for half-space Debye media.

A. TD-RC for half-space Debye media

The TD-RC for the incidence of electromagnetic plane-waves onto an interface separating dielectric and Debye media has been presented in [10], and further computationally improved by [11, 19]. In this work, the formulation achieved by applying directly an inverse Laplace transform to the Fresnel RCs is applied, because 1) do not require of additional parameters related to series representing the analytical equations, and 2) the effect of the savings in the computational burden in a method-of-moments (MoM) code for solving equation (7) is limited. Naming τ, ε_s, and ε_∞, the relaxation time, static and infinite permittivity, respectively, of the Debye media, and θ the angle of incidence, the TD-RC for TE polarized waves is:

$$\begin{aligned}\Gamma^D_{TE}(t)&=\frac{1-K_{TE}}{1+K_{TE}}\delta(t)+F_{TE}s_Bg_1(t)u(t)\\&-F_{TE}2s_B{}^2\frac{K_{TE}}{1-K_{TE}{}^2}\left[e^{-s_At}u(t)*g_2(t)u(t)\right]\end{aligned}, \quad (8)$$

where:

$$K_{TE}=\frac{\sqrt{\varepsilon_\infty-\sin^2\theta}}{\cos\theta}, \quad (9)$$

$$F_{TE}=\frac{2K_{TE}}{\left(1+K_{TE}\right)\left(1-K_{TE}{}^2\right)}, \quad (10)$$

$$s_A=\frac{1}{\tau}\frac{\varepsilon_s-1}{\varepsilon_\infty-1}, \quad (11)$$

$$s_B=\frac{1}{2\tau}\frac{\varepsilon_s-\varepsilon_\infty}{\varepsilon_\infty-\sin^2\theta}, \quad (12)$$

and:

$$g_1(t)=e^{-\frac{t}{\tau}}\left[\left(K_{TE}-1\right)\overline{I}_0\left(s_Bt\right)-\left(K_{TE}+1\right)\overline{I}_1\left(s_Bt\right)\right], \quad (13)$$

$$g_2(t)=e^{-\frac{t}{\tau}}\left[\left(K_{TE}-1\right)\overline{I}_0\left(s_Bt\right)+\left(K_{TE}+1\right)\overline{I}_1\left(s_Bt\right)\right], \quad (14)$$

with $\overline{I}_n(x)$ corresponding to the exponentially modified Bessel function of the first kind and order n, and $u(x)$ to the unit step function.

Additionally, TD-RC for TM polarized waves can be written as:

$$\begin{aligned}\Gamma^D_{TM}(t)&=\frac{1-K_{TM}}{1+K_{TM}}\delta(t)+F_{TM}K_{TM}\left[f_2(t)-f_1(t)\right]u(t)\\&-F_{TM}\left(1+K_{TM}\right)s_B\left[g_3(t)u(t)+f_1(t)u(t)*g_3(t)u(t)\right]\end{aligned}, \quad (15)$$

where:

$$K_{TM}=\frac{\varepsilon_\infty\cos\theta}{\sqrt{\varepsilon_\infty-\sin^2\theta}}, \quad (16)$$

$$F_{TM}=\frac{2K_{TM}}{\left(1+K_{TM}\right)\left(1-K_{TM}{}^2\right)}, \quad (17)$$

$$Q=\frac{\varepsilon_\infty-2\sin^2\theta}{\varepsilon_\infty}, \quad (18)$$

and:

$$f_1(t)=\left[A_1e^{-s_Et}+B_1e^{-s_Ft}\right], \quad (19)$$

$$f_2(t)=\left[A_2e^{-s_Et}+B_2e^{-s_Ft}\right], \quad (20)$$

$$g_3(t) = e^{-\frac{t}{\tau}}\left[Q\bar{I}_0\left(s_B t\right) + \bar{I}_1\left(s_B t\right)\right] \quad , (21)$$

where (s_E, s_F) are the negative roots of the second-order polynomial *P(s)*:

$$P(s) = s^2 + s\left(\frac{s_0 + s_1 - 2s_2K_{TM}^2}{1-K_{TM}^2}\right) + \left(\frac{s_0 s_1 - 2{s_2}^2 K_{TM}^2}{1-K_{TM}^2}\right), \quad (22)$$

and additional constants included in equations (19), (20), and (22) are:

$$s_0 = 1/\tau \quad , (23)$$

$$s_1 = \frac{1}{\tau}\frac{\varepsilon_s - \sin^2\theta}{\varepsilon_\infty - \sin^2\theta} \quad , (24)$$

$$s_2 = \frac{1}{\tau}\frac{\varepsilon_s}{\varepsilon_\infty} \quad , (25)$$

and:

$$A_1 = \frac{\left(s_0 - s_E\right)\left(s_1 - s_E\right)}{\left(s_F - s_E\right)} \quad , (26)$$

$$B_1 = -\frac{\left(s_0 - s_F\right)\left(s_1 - s_F\right)}{\left(s_F - s_E\right)} \quad , (27)$$

$$A_2 = \frac{\left(s_2 - s_E\right)\left(s_2 - s_E\right)}{\left(s_F - s_E\right)} \quad , (28)$$

$$B_2 = -\frac{\left(s_2 - s_F\right)\left(s_2 - s_F\right)}{\left(s_F - s_E\right)} \quad . (29)$$

B. MoM for thin-wires EFIE-TD including half-space Debye media

The computational implementation of equation (7) can be made through the MoM [20]. In this work, unknown currents $I\left(s',t'\right)$ of equations (4) and (5) are expanded using lagrangian sub-sectional basis functions [21], defined in N_S spatial and N_T temporal segments along a rectilinear uniform segmentation of the contour of the thin-wires. Weight functions applied are point-matching delta functions $\delta\left(\vec{r} - \vec{r}_u\right)$ and $\delta\left(t - t_v\right)$ chosen, respectively, along a set of N_S points $\vec{r}_u$ located the surface of the wire, and a discrete set of time N_T instants t_v.

Therefore, it can be named Δ_i as the size of thee *i-th* segment of the wire, Δ_t as the duration of the time intervals in the marching-on-time procedure, $s_i'' = s' - s_i$ as the distance of a position s' located at any *i-th* segment of the wire from its center s_i, and $t_j'' = t' - t_j$ as the time distance referred to a chosen *j-th* time t_j. Using this notation and the point-matching functions, a discrete form of equation (7) arises:

$$\hat{s}_u \cdot \vec{E}^i(\vec{r}_u,t_v) = \hat{s}_u \cdot \vec{E}^d(\vec{r}_u,t_v) + \hat{s}_u \cdot \left\{\Gamma_{TM}^D(t_v) * \vec{E}^r(\vec{r}_u,t_v)\right\} + \hat{s}_u \cdot \left\{\left[\Gamma_{TE}^D(t_v) - \Gamma_{TM}^D(t_v)\right] * \left(\vec{E}^r(\vec{r}_u,t_v)\cdot\hat{n}\right)\hat{n}\right\}, \quad (30)$$

in which the direct and reflect waves are given by:

$$\vec{E}^d(\vec{r}_u,t_v) = \frac{1}{4\pi\varepsilon}\sum_{i=1}^{N_S}\int_{\Delta_i}\frac{\hat{s}_i}{v^2R_{iu}}\frac{\partial I_{ij}(s_i'',t_j'')}{\partial t_j''}ds_i'' + \frac{1}{4\pi\varepsilon}\sum_{i=1}^{N_S}\int_{\Delta_i}\frac{\vec{R}_{iu}}{R_{iu}^3}\left(\int_0^{t_j''}\frac{\partial I_{ij}(s_i'',\tau)}{\partial s_i''}d\tau\right)ds_i'' + \frac{1}{4\pi\varepsilon}\sum_{i=1}^{N_S}\int_{\Delta_i}\frac{\vec{R}_{iu}}{vR_{iu}^2}\frac{\partial I_{ij}(s_i'',t_j'')}{\partial s_i''}ds_i'', \quad (31)$$

and

$$\vec{E}^r(\vec{r}_u,t_v) = \frac{1}{4\pi\varepsilon}\sum_{i=1}^{N_S}\int_{\Delta_{\psi,i}}\frac{\hat{s}_i}{v^2R_{iu}}\frac{\partial I_{ij}(s_i'',t_j'')}{\partial t_j''}ds_i'' + \frac{1}{4\pi\varepsilon}\sum_{i=1}^{N_S}\int_{\Delta_{\psi,i}}\frac{\vec{R}_{iu}}{R_{iu}^3}\left(\int_0^{t_j''}\frac{\partial I_{ij}(s_i'',\tau)}{\partial s_i''}d\tau\right)ds_i'' + \frac{1}{4\pi\varepsilon}\sum_{i=1}^{N_S}\int_{\Delta_{\psi,i}}\frac{\vec{R}_{iu}}{vR_{iu}^2}\frac{\partial I_{ij}(s_i'',t_j'')}{\partial s_i''}ds_i'', \quad (32)$$

where $\hat{s}_u$ and $\hat{s}_i$ stand for the tangential vectors, respectively, to the contour of the wire at the field point $\vec{r}_u$ and to the axis of the wire at the source point $\vec{r}_i$. $\vec{R}_{iu}$ corresponds to the vector between source and field points, and accomplishes the relation $\vec{R}_{iu} = \vec{r}_u - \vec{r}_i - s_i''\hat{s}_i$.

In order to keep an affordable computational burden in the solution of equation (30) it is required to pay a special attention to the terms involving the convolution operation. As it is shown in [10, 11], and similarly to the transient response from lossy grounds [22], the TD-RC from a Debye soil shows a highly decreasing form for realistic soils (see Figure 1 where TD-RC of typical ground and water half-space, chosen as examples of very different Debye media, are depicted). Based in this property, it can be established a useful approximation which allows to neglect late-time responses of the TD-RC and, thus, undesirable long computational times for convolutions. This approximation consists in a temporal truncation of the TE and TM TD-RCs to $0<t<t_{max}$, where t_{max} correspond to that time where $\Delta t\cdot\Gamma^{D}_{\{TE,TM\}}\left(t_{\max}\right) < 0.1\cdot\Gamma^{D}_{\{TE,TM\}}\left(0\right)$ with Δt corresponding to the time interval of analysis. In practice, no significant loss of accuracy is made by applying this condition, because in those cases where the rate of decrease in the TD RC response is lower, the impulsive part of equations (8) or (15) outweighs their non-impulsive counterpart. For those Debye media where the non-impulsive part predominates, its decreasing rate is high enough to only consider a limited set of terms of the time response. It worth to remark that the former approximation is compromised for high angles of incidence, which should be considered for thin-wire antennas very near to the interface. However, this fact does not imply a restriction in practice, because the accuracy of the RC approach is only guaranteed for heights of the thin-wires high enough above the ground [8].

III. RESULTS

A. Validation of the code

Numerical results for the validation of the code have been achieved by simulating the scenario shown at Figure 2. A separate validation of TE and TM cases can be performed by considering only one wire above ground ─where only TM TD-RCs plays a role in the simulation, and two wires ─where both TM and TE are placed under consideration. Figure 2 also shows the image thin-wires below ground, which correspond to the term of contour C_Ψ in equation (32).

Therefore, a typical slightly wet Debye soil with parameters ε_s=2.5220, ε_∞=2.4725, and τ=21.5·10^{-12} s [23] is chosen for the validation. First example under consideration validates the code for TM-incidence by considering a thin-wire antenna of total length of 1 m and a diameter of 5 mm placed at a height of 0.25 m above the soil. The antenna is fed at its central point by a normalized derivative gaussian pulse in the form:

$$v(t) = e^{0.5} g\sqrt{2}(t-t_{\max})e^{-g^2(t-t_{\max})^2}, \qquad (33)$$

with parameters g=1.5·10^9 s^{-1} and t_{max}=4/g. Figure 3 shows the current at the feed point, in comparison to a full-wave simulation coming from a FDTD code including thin-wire approach [24]. Accuracy of the results is in the range of previously reported differences between TDIE and FDTD methods [25, 26]. A minor time delay is appreciated by comparing the calculated waveforms of MoM-TD RC and FDTD. Reasons for this delay are associated to the longer wavelengths of the feeding pulse, which does not accomplish the required height to wavelength ratio corresponding to equation (6).

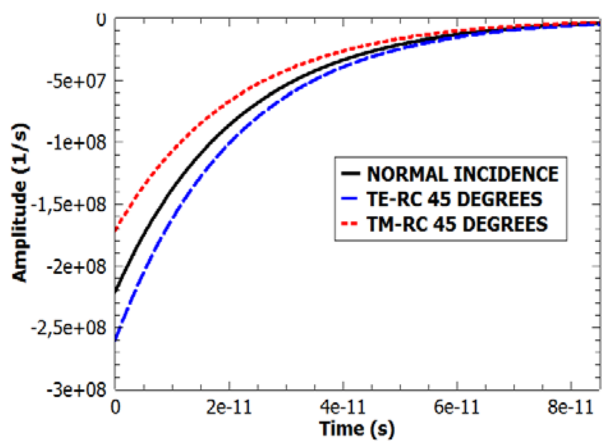

(a)

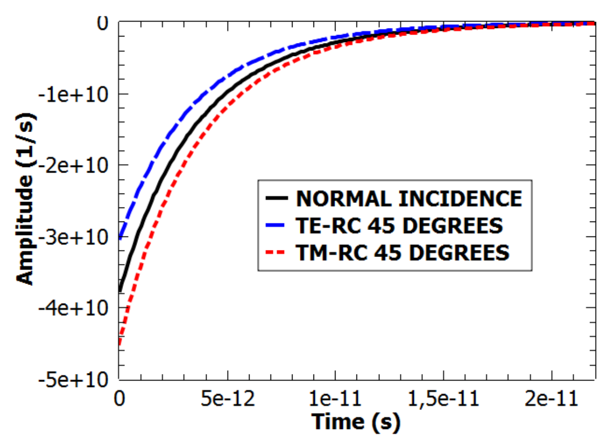

(b)

Fig. 1. TD-RC at different angles of incidence for a free space-Debye interface with parameters corresponding to (a) typical soil and (b) water.

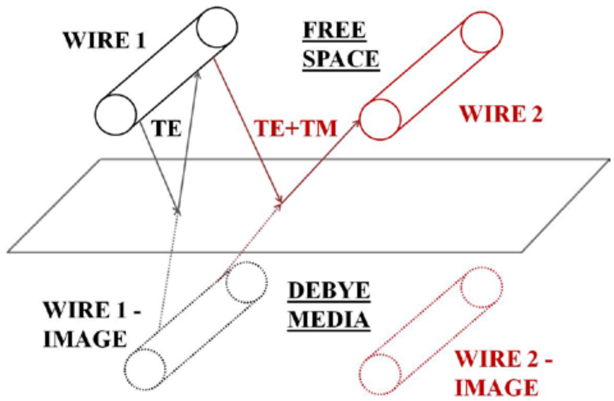

Fig. 2. Simulated scenario of horizontal thin-wires in a free space-Debye media. The results section shows different examples by considering only one thin-wire (black) as transmitter and a second thin-wire (red) as receiver.

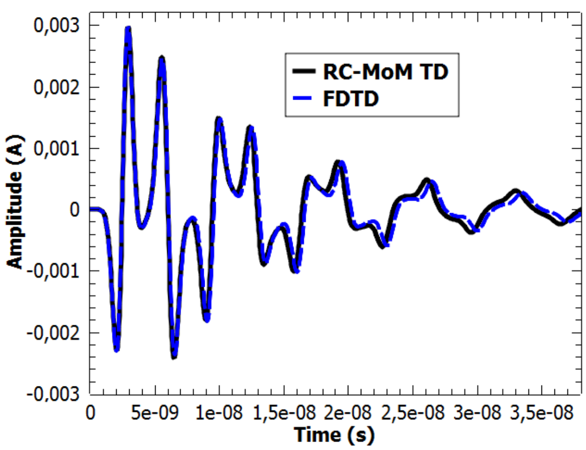

Fig. 3. Current at the center of a single horizontal thin-wire antenna above ground.

Figure 4 depicts the results of the validation for the two horizontal thin-wires case, in a configuration resembling the bistatic mode of a GPR equipment. Thus, a thin-wire acts as transmitting antenna, and it is fed as its center with a pulse of waveform following equation (33), while the other thin-wire is the receiving antenna in which measurements of the incoming electric field are made through the current at its center. Parameters of the feeding pulse are $g=1.5\cdot10^{9}$ s^{-1} and $t_{max}=4/g$, and thin-wires are located at a horizontal distance of 0.25 m, and both placed 0.25 m above ground. The conclusions regarding the accuracy of the method are similar to those mentioned for the single thin-wire case.

B. Thin-wire antennas over Debye soils

Numerical methods have been developed for the simulation of GPR scenarios [12, 27, 28]. Performance of GPR antennas, e. g. mismatch of input impedance, above a Debye soil can be degraded as a consequence of the coupling effect of the reflecting wave produced by the ground. Controlling this effect is important in GPR applications, because mismatches can result in dispersive waveforms non-related to the presence the objects, and thus can lead to false positives in the detections. As an example of the usefulness of the proposed algorithm, a monostatic GPR equipment has been modelled by placing a single horizontal thin-wire in front of both slightly wet soil of Section 3A, as well as in front of a water soil (which has been chosen as an extreme case of fully-saturated water soil). Debye parameters of water-soil $\varepsilon_s=81.83$, $\varepsilon_\infty=23.46$, and $\tau=9.41\cdot10^{-12}$ s [23], and feeding pulse and geometrical parameters are identical to the single-wire case of Figure 3.

Time-domain currents at the center of the antenna for these soils are shown at Figure 5. The case of a thin-wire embedded in free space is also plot as reference signal. It can be appreciated the strong effect of the water soil in the reflected pulse, which can mask reflected signals produced by buried objects, and thus disable the effectiveness of the equipment.

Figure 6a and 6b show another effect which should be considered at the design stage of the antennas. When placed in front of Debye media, input impedance of the antenna can change abruptly, leading to undesirable mismatches which could affect to the life cycle of the equipment. For example, first resonances of the dipoles depicted in Figure 6 are placed at 143 MHz, 142 MHz, and 139 MHz for free space, wet soil, and water media, respectively. So, a minor frequency shift is produced by the presence of the Debye media. However, the real part of the input impedance at the first resonance is 70 Ω, 60 Ω, and 17 Ω for free space, wet soil, and water, respectively. Potential damages could happen in front of water soils with such mismatches at the input impedance.

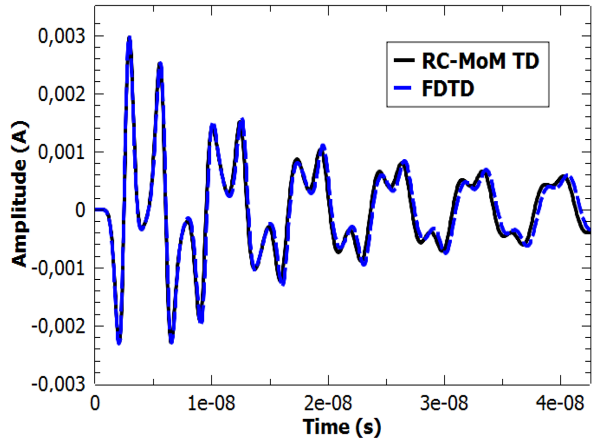

(a)

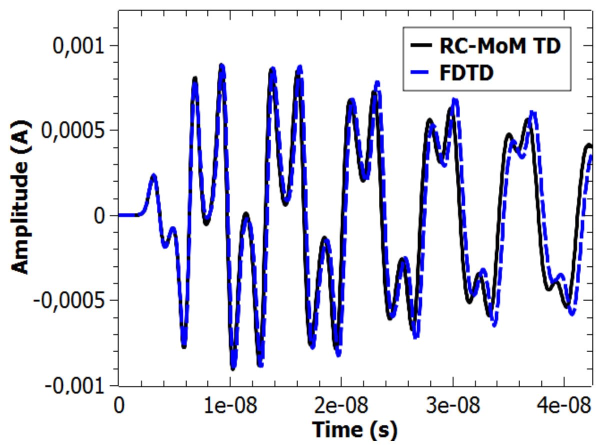

(b)

Fig. 4. Current at the center of the (a) transmitting and (b) receiving antenna for the case of two horizontal thin-wires above ground.

A final aspect to be considered is the reduction of the computational time achieved by using the proposed algorithm. Compared to finite difference schemes, it is roughly 400 times for the slightly wet soils and near to 800 for the water soil. It is very interesting to remark that the presence of the water half-space also increase the computational time for the RC-TDIE approach, because the shorter RC waveforms of the water soil (see Figure 1) require for a decrease of the time interval in order to provide an adequate sampling of the RC. For this reason, and following numerical guidelines of [1] according to the spectra of the feeding pulse, 101 spatial segments have been used to model any of the thin-wires in the case of free-space and slightly wet soils, leading to a time interval of 33.02 picoseconds, while a total of 202 segments are needed for the case of the water soils. Spite this fact, a finer spatial discretization is also necessary in FDTD for the water half-space and thus even higher computational savings in time are achieved by the RC-TDIE algorithm.

VI. CONCLUSION

This paper has presented a numerical method based on a hybrid RC-TDIE approach for the simulation of thin-wire antennas placed over Debye soils. Numerical results have shown the accuracy of the method as well as a low-cost computational performance compared to full-wave procedures. Examples have also shown the utility of the numerical simulations for the design of thin-wire antennas for GPR applications.

ACKNOWLEDGMENT

The authors would like to thank the Spanish Ministry of Education and Brazilian CAPES for their support of this work, through project PR2009-0067. The authors would also like to acknowledge partial support by the EU FP7/2007-2013, under GA 205294 (HIRF SE project), from the Spanish National Projects TEC2007-66698-C04-02, CSD200800068, DEX-5300002008105, and from the Junta de Andalucia Project TIC1541. This work was also supported by the Brazilian agencies CNPq and FAPEMIG.

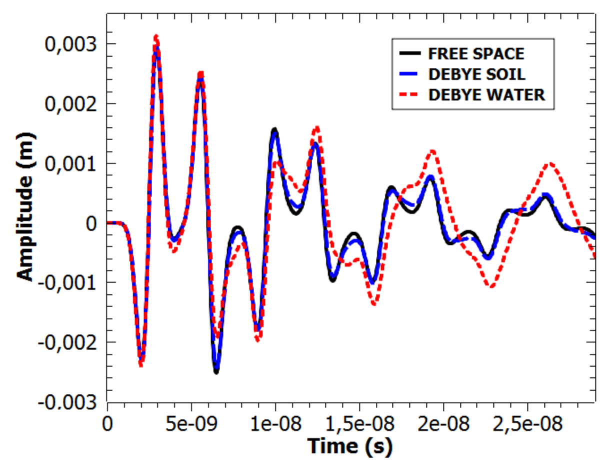

Fig. 5. Current at the center of the thin-wire antenna for the case of different Debye soils.

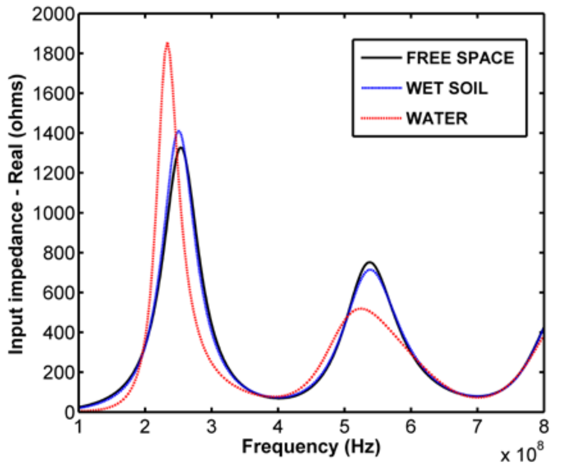

(a)

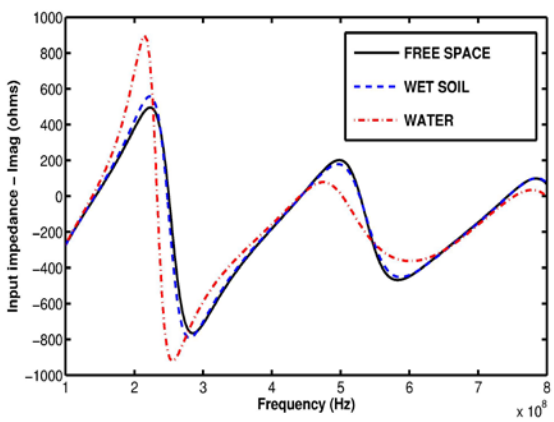

(b)

Fig. 6. Input impedance of the thin-wire antenna for the case of different Debye soils.

REFERENCES

[1] E. K. Miller and J. A. Landt, "Direct Time-Domain Techniques for Transient Radiation and Scattering from Wires," *Proc. IEEE*, vol. 68, pp. 1396-1423.

[2] F. Teixeira, "A Summary Review on 25 Years of Progress and Future Challenges in FDTD and FETD Techniques," *Applied Computational Electromagnetic Society (ACES) Journal*, vol. 25, no. 1, pp. 1-14, Jan. 2010.

[3] J. A. Huisman, S. S. Hubbard, J. D. Redman, and A. P. Annan, "Measuring Soil Water Content with Ground Penetrating Radar: A Review," *Vadose Zone J.*, vol. 2, pp. 476-491, 2003.

[4] J. Guerra and J. Eiras, "High Frequency Dielectric Relaxation in Lanthanum Modified PbTiO3 Ferroelectric Ceramics," *Material Research*, vol. 7, pp. 325-328, 2004.

[5] A. G. Tijhuis and A. Rubio Bretones, "Transient Excitation of a Layered Dielectric Medium by a Pulsed Electric Dipole," *IEEE Trans. Antennas and Prop.*, vol. 48, pp. 1673-1684, 2000.

[6] S. Makal and A. Kizilay, "A Decomposition Method for the Electromagnetic Scattering from a Coductive Object Buried in Lossy medium," *Applied Computational Electromagnetic Society (ACES) Journal*, vol. 26, no. 4, pp. 340-347, Apr. 2011.

[7] D. Poljak, *Advanced Modeling in Computational Electromagnetic Compatibil-ity*, John-Wiley&Sons, New Jersey, 2007.

[8] T. K. Sarkar, "Analysis of Abitrarily Oriented Thin Wire Antennas over a Plane Imperfect Ground," *Arch. Elek. Ubertrangungstech.*, vol. 31, pp. 449-457, 1977.

[9] M. Fernández Pantoja, A. G. Yarovoy, A. Rubio Bretones, and S. González García, "Time-Domain Analysis of Thin-Wire Antennas over Lossy Ground using the Reflection-Coefficient Approximation," *Radio Sci.*, vol. 44, RS6009, Dec. 2009.

[10] E. J. Rothwell, "Plane-Wave Impulse Response of a Debye Half-Space," *Electromagnetics*, vol. 27, pp. 195-206, 2007.

[11] Q. Zheng and G. Y. Delisle, "Transient Analysis of Plane Wave Reflection from a Debye Half Space," *Proc. Microsystems and Nanoelectronics Res. Conf.*, Ottawa, Canada, pp. 1-4, Nov. 2008.

[12] Z. Huang, K. R. Demarest, and R. G. Plumb, "An FDTD/MoM Hybrid Technique for Modeling Complex Antennas in the Presence of Heterogeneous Grounds," *IEEE Trans. on Geoscience and Remote Sensing*, vol. 37, no. 6, pp. 2692-2698, 1999.

[13] F. Edelvik, "A New Technique for Accurate and Stable Modeling of Arbitrarily Oriented Thin Wires in the FDTD Method," *IEEE Trans. on Electromagnetic Compatibility*, vol. 45, no. 2, pp. 416-423, 2003.

[14] H. Zhao and Z. Shen, "Weighted Laguerre Polynomials-Finite Difference Method for Time-Domain Modeling of Thin Wire Antennas in a Loaded Cavity," *IEEE Antennas and Wireless Propagation Letters*, vol. 8, pp. 1131-1134, 2009.

[15] C. A. Balanis, *Antenna Theory: Analysis and Design*, 3rd Ed., John Wiley & Sons, New York, 2005.

[16] T. J. Cui and W. C. Chew, "Accurate Model of Arbitrary Wire Antennas in Free Space, Above or Inside Ground," *IEEE Trans. Antennas Prop.*, vol. 48, pp. 482-493, 2000.

[17] G. J. Burke and E. K. Miller, "Modeling Antennas Near to and Penetrating a Lossy Interface," *IEEE Trans. Antennas Prop.*, vol. 32, pp. 1040-1049, 1984.

[18] G. J. Burke, E. K. Miller, J. N. Brittingham, D. L. Kager, R. J. Lytle, and J. T. Okada, "Computer Modeling of Antennas Near the Ground," *Electromagnetics*, vol. 1, pp 29-49, 1981.
[19] E. J. Rothwell, "Exponential Approximations of the Bessel Functions $I_{0,1}(x)$, $J_{0,1}(x)$, $Y_0(x)$, and $H_0^{(1,2)}(x)$ with Applications to Electromagnetic Scattering, Radiation, and Diffraction," *IEEE Antennas and Propag. Magazine*, vol. 51 (3), pp. 138-147, 2009.
[20] R. F. Harrington, *Field Computation by Moment Methods*, Mc-Millan, Florida, 1968.
[21] E. K. Miller, A. Poggio, and G. Burke, "An Integro-Differential Equation Technique for the Time-Domain Analysis of Thin-Wire Structures. Part I: The Numerical Method," *Journal of Computer Physics*, vol. 12, 1973.
[22] M. F. Pantoja, A. G. Yarovoy, and A. R. Bretones, "On the Direct Computation of the Time Domain Plane Wave Reflection Coefficients," *Applied Computational Electromagnetic Society (ACES) Journal*, vol. 24, no. 3, pp. 294-299, June 2009.
[23] E. G. Farr and C. A. Frost, "Impulse Propagation Measurements of the Dielectric Properties of Water, Dry Sand, Moist Sand and Concrete," *Measurement Notes* 52, Nov. 1997.
[24] J. Chen and J. Wang, "An Unconditionally Stable Subcell Model for Thin Wires in the ADI-FDTD Method," *Applied Computational Electromagnetic Society (ACES) Journal*, vol. 25 no. 8, pp. 659-664, Aug. 2010.
[25] A. Monorchio, A. R. Bretones, G. Manara, R. G. Martin, and R. Mittra, "A Hybrid Time-Domain Technique that Combines the Finite Element, Finite Difference and Method of Moment Techniques to Solve Complex Electromagnetic Problems," *IEEE Trans. Antennas and Prop.*, vol. 52, no. 10, pp. 2666-2674, Oct. 2004.
[26] N. Sachdeva, S. M. Rao, and N. Balakrishnan, "A Comparison of FDTD-PML with TDIE," *IEEE Trans. Antennas Prop.*, vol. 50, no. 11, pp. 1609-1615, Nov. 2002.
[27] F. L. Teixeira, W. C. Chew, M. Straka, M. L. Oristaglio, and T. Wang, "Finite-Difference Time-Domain Simulation of Ground Penetrating Radar on Dispersive, Inhomogeneous and Conductive Soils," *IEEE Trans. Geo. Remote Sensing*, vol. 36, no. 6, pp-1928-1937, Nov. 1998.
[28] K. P. Prokopidis and T. D. Tsiboukis, "Modeling of Ground-Penetrating Radar for Detecting Buried Objects in Dispersive Soils," *Applied Computational Electromagnetic Society (ACES) Journal*, vol. 22, no. 2, pp. 287-294, July 2007.

Mario Fernández Pantoja received the B.Sc., M.Sc., and Ph.D. degrees in Electrical Engineering from the University of Granada, Granada, Spain, in 1996, 1998, and 2001, respectively. Between 1997 to 2001, he was an Assistant Professor at the University of Jaen, Jaen, Spain. In 2001, he joined the University of Granada where, in 2004, he was appointed Associate Professor. He has been a Guest Researcher at the Dipartimento Ingenieria dell'Informazione, University of Pisa, Italy, the Antenna and Electromagnetics Group, Denmark Technical University, and Computational Electromagnetics and Antenna Research Laboratory from Pennsylvania State University. His research is mainly focused on the areas of interaction of electromagnetic waves with structures in time domain, and optimization methods applied to antenna design.

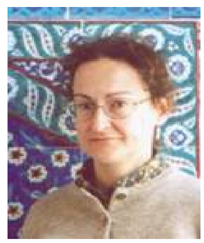

Amelia Rubio Bretones was born in Granada, Spain. She received the Ph.D. degree in Physics (cum laude) from the University of Granada, Granada, Spain, in 1988. Since 1985, she has been employed at the Department of Electromagnetism, University of Granada, first as an Assistant Professor, and then in 1989, as an Associate Professor, and finally, since 2000, as a Full Professor. On several occasions, she was a Visiting Scientist at the Delft University of Technology, Eindhoven University of Technology, and at The Pennsylvania State University. Her research interest is mainly in the field of numerical techniques for applied electromagnetics with an emphasis on time-domain techniques such as finite difference time domain, the application of the method of moments in the time domain for antenna and scattering problems, and hybrid techniques.

Salvador G. García received the M.S. and Ph.D. degrees (with extraordinary award), both in Physics, from the University of Granada (Spain), in 1989 and 1994, respectively. In 1999, he joined the Department of Electromagnetism and Matter Physics of the University of Granada as an Assistant Professor (with tenure). He has published over 30 refereed journal articles and book chapters, and over 70 conference papers and technical reports, and participated in several national and international projects with public and private funding. Dr. Garcia has received grants to stay as a visiting scholar at the University of Duisburg (Germany, 1997), Institute of Mobile and Satellite Communication Techniques (Germany, 1998), University of Wisconsin-Madison (USA, 2001) and University of Kentucky (USA, 2005). His current research interests include computational electrodynamics in the time domain, microwave imaging and sensing (GPR), bioelectromagnetics and antenna design.

X. Lucas Travassos received his B.Sc. and M.Sc. degrees from the Universidade Federal de Santa Catarina (Brazil) in 2002 and 2004, respectively. He finished his Ph.D. at the L'Ecole Centrale de Lyon (France) in 2007 with a thesis on NDT using ground penetrating radar techniques in cooperation with the University of Akron (USA). He is currently a research associate at SENAI-CIMATEC (Brazil) and his research interests are numerical modeling, non-destructive testing, and electromagnetic devices.

Rafael Gómez Martín received the M.S. degree from the University of Seville (Spain) in 1971 and the Ph.D. degree (cum laude) from the University of Granada (Spain) in 1974, both in Physics. Between 1971 and 1974, he was at the University of Santiago de Compostela (Spain) as a Ph.D. student. Between 1975 and 1985, he was Associate Professor at the University of Granada where in 1986 he became Full Professor. He is currently with the Department of Electromagnetism, where he is Head of the Electromagnetics Group. His current research interests include: the development of analytical and numerical methods in electromagnetism; antennas, ground penetrating radar; electromagnetic compatibility and biological effects of electromagnetic fields. He is the author of more than a hundred papers and is also the author of a book on advanced electromagnetics.

Design and Analysis of Multi-Frequency Unequal-Split Wilkinson Power Divider using Non-Uniform Transmission Lines

Derar Hawatmeh[1], Khair Al Shamaileh[2], and Nihad Dib[1]

[1] Department of Electrical Engineering, Jordan University of Science and Technology
P. O. Box 3030, Irbid 22110, Jordan
dfh_ee@hotmail.com, nihad@just.edu.jo

[2] Waseela for Integrated Telecommunication Solutions
P. O. Box 962487, Amman 11196, Jordan
khair.shamaileh@waseela-net.com

Abstract **─** In this paper, the design of miniaturized multi-frequency unequal-split Wilkinson power divider (WPD) using non-uniform transmission lines (NTLs) is presented. To achieve compactness, the uniform transmission lines of the conventional WPD are substituted by their equivalent NTLs. Moreover, two extra compact NTLs transformers are incorporated in each arm of the divider for output ports matching purposes. To prove the validity of the design procedure, two examples of single band and triple band NTL-based WPDs, with 2:1 split ratio, are presented. Both dividers are simulated using full-wave simulators. Furthermore, the proposed single band divider is fabricated and tested. Both simulation and measurements results are in good agreement. Besides the rejection of the odd harmonics over the band 1-5 GHz to a level lower than -15 dB, a total length reduction of 37%, and 16% in the single and triple band WPDs, respectively, is achieved.

Index Terms **─** Non-uniform transmission lines, power dividers, Wilkinson power divider.

I. INTRODUCTION

Microwave power dividers are essential components in modern microwave applications, such as antenna feed networks, phase shifters, and frequency mixers. Since its invention back in 1960 [1], the Wilkinson power divider (WPD) has been considered as one of the most important dividers in microwave circuits. Recently, WPDs have been notably addressed by researchers in many different aspects, such as reducing the size of their overall circuit area. The use of non-uniform transmission lines (NTLs) as one of the miniaturization techniques was presented in many papers [2-7]. In [2], an equal-split WPD was miniaturized using NTLs, and a size reduction of 52% was achieved. In [3], and as an extension to what was done in [2], a dual band WPD was proposed with 26% reduction in size (compared to the conventional dual-band one). In [4] and [5], NTL-based miniaturized Bagley power divider and branch line coupler, respectively, were presented. A general design procedure for NTL-based compact multi-band equal-split WPD was proposed in [6]. In [7], a reduced-size NTLs WPD, with modified topology, with high power split ratio was proposed in which the splitting ratio depends on the electrical lengths of its arms rather than the impedance values. Moreover, many miniaturization techniques were introduced in the literature to accomplish compactness, such as the use of stubs. In [8, 9], dual band compact WPDs were proposed in which stubs were incorporated to gain a significant size reduction of the circuit area. In [10], the WPD has been miniaturized using stubs, where artificial TLs have been used to accomplish the design. In [11], a stepped impedance interdigital coupling element has been incorporated to achieve the compactness for a single band WPD and to suppress the odd harmonics, as well.

Submitted On: Dec. 25, 2011
Accepted On: Feb. 23, 2012

In this paper, based on NTLs theory, a compact unequal-split WPD, with 2:1 split ratio, is presented. This is in contrast to [2, 3, 6], where equal-split NTLs WPDs were considered. To achieve compactness, the conventional uniform arms of the proposed dividers are replaced by their equivalent NTLs at specific design frequencies. The proposed divider is then simulated using two full-wave simulators to prove the validity of the design procedure. Furthermore, the designed single band unequal-split WPD is fabricated and measured, and both simulation and measurement results are in good agreement.

II. Design of compact NTLs

Figure 1 shows a schematic of the conventional unequal-split WPD, which can be designed using the following set of equations [12]:

$$Z_{02} = k^2 \times Z_{03} = Z_0 \times \sqrt{k \times (1 + k^2)}, \quad (1.\mathrm{a})$$

$$Z_{03} = Z_0 \times \sqrt{\frac{1 + k^2}{k^3}}, \quad (1.\mathrm{b})$$

$$R = Z_0 \times \left(k + \frac{1}{k}\right), \quad (1.\mathrm{c})$$

where Z_{02} and Z_{03} are the characteristic impedances of the upper and lower arms, respectively; k^2 is the power splitting ratio between ports 3 and 2, which equals to $\frac{P_3}{P_2}$, and R is the isolation resistor between the two output ports.

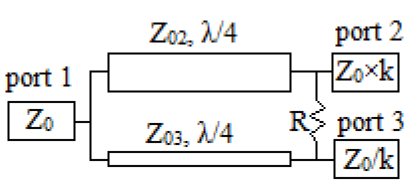

Fig. 1. A schematic of the conventional unequal-split WPD.

The key step in designing compact NTL-based WPD is to replace each arm of the conventional WPD with its equivalent NTL at a specific design frequency [2-7], keeping in mind that the length of the equivalent NTL should be less than the uniform transmission line's (UTL) length. Figure 2 shows a schematic of the proposed unequal-split NTL-based WPD.

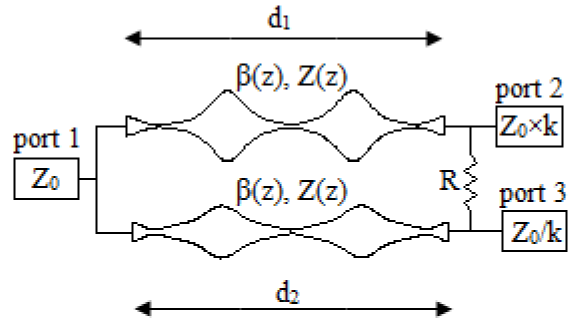

Fig. 2. A schematic of the unequal-split NTL-based WPD.

As shown in Figure 2, each equivalent NTL has varying characteristic impedance Z(z), and propagation constant β(z), compared to the conventional UTL, that has a constant characteristic impedance Z_0, and propagation constant β_0. The *ABCD* matrix of the UTL is given as follows [12]:

$$\begin{bmatrix} A_0 & B_0 \\ C_0 & D_0 \end{bmatrix} = \begin{bmatrix} \cos(\theta_0) & jZ_0 \sin(\theta_0) \\ \frac{j}{Z_0}\sin(\theta_0) & \cos(\theta_0) \end{bmatrix}, \quad (2)$$

where θ_0 is the electrical length of the UTL at the design frequency. In order to design the NTL section, it is firstly subdivided into a large number of uniform electrically short sections, and the overall *ABCD* matrix of the whole NTL can be obtained by multiplying the *ABCD* matrices of these uniform sections [2-7]. Then, the following truncated Fourier series expansion for the normalized characteristic impedance $\overline{Z}(z) = Z(z)/Z_0$ is considered:

$$\ln\left(\overline{Z}(z)\right) = \sum_{n=0}^{N} C_n \cos\left(\frac{2\pi nz}{d}\right). \quad (3)$$

An optimum designed compact NTL has to have its *ABCD* parameters as close as possible to the *ABCD* parameters of the UTL at a specific design frequency. For the single band NTL-based WPD, the optimum values of the Fourier coefficients C_n's can be obtained through minimizing the following error function [2, 5, 7, 13]:

$$Error = \sqrt{\frac{1}{4}\left(\left|A-A_0\right|^2 + Z_0^{-2}\left|B-B_0\right|^2 + Z_0^2\left|C-C_0\right|^2 + \left|D-D_0\right|^2\right)}. \qquad (4)$$

In the case of multi-band NTL-based WPD, the even-odd mode analysis carried out in [6] will be used. Figures 3 and 4 show the even and odd modes circuits of the NTL-based WPD, respectively. Using the even-mode equivalent circuits (Fig. 3), the NTLs are designed in such a way that the input reflection coefficient $|\Gamma_{in}|$ equals zero (or very small) at the design frequencies.

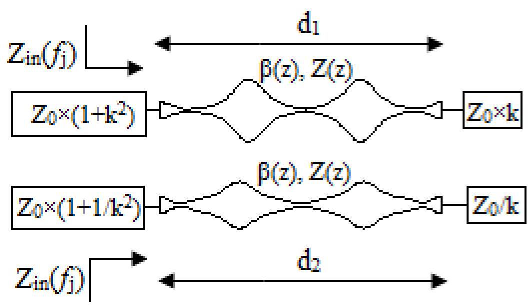

Fig. 3. Even-mode analysis of the unequal-split NTL-based WPD.

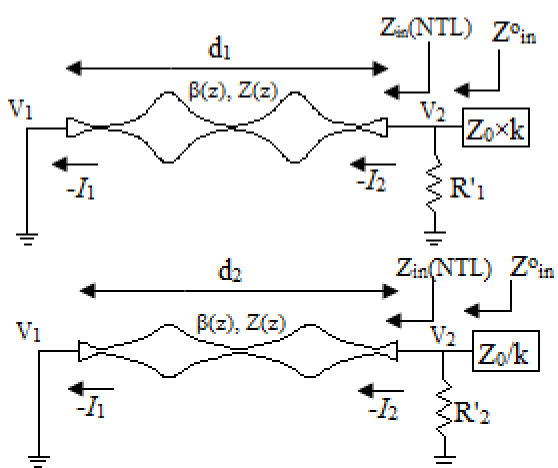

Fig. 4. Odd-mode analysis of the unequal-split NTL-based WPD.

Thus, the following error function, written in terms of the summation of the input reflection coefficients at M design frequencies $(f_j, j = 1, \ldots, M)$, is used [6]:

$$Error_{input} = \sqrt{\sum_{j=1}^{M} \left|\Gamma_{in}(f_j)\right|^2}, \qquad (5)$$

where,

$$\Gamma_{in}(f_j) = \frac{Z_{in}(f_j) - Z_s}{Z_{in}(f_j) + Z_s}, \qquad (6)$$

where Z_S is the source impedance expressed by $Z_0(1+K^2)$ and $Z_0(1+1/K^2)$ for the upper and lower arms shown in Figure 3, respectively. It is worth mentioning here that both error functions (4) and (5) should be restricted by some constraints, such as reasonable fabrication and physical matching, as follows:

$$\bar{Z}_{min} \le \bar{Z}(z) \le \bar{Z}_{max}, \qquad (7.a)$$

$$\bar{Z}(0) = \bar{Z}(d) = 1. \qquad (7.b)$$

These optimization problems are solved using the Matlab "fmincon" routine.

The isolation resistor is found using the odd-mode equivalent circuits shown in Figure 4, where the *ABCD* matrix of each branch can be written as follows:

$$\begin{bmatrix} V_1 \\ -I_1 \end{bmatrix} = \begin{bmatrix} A & B \\ C & D \end{bmatrix} \begin{bmatrix} V_2 \\ -I_2 \end{bmatrix}. \qquad (8)$$

Setting V_1=0 leads to:

$$AV_2 - BI_2 = 0. \qquad (9)$$

Solving for $\frac{V_2}{I_2}$,

$$\frac{V_2}{I_2} = \frac{B}{A} = Z_{in}^{NTL}. \qquad (10)$$

Finally, the input impedances for both upper and lower branches are given as follows, respectively:

$$Z_{in}^{0} = \frac{R_1'.Z_{in}^{NTL}}{R_1' + Z_{in}^{NTL}}, \qquad (11)$$

$$Z_{in}^{0} = \frac{R_2'.Z_{in}^{NTL}}{R_2' + Z_{in}^{NTL}}. \qquad (12)$$

Perfect output port matching for the upper and lower branches, respectively, can be achieved by satisfying the following conditions:

$$\Gamma_{out}(f_j) = \frac{Z^o{}_{in}(f_j) - Z_0K}{Z^o{}_{in}(f_j) + Z_0K}, \qquad (13.a)$$

$$\Gamma_{out}(f_j) = \frac{Z^o{}_{in}(f_j) - Z_0/K}{Z^o{}_{in}(f_j) + Z_0/K}. \qquad (13.b)$$

So, perfect output port matching at the design frequencies is achieved by keeping the output reflection coefficients as close as possible to zero by minimizing the following error function:

$$Error_{out} = \sqrt{\sum_{j=1}^{M} \left|\Gamma_{out}(f_j)\right|^2}, \qquad (14)$$

where R_1' and R_2' are the optimization variables that are determined using an optimization code. Clearly, the optimization must be run twice to find the value of the isolation resistor:

$$R = R_1' + R_2'. \qquad (15)$$

It is worth mentioning here that, compared to the conventional multi-band WPD [14], where a total number of M isolation resistors were used, the proposed multi-band NTL-based WPD has only one isolation resistor.

III. 2:1 NTL-based WPD

A. Single-band design

The conventional unequal-split WPD parameters can be calclulated using equations 1.a-1.c. Since the designed divider is of unequal-split type, output port 2 has an impedance of $R_2 = Z_0 \times k$, while output port 3 has an impedance of $R_3 = \frac{Z_0}{k}$ [12]. To obtain a 2:1 split ratio ($k^2 = 0.5$), the unequal-split WPD parameters are found to be: Z_{02}=51.5 Ω, Z_{03}=103 Ω, R=106.07 Ω, R_2=35.36 Ω and R_3=70.71 Ω (considering a reference impedance Z_0=50 Ω). Quarter-wavelength matching transformers are needed to match the output ports to 50 Ω. The characteristic impedances of these matching transformers are calculated as follows: for port 2: $\sqrt{35.36 \times 50} = 42.045\,\Omega$; and for port 3: $\sqrt{70.71 \times 50} = 59.46\,\Omega$. Now, each uniform microstrip line section is replaced by its equivalent compact NTL. Two output ports NTL matching transformers have been also designed. Considering an FR-4 susbtrate (with a thickness of 1.6 mm and dielectric constant of 4.6) and a design frequency of 1 GHz, the lengths (d) of the upper and lower WPD NTL arms are chosen to be 22.84 mm and 26.1 mm, respectively; while the lengths of the output ports matching transformers are chosen as 24.3 mm and 25.7 mm. It should be mentioned that the width of the upper (port 2) and lower (port 3) output ports at their ends are 3.92 mm and 2.18 mm, respectively; while the input port (50 Ω) width is 2.95 mm. Figure 5 shows the layout of the compact NTL-based 2:1 WPD compared to the conventional one. The proposed WPD is simulated using IE3D [15] and HFSS [16] full-wave simulators. The simulation results are shown in Figure 6, whereas Table 1 represents the values of the S-parameters at the design frequency.

Table 1: Values of the S-parameters of the single band NTL-based 2:1 WPD

		IE3D	HFSS	theoretical
At 1.0 GHz	S11 (dB)	-27	-25.55	$-\infty$
	S21 (dB)	-2.52	-2.4	-1.76
	S31 (dB)	-4.76	-4.77	-4.77
	S22 (dB)	-27.92	-25.1	$-\infty$
	S23 (dB)	-33.49	-23	$-\infty$
	S33 (dB)	-21.54	-24.94	$-\infty$

The slight differences between the theoretical and simulation results are thought to be due to dielectric losses, coupling, and discontinuities effects.

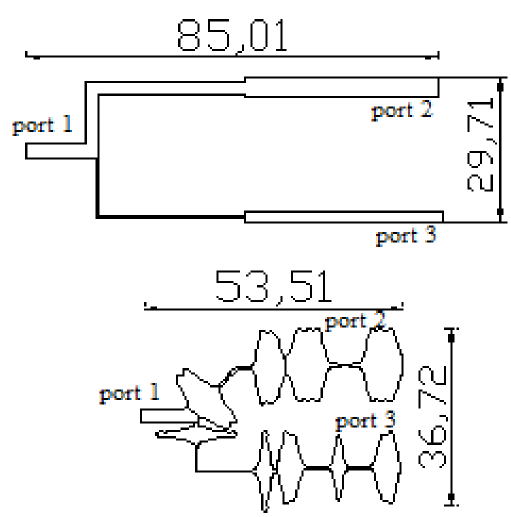

Fig. 5. The layout of the single-band NTL-based WPD compared to the conventional one (dimensions are in mm).

For verification purposes, the single band, NTL-based WPD is fabricated and measured using an Agilent Spectrum Analyzer (with a built in tracking generator extending from 0-1.5 GHz). Figure 7 shows the measured results, while Figure 8 shows a picture of the fabricated WPD.

Experimental results show an acceptable agreement between both simulated and measured results. The small discrepancies in the measured results could be due to conductor and dielectric losses, the use of the connectors and the errors in the measurements, keeping in mind that a spectrum analyzer (not a network analyzer) was used.

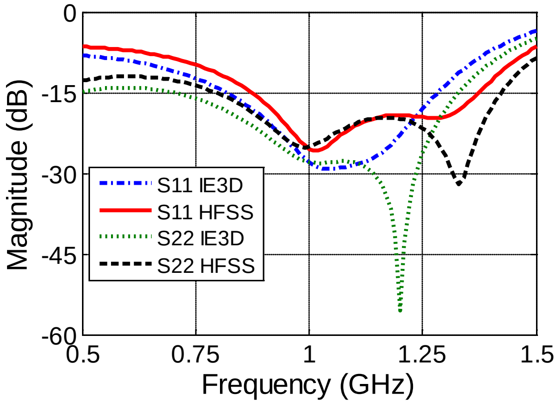

(a)

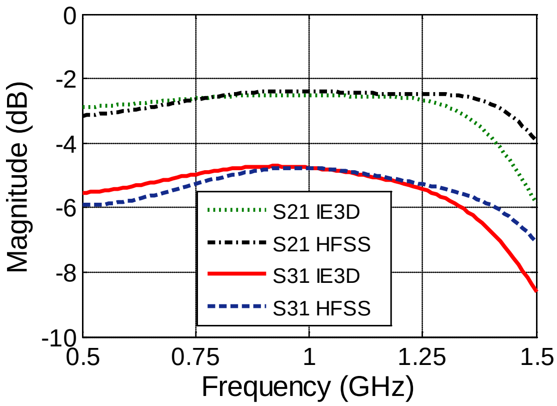

(b)

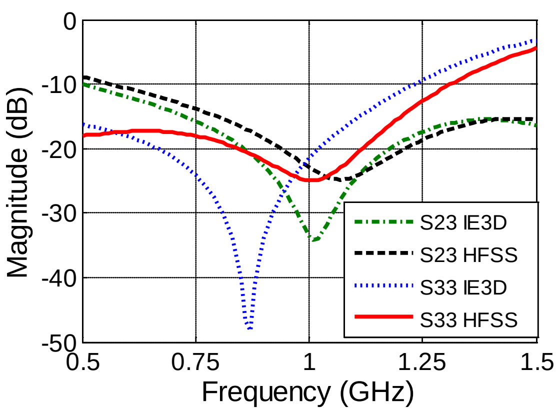

(c)

Fig. 6. S-parameters of the designed NTL-based WPD using IE3D and HFSS.

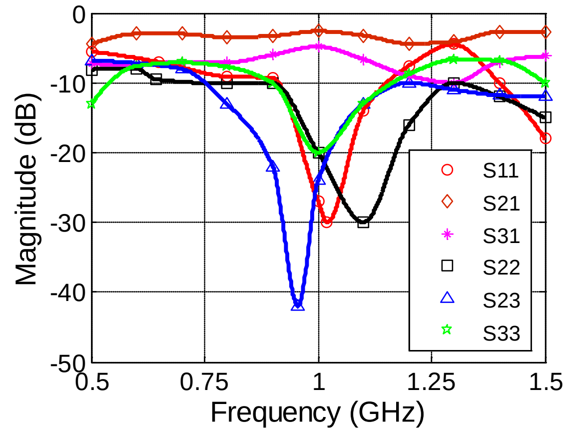

Fig. 7. Measured S-parameters of the fabricated NTL-based WPD.

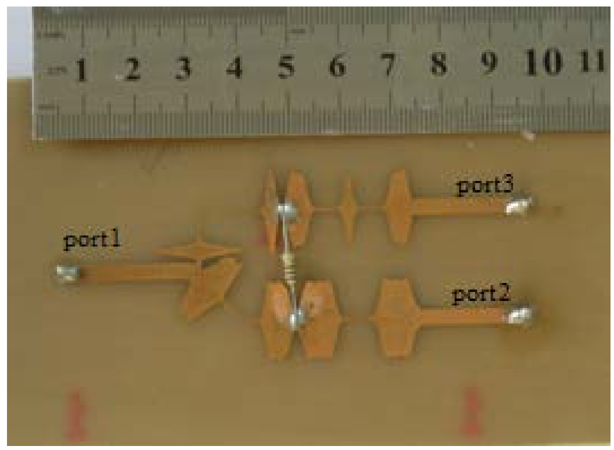

Fig. 8. Fabricated NTL-based 2:1 WPD.

B. Multi-band design

A triple frequency NTL-based 2:1 WPD is designed to operate at 0.5 GHz, 1.25 GHz, and 2 GHz, considering the same FR-4 substrate. The length of each WPD arm and output ports matching transformer is chosen to be $\frac{\lambda}{4}$ at the lowest design frequency. Using the design procedure described in the previous section, the layout of the designed triple band NTL-based WPD (compared to the conventional one) is shown in Figure 9. Three resistors (not shown in the figure) are needed in the conventional triple band WPD [14], while only a single one is needed in the NTL-based WPD.

The simulation results of the designed triple band NTL-based WPD (with an optimized isolation resistor of 105 Ω) are shown in Figure 10. A slight shift in the design frequencies is thought to be due to the coupling and discontinuity effects. The values of the S-parameters at the design frequencies are shown in Table 2.

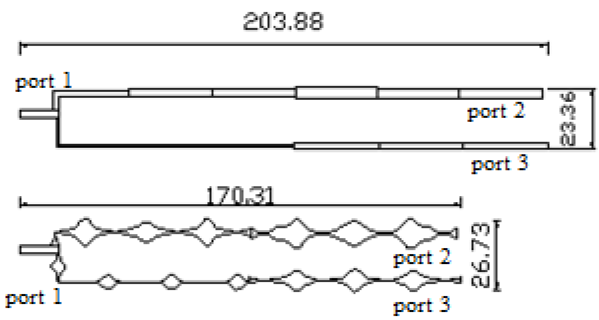

Fig. 9. The layout of the designed triple band NTL-based WPD compared to the conventional design (dimensions in mm).

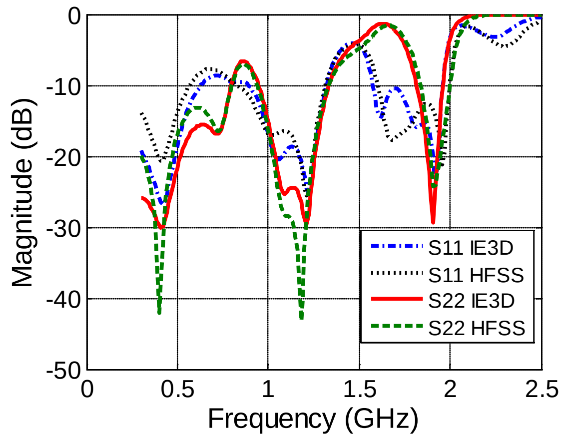

(a)

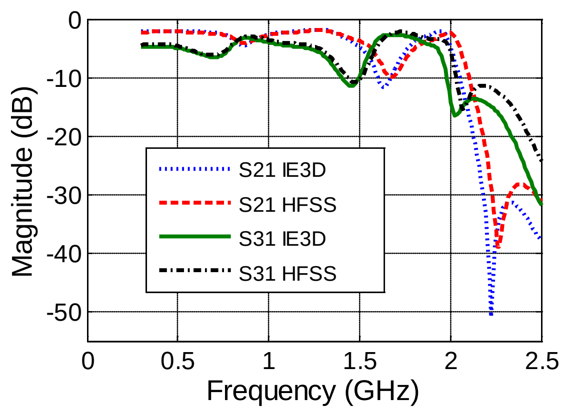

(b)

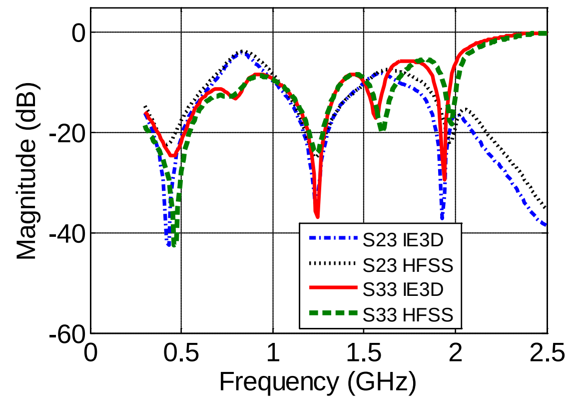

(c)

Fig. 10. S-parameters of the designed triple band NTL-based WPD.

Table 2: Values of the S-parameters of the triple band NTL-based 2:1 WPD

		IE3D	HFSS	theoretical
At 0.42 GHz	S11 (dB)	-26.7	-20.58	$-\infty$
	S21 (dB)	-2.03	-2.12	-1.76
	S31 (dB)	-4.7	-4.3	-4.77
	S22 (dB)	-29.9	-31.8	$-\infty$
	S23 (dB)	-41.9	-22.4	$-\infty$
	S33 (dB)	-23.37	-27.72	$-\infty$
At 1.22 GHz	S11 (dB)	-25.45	-25.4	$-\infty$
	S21 (dB)	-1.896	-2	-1.76
	S31 (dB)	-5.07	-4.42	-4.77
	S22 (dB)	-28.01	-25.6	$-\infty$
	S23 (dB)	-31.8	-24.24	$-\infty$
	S33 (dB)	-28.3	-22.6	$-\infty$
At 1.92 GHz	S11 (dB)	-23	-21.14	$-\infty$
	S21 (dB)	-2.	-2.7	-1.76
	S31 (dB)	-4.8	-3.7	-4.77
	S22 (dB)	-26.5	-17.7	$-\infty$
	S23 (dB)	-27	-20	$-\infty$
	S33 (dB)	-17.4	-15	$-\infty$

IV. COMPARISON BETWEEN CONVENTIONAL AND NTL-BASED WPDS

Using NTLs instead of UTLs, two main advantages are obtained: (1) the size reduction, and (2) the odd harmonics suppression. A total length reduction of almost 31 mm is achieved for the single band NTL-based WPD and about 33 mm for the triple band one. Since both structures have the same *ABCD* parameters at the design frequency only, the NTLs WPD behavior is completely different from the conventional one at other frequencies. Figure 11 shows the input port matching parameter (S_{11}) for both conventional and NTL-based single band WPD. It is clear that the third odd harmonic has been completely suppressed while the fifth odd harmonic is partially suppressed for the NTL-based WPD. Figure 12 shows S_{11} for both conventional triple band WPD and NTL-based triple band WPD. It is clear that the third and fifth odd harmonics are totally suppressed while the seventh odd harmonic is partially suppressed. Furthermore, a performance improvement is noticeable in the NTL-based WPD, since S_{11} is close to 0 dB at frequencies other than the design frequencies.

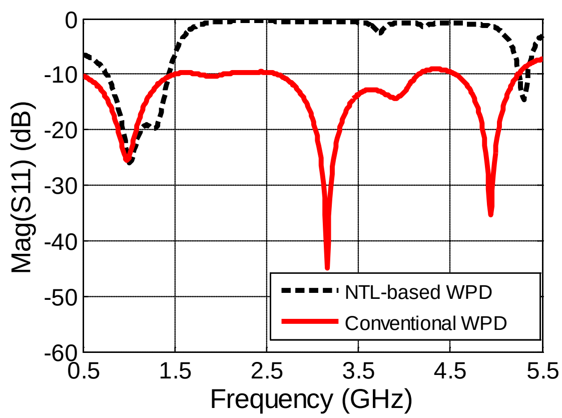

Fig. 11. S_{11} for both UTL-based and NTL-based single band WPDs.

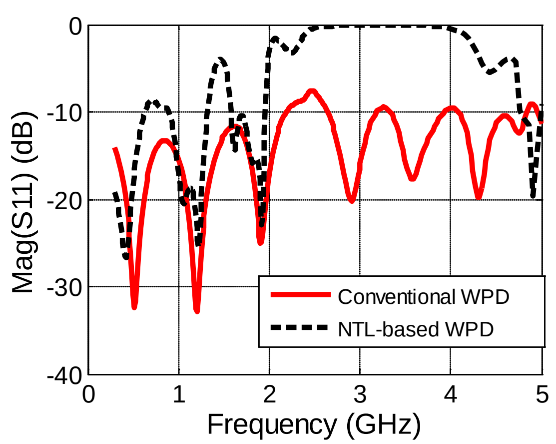

Fig. 12. S_{11} for both UTL-based and NTL-based triple band WPDs.

V. CONCLUSION

In this paper, the design and analysis of a compact 2:1 unequal-split NTL-based WPD was presented. In order to achieve compactness, each uniform transmission line was replaced by its equivalent NTL at the design frequency. Besides suppressing some of the odd harmonics of the design frequency, a length reduction about 30 mm was achieved compared to the conventional WPD. In addition to the length reduction and odd harmonics suppression, the number of isolation resistors in the multi-band design was reduced to one resistor regardless of the number of operation bands. This work will be extended to N-port, unequal-split multi-band WPD designs.

VI. ACKNOWLEDGMENT

This work was supported by the Deanship of Research at Jordan Univ. of Science and Technology (JUST).

REFERENCES

[1] R. Wilkinson, “An N-Way Hybrid Power Divider,” *IRE Transactions on Microwave Theory and Techniques*, vol. MTT-8, no. 1, pp. 116-118, 1960.

[2] F. Hosseini, M. Khalaj-Amir Hosseini, and M. Yazdani, “A Miniaturized Wilkinson Power Divider Using Non-uniform Transmission Line,” *Journal of Electromagnetic Waves and Applications*, vol. 23, pp. 917-924, 2009.

[3] K. Shamaileh and N. Dib, “Design of Compact Dual-Frequency Wilkinson Power Divider Using Non-uniform Transmission Line,” *Progress In Electromagnetics Research C*, vol. 19, pp. 37-46, 2011.

[4] K. Shamaileh, A. Qaroot, and N. Dib, “Non-Uniform Transmission Line Transformers and Their Applications in the Design of Compact Multi-Band Bagley Power Dividers with Harmonics Suppression,” *Progress In Electromagnetics Research*, vol. 113, pp. 269-284, 2011.

[5] F. Hosseini, M. Khalaj-Amir Hosseini, and M. Yazdany, “To Compact Ring Branch-Line Coupler Using Nonuniform Transmission Line,” *Microwave and Optical Technology Letters*, vol. 51, no. 11, pp. 2679-2682, Nov. 2009.

[6] K. Shamaileh, A. Qaroot, N. Dib, and A. Sheta, “Design and Analysis of Multi-Frequency Wilkinson Power Dividers Using Non-uniform Transmission Lines,” *International Journal of RF and Microwave Computer-Aided Engineering*, vol. 21, no. 5, pp. 526-533, September 2011.

[7] K. Shamaileh, A. Qaroot, N. Dib, and A. Sheta, “Design of Miniaturized Unequal Split Wilkinson Power Divider with Harmonics Suppression Using Non-Uniform Transmission Lines,” *Applied Computational Electromagnetics Society (ACES) Journal*, vol. 26, no. 6, pp. 530-538, June 2011.

[8] L. Shao, H. Guo, X. Liu, W. Cai, and L. Mao "A Compact Dual-Frequency Wilkinson Power Divider with Open-ended Stubs," *Int. Symposium on Signals Systems and Electronics (ISSSE)*, vol. 1, pp. 1-4, 2010.

[9] Z. Wang, J. Jang, and C. Park, "Compact Dual-Band Wilkinson Power Divider Using Lumped Component Resonators and Open-Circuited Stubs," *Wireless and Microwave Technology Conference (WAMICON)*, pp. 1-4, June 2011.

[10] C.-H. Tseng and C.-H. Wu, "Compact Planar Wilkinson Power Divider Using Pi-Equivalent Shunt-Stub-Based Artificial Transmission Lines," *Electronics Letters*, vol. 46, pp. 1327-1328, 2010.

[11] P. Cheong, K. Lai, and K. Tam, "Compact Wilkinson Power Divider With Simultaneous Bandpass Response and Harmonic Suppression," *IEEE MTT-S International Microwave Symposium Digest*, pp. 1588-1591, 2010.

[12] D. Pozar, Microwave Engineering, New York: John Wiley, 3rd edition, 2005.

[13] M. Khalaj-Amirhosseini, "Nonuniform Transmission Lines as Compact Uniform Transmission Lines," *Progress In Electromagnetics Research C*, vol. 4, pp. 205-211, 2008.

[14] A. Qaroot, N. Dib, and A. Gheethan "Design Methodology of Multi-Frequency Unequal Split Wilkinson Power Dividers Using Transmission Line Transformers," *Progress in Electromagnetics Research B*, vol. 22, pp. 1-21, 2010.

[15] IE3D, V 14, 2007, www.zeland.com.

[16] HFSS: High Frequency Structure Simulation based on Finite Element Method, V. 10, 2005, Ansoft Corporation, www.ansoft.com.

Derar Fayez Hawatmeh received his B.Sc. in Communications and Electronics Engineering from Jordan University of Science and Technology (JUST), Irbid, Jordan in 2010. In 2010, he joined the Master program in the Electrical Engineering Department at JUST majoring in Wireless Communications. His research interests include the analysis and design of antennas, compact, planar, passive, and multifrequency and ultra-wideband microwave components for wireless applications.

Khair Ayman Al Shamaileh received his B.Sc. in Communications and Electronics Engineering from Jordan University of Science and Technology (JUST), Irbid, Jordan in 2009. In the same year, he joined the Master program in the Electrical Engineering Department at JUST majoring in Wireless Communications. He received his M. Sc. degree in 2011. His research interests include the analysis and design of compact, planar, passive, multi-frequency and ultra- wideband microwave components for wireless applications.

Nihad I. Dib obtained his B. Sc. and M.Sc. in Electrical Engineering from Kuwait University in 1985 and 1987, respectively. He obtained his Ph.D. in EE (major in Electromagnetics) in 1992 from University of Michigan, Ann Arbor. Then, he worked as an assistant research scientist in the radiation laboratory at the same school. In Sep. 1995, he joined the EE department at Jordan University of Science and Technology (JUST) as an assistant professor, and became a full professor in Aug. 2006. His research interests are in computational electromagnetics, antennas and modeling of planar microwave circuits.

Switched Band-Notched UWB/ WLAN Monopole Antenna

Guangmin Zhang[1,2], Jin-song Hong[1], Bing-zhong Wang[1], and Gangbing Song[2]

[1]Institute of Applied Physics
University of Electronic Science and Technology of China, Chengdu, 610054, People's Republic of China
zgm2177702019@hotmail.com, cemlab@uestc.edu.cn, bzwang@uestc.edu.cn

[2]Department of Mechanical Engineering
University of Houston, Houston, TX, 77204, USA
gsong@central.uh.edu

Abstract **─** A switched band antenna that has a capability to operate in tri-band WLAN frequency band (2.4–2.485 GHz, 5.15-5.35 GHz and 5.725-5.825 GHz) and a band-notched UWB frequency band (the stop-band covers the frequency range from 5.15 GHz to 5.825 GHz) is presented. The antenna uses a switchable ground and a switchable monopole patch to provide a switched band property. To the authors' knowledge, the proposed antenna represents a feature that is unique to this paper.

Index Terms **─** Band-notched UWB, switched band, WLAN.

I. INTRODUCTION

Communication technologies have been growing rapidly in recent years. One of the breakthroughs is that the single system can be integrated with several applications, such as ultra-wide band (UWB) communications, satellite communications, and wireless local area networks (WLAN). Since these applications operate at different frequency bands, those wireless systems request the antennas can operate in various frequency bands. Therefore, to meet the demands of those systems, various frequency reconfigurable antennas which can adjust their operating frequency bands are developed. Some investigators tuned the operating bands of the frequency reconfigurable antennas by changing sizes of the radiator [1-3], such as the length of the dipoles [1-2]. The frequency reconfigurable antenna can provide the switchable operating frequency characteristic by changing the number of the shorting strips [4]. However, most of the frequency reconfigurable antennas provide only one narrow operating band in the wide frequency ranges [1-6]. Those characteristics can not meet some wideband communication demands, for example UWB communication. The researchers use the switchable ring resonators to make the antenna work in a wide band or the dual band of WLAN [7]. However, the operating bands of the antenna can not cover band-notched UWB frequency band and tri-band WLAN frequency band via changing its operation modes [7].

A novel frequency-reconfigurable planar antenna is developed in this paper. The proposed antenna is composed of three switches, a reconfigurable monopole patch, and a switchable ground plane. By controlling the states of the switches, the proposed antenna is able to provide two operation modes whose operation bands can cover 2.45/5.2/5.8 GHz WLAN band (2400-2483 MHz, 5150-5350 MHz, 5725-5825 MHz) and the band-notched UWB band (the stop-band covers the frequency range from 5.15 GHz to 5.825 GHz), respectively. In this study, all switches create a 1 mm gap when they are in the close state and short the gap when in the open condition. Therefore, for the proof of concept [7], the "OFF" state is obtained by an air gap of 1 mm. The "ON" condition is realized by hard-wiring the air gap.

Submitted On: Oct. 27, 2011
Accepted On: Jan. 28, 2012

II. ANTENNA CONFIGURATIONS

Figure 1 shows the geometry of the proposed antenna. In this study, the FR4 substrate of thickness 1 mm and relative permittivity 4.6 is used. A monopole patch and a 50Ω microstrip feeding line are printed on the same side of the dielectric substrate. The conducting switchable ground plane is printed on the other side of the substrate. Two rectangle slots are etched on the ground plane. To achieve the desired frequency reconfigurability, two switches are placed over the upper section of the ground plane, while another switch is located on the monopole patch. When switch 1 is in the "ON" state and other switches are in the "OFF" state, the proposed antenna operates in tri-band WLAN mode. When switch 1 is in the "OFF" state and other switches are in the "ON" state, the proposed antenna operates in the band-notched UWB mode.

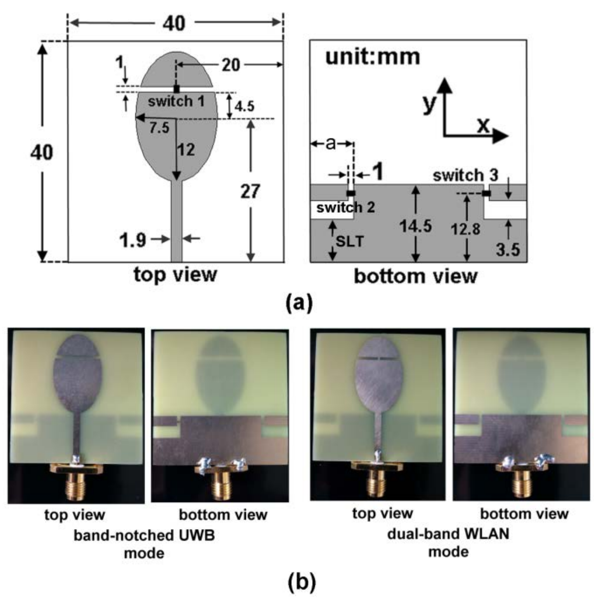

Fig. 1. Structure of the proposed antenna. (a=7mm, SLT=8mm)(a) Top view and bottom view.(b) Photos of the proposed antenna.

III. RESULTS AND DISCUSSION

The measured and simulated bandwidths of the proposed antenna are illustrated in Fig. 2. The measurement was taken by an Agilent E5071C network analyzer, and the simulations are performed using CST Microwave Studio in this study. The Agilent E5071C network analyzer has the highest measurable frequency at about 8 GHz. Though it does not cover the whole UWB band (3.1-10.6 GHz), it reaches our requirements since we were concerned with where the notch-band of the band-notched UWB mode and the triple bands of the WLAN mode are in the measurable band.

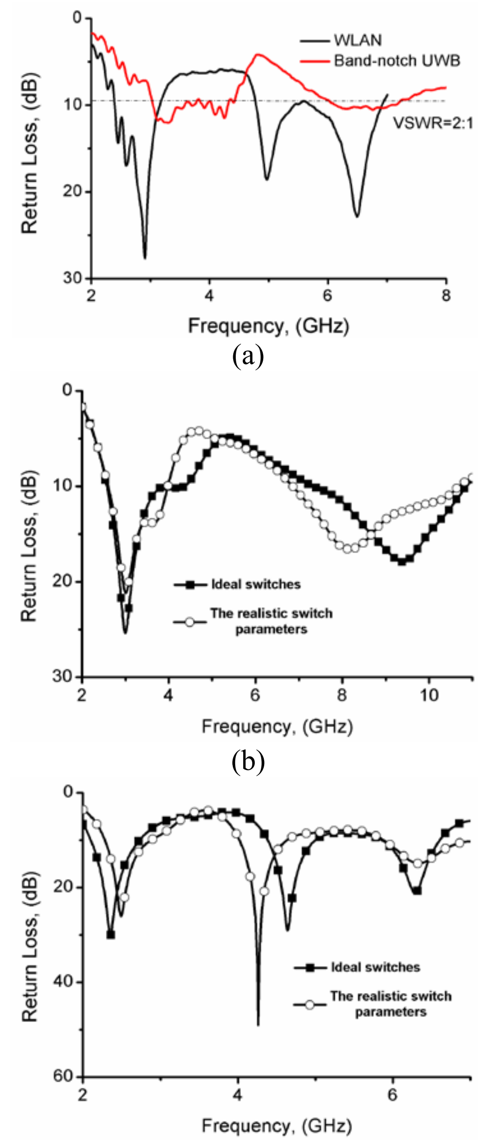

Fig. 2. Return losses of the proposed antenna in two modes: (a) measured results, (b) simulated results in the band-notched UWB mode, (c) simulated results in the Tri-band WLAN mode.

In the tri-band WLAN mode, the lower band for VSWR ≤ 2 ranges from 2.39GHz to 3.18GHz, and the higher band scans from 4.77 to 6.94GHz for VSWR ≤ 2. In the band-notched UWB mode, a stop-band ranging from 4.43 to 6.02 GHz for VSWR>2 is obtained. There is some discrepancy between the simulated result and the measured result. One of the reasons for such discrepancy is the fabrication and measurement tolerance of the proposed antenna, the other is the ideal excitation port which can not simulate the real SMA connector and the weld connecting the SMA connector to the proposed antenna. Despite those nonideal effects during the fabrication and measurement, the impedance responses in Fig. 2 still sustain the consistency of the band reconfigurability of the proposed design.

The return losses of the proposed antenna with the realistic switch parameters in the two modes are also shown in Fig. 2. The RF equivalent circuit of a PIN diode, MACOM MA4AGBPL912 [8], was used and shown in Fig. 3. Since the realistic switch parameters can change impedance of the proposed antenna, it can be seen that the resonant frequencies of the tri-band WLAN mode and the notch band of band-notched UWB mode shift compared with those with the ideal switches.

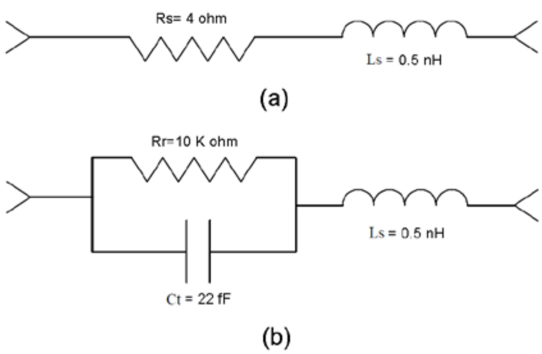

Fig. 3. RF equivalent circuit for the PIN diode in the (a) ON state and (b) OFF state.

Figure 4 displays the radiation patterns of the two modes in three plane-cuts, the x-y plane, the x-z plane, and the y-z plane. All radiation patterns of the tri-band WLAN mode and the band-notched UWB mode are roughly omni-directional. The broadside directions of the two modes are roughly identical. That means the system can remain stable when the antenna switches between the tri-band WLAN mode and the band-notched UWB mode.

It is worthwhile to mention that the two slots etched on the ground play important roles in the proposed design. When the proposed antenna operates in the WLAN mode, the two slots are located outside the ground. As a result, an inverted T-shaped ground plane which can generate two various bands is formed. When the proposed antenna works in the band-notched UWB mode, the two rectangle slots are etched on the ground and act as a stop-band filter to notch the 5.2-GHz and 5.8-GHz WLAN bands.

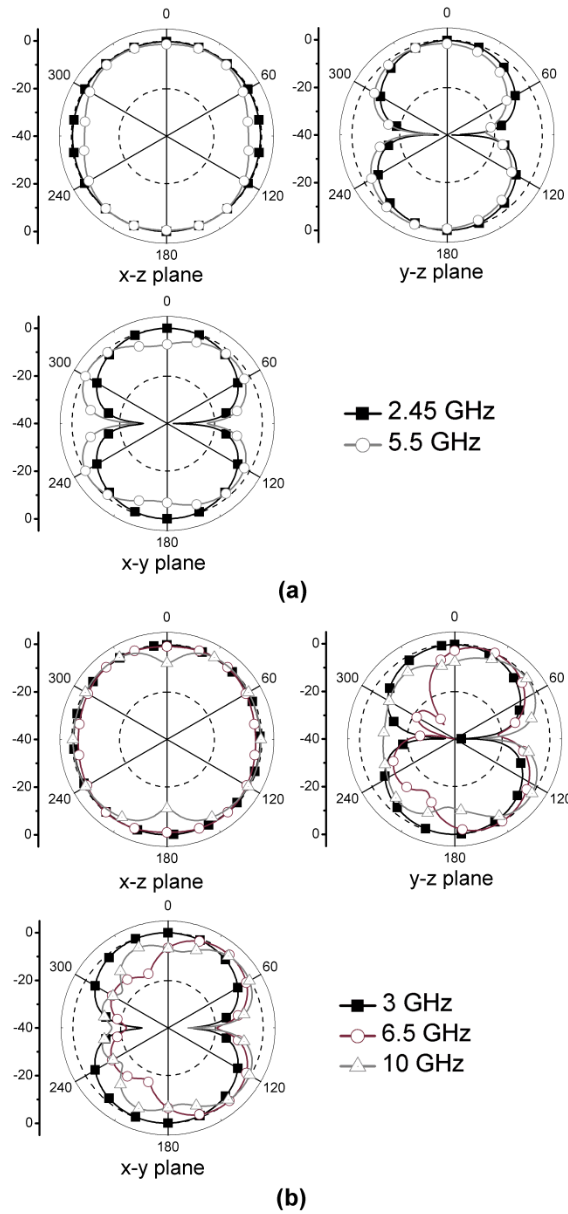

Fig. 4. Simulated radiation patterns of the antenna in two modes: (a) tri-band WLAN mode, (b) band-notched UWB mode.

To validate the above concept, the return losses of the proposed antenna with various parameter ***a*** in the WLAN mode and the band-notched UWB mode are shown in Fig. 5. The length of the two rectangle slots extends with the increase of the parameter ***a***. That causes the current path in the notch band to be lengthened. Therefore, it can be seen that the stop-band frequency of the band-notched UWB mode lowers with the increase of the value of parameter ***a***. Furthermore, when the value of parameter ***a*** is increased, the length of the rectangle slots is closer to half a wavelength at the center frequency of the notch band, leading to the improvement of the rejection level. The increase of the parameter ***a*** also causes the decrease of the width of the vertical portion of the T-shaped ground plane. Since the T-shaped ground plane is a 2-order stepped-structure, the decrease of the width of the vertical portion makes the impedance of the proposed antenna mismatch, as Fig. 5 (b) shows.

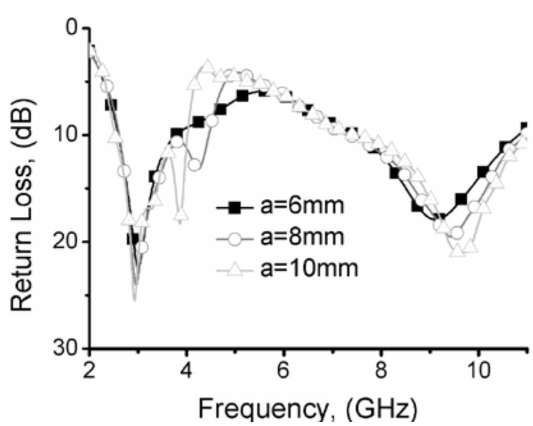

(a)

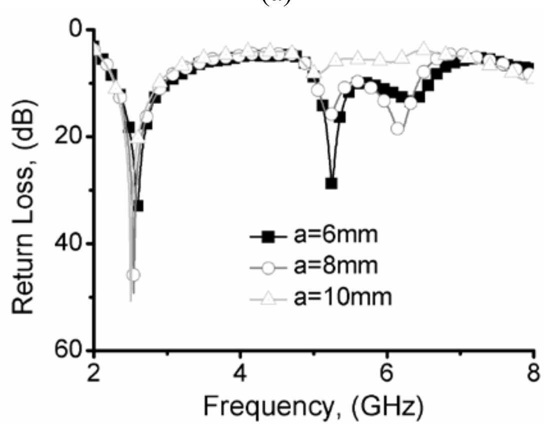

(b)

Fig. 5. Simulated return losses of the proposed antenna with various ***a***: (a) the band-notched UWB mode, (b) the WLAN mode.

In addition, the return losses of the proposed antenna with various SLT in the two modes are shown in Fig. 6. Since the rectangle slots are closer to the signal port with the decrease of the SLT, the resonant current around the rectangle slots is strengthened, which means the effective current path is increased. As a result, the rejection level can be improved. However, since the shape of the T-shaped ground plane vary with the decrease of SLT, the higher band of the WLAN mode is narrowed.

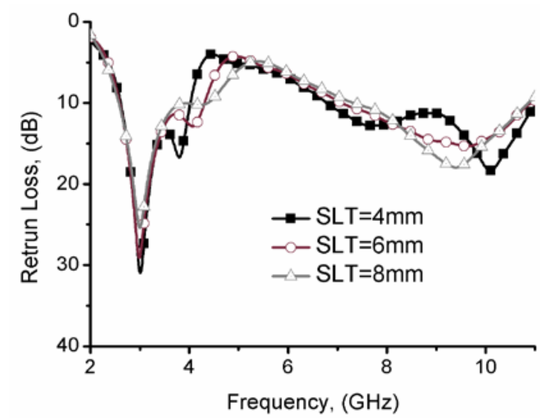

(a)

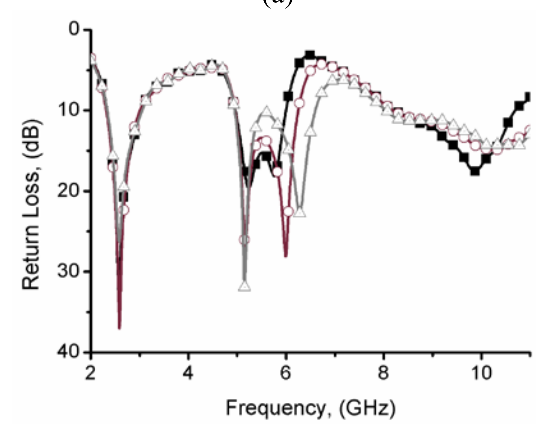

(b)

Fig. 6. Simulated return losses of the proposed antenna with various SLT: (a) the band-notched UWB mode, (b) the WLAN mode.

IV. CONCLUSION

A novel frequency-reconfigurable antenna is developed in this letter. By switching between the ON and OFF status of the switches, the proposed antenna can allow the system to operate in two modes, the tri-band WLAN mode and the band-notched UWB frequency mode. As a result, the proposed antenna can be used in the tri-band WLAN system and the UWB system.

ACKNOWLEDGMENT

This work was supported by the National Natural Science Foundation of China (No.61172115 and No.60872029), the High-Tech Research and Development Program of China (No. 2008AA01Z206), the Aeronautics Foundation of China (No.20100180003), and the Fundamental Research Funds for the Central Universities (No. ZYGX 2009J037). Academic new artist Ministry of education doctoral post graduate (No.A01002203901073). Project 9140A01020110DZ0211 and CSC Project 2010607042.

REFERENCES

[1] P. Qin, A. R. Weily, Y. J. Guo, T. S. Bird, and C. Liang, "Frequency Reconfigurable Quasi-Yagi Folded Dipole Antenna," *IEEE Trans. Antennas Propag.*, vol. 58, no. 8, pp. 2742-2747, 2010.

[2] Y. Cai, Y. J. Guo, and A. R. Weily, "A Frequency-Reconfigurable Quasi-Yagi Dipole Antenna," *IEEE Antennas Wireless Propag. Lett.*, vol. 9, pp. 883-886, 2010.

[3] Y. Yu, J. Xiong, H. Li, and S. He, "An Electrically Small Frequency Reconfigurable Antenna with a Wide Tuning Range," *IEEE Antennas Wireless Propag. Lett.*, vol.10, pp.103 - 106, 2011.

[4] J. Row and T. Lin, "Frequency-Reconfigurable Coplanar Patch Antenna with Conical Radiation," *IEEE Antennas Wireless Propag. Lett.*, vol. 10, pp. 1088-1091, 2010

[5] C. W. Jung, Y. J. Kim, Y. E. Kim, and F. F. De, "Macro-Micro Frequency Tuning Antenna for reconfigurable Wireless Communication Systems," *Electron. Lett.*, vol. 43, pp. 201-202, 2007.

[6] S. Xiao, B. Z. Wang, and X. S. Yang, "A Novel Frequency Reconfigurable Patch Antenna," *Microw. Opt. Technol. Lett.*, vol. 36, pp. 295-297, 2003.

[7] M. R. Hamid, P. S. Hall, P. Gardner, and F. Ghanem, "Switched WLAN-Wideband Tapered Slot Antenna," *Electron. Lett.*, vol. 46, no. 1, pp. 23-24, 2010.

[8] MA4AGBLP912, M/A-COM Technology Solutions Inc. [Online]. Available: www. macomtech.com

Dipole Antenna Miniaturization using Single-Cell Metamaterial

Amir Jafargholi and Manouchehr Kamyab

Department of Electrical Engineering
K. N. Toosi University of Technology, P.O.Box 16315-1355. Tehran, Iran
Jafargholi@ee.kntu.ac.ir, Kamyab@kntu.ac.ir

Abstract **─** Miniaturized printed dipole antenna loaded with reactive elements is proposed. The reactive loading of the dipole is inspired by the epsilon-negative (ENG) and double negative (DNG) metamaterial (MTM) inclusions, which enable the loaded dipole to be compacted. The reactive loads are realized by two rake-shaped split ring resonators (SRRs) facing each other. Investigations reveal that the loaded dipole radiates at two separated bands depending on load locations. The new resonance frequencies are lower than the natural resonance frequency of the conventional half wavelength dipole. In this range of frequencies, the radiation efficiency of the composite antenna is high. In order to validate the simulation results, a prototype of the proposed printed dipole is fabricated and tested. The agreement between the simulated and measured results is quite good.

Index Terms **─** Loaded dipole, metamaterial.

I. INTRODUCTION

The increasing demands on compact multifunctional devices have necessitated the development of miniaturized/multi-frequency printed dipoles which can be integrated into familiar devices such as laptop computers and mobile phones. The typical difficulties encountered in designing compact antennas include narrow bandwidth, and low radiation efficiency. In order to achieve a good efficiency, considerable effort must be expended on the matching network. Other researchers have found that the bandwidth of the dipole antenna can be enhanced by loading the antenna with parallel lumped element circuits [1]. Over the last decade, increasing demands for low profile multifunctional antennas have resulted in considerable interest by the electromagnetic research community in MTMs. Due to unique electromagnetic properties; MTMs have been widely considered in monopole and dipole antennas to improve their performance [2-5]. The applications of composite right/left handed (CRLH) structures to load the printed dipole have been investigated both numerically [6-8] and analytically [9]. However, the main drawbacks of this method are low gain and low efficiency. The use of transmission-line based MTMs to realize a tri-band monopole antenna has been recently investigated in [10]. However, the cross polarization levels of the proposed antenna in [10] are very high. It is also known that the antenna properties can be improved by covering the metal radiating parts or filling the antenna volume. For instance, the bandwidth of the microstrip patch antenna can be significantly improved by replacing the dielectric substrate with the magneto-dielectric one [11]. The effect of complex material coverings on the bandwidth of the antennas has been also investigated in [12].

In this paper, first, the effect of material inclusions embedded in a simple dipole antenna has been investigated. The numerical investigations result in some general conclusions regarding the effect of material inclusions on the dipole antenna performance. It is demonstrated that in contrast to the double-positive (DPS) and mu-negative (MNG) MTMs, ENG-, and DNG-MTM inclusions can provide miniaturization and multi-band performance. To practically realize this method, a compact printed dipole antenna is designed using reactive loading, which is inspired by ENG-MTM inclusions.

Submitted On: Aug. 16, 2011
Accepted On: Jan. 26, 2012

To this aim, a novel printed MTM element is proposed and successfully tested. The proposed MTM cell shows ENG behavior at around the antenna operating frequency. The dimensions of the proposed MTM cell is optimized to meet the specifications of the mobile bands (890.2MHz–914.8MHz, and 1710MHz–1784MHz) while maintaining its compact size. The antenna radiation efficiency at the first resonance frequency is significantly higher than those reported for other miniaturized dipoles in the literature [6-9]. It is worthwhile to point out here that the subject of single-cell MTM loading is not new and has been studied by other authors [10].

II. LOADED DIPOLE ANTENNA WITH MTM INCLUSIONS

The resonance frequencies of an original monopole/dipole are harmonics of the main resonant frequency ω_1. However, omnidirectional radiation pattern distortion and low directivity are two major disadvantages associated with monopole/dipole antenna resonating at higher order harmonics ($\omega_m>\omega_1$) [5, 13]. In this section, a simple and intuitive rule for determining the beneficial filling material type for dipole antennas has been introduced. A dipole antenna loaded with cylindrical dispersive MTM inclusions is shown in Fig. 1. It is assumed that the MTM inclusions are embedded in the both arms of the dipole. Here, the Drude model [14] is used to simulate the MTM inclusions, since it can yield a negative real part of the permittivity/permeability over a wide frequency range. Depending on the MTM type either μ or ε (or both) obey the Drude model (plasma frequency $\omega_p=1.8\times10^{10}$ rad/s and collision frequency f_c=0.2GHz) and are equal to one otherwise. The distance from the location of the MTM inclusions to the feed point is denoted as d_{MIF}. The behaviors of the loaded dipole as a function of the MTM type, the distance of the MTM inclusions from the antenna feed point, d_{MIF}, and inclusion width have been studied here.

The computation time for the DPS inclusion is about 10 minutes for all frequency points compared to about an hour for a DNG case using CST over a frequency range of 0 to 6GHz, while this time increased in CST for higher permittivity and permeability materials. (For a 3.2GHz dual core CPU with 2GByte RAM).

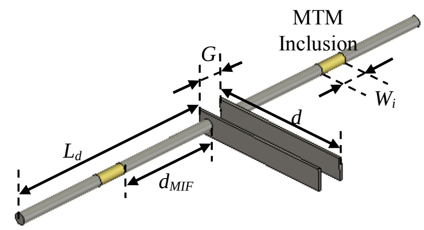

Fig. 1. An ideal model of MTM loaded dipole: L_d=120mm, W_i=2.5mm, G=5mm, d=27mm.

2.1. Power reflection coefficient, $|S_{11}|$ as a function of MTM distance from the antenna feed point

Figure 2, shows the antenna return loss for the dipoles loaded with DPS-, MNG-, DNG-, and ENG-inclusions, with d_{MIF} as a parameter. As the ENG- or DNG- inclusions are added, the antenna resonant behavior changes. It can be concluded from Fig. 2 that for the dipole antenna loaded with DNG- or ENG-inclusions, an additional resonance frequency is introduced at the frequencies lower than the antenna resonant frequency where the antenna radiates an omnidirectional radiation pattern. In contrast, for the dipoles loaded with DPS- or MNG-inclusions, changing DPS/MNG locations on the antenna arms causes no resonances at frequencies lower than the main resonance frequency, as shown in Figs. 2a and 2b. As the distance between the ENG-/DNG-inclusions and the feed point is increased, the main resonant frequency decreases while the low resonant frequency is almost unchanged. This feature provides the ability to choose the second resonance frequency arbitrarily based on provision dictated by application. Thus, the frequency ratio between these two frequencies can be readily controlled by adjusting the inclusion locations. In addition, for the case of the dipoles loaded with DNG-/ENG-blocks and 50mm<d_{MIF}<75mm, more than one resonance is introduced at around the antenna main resonant frequency where the antenna radiates omnidirectional radiation patterns, as shown in Figs. 2b and 2c. To make the concept clearer, three DNG loaded dipoles are designed and simulated. The return loss results for the dipole antennas loaded with different DNG blocks and different d_{MIF} are shown in Fig. 3. For comparison purposes, the power reflection coefficient of an unloaded dipole antenna is also presented in Fig. 3. As can be seen, all the antennas have multi-resonance behavior.

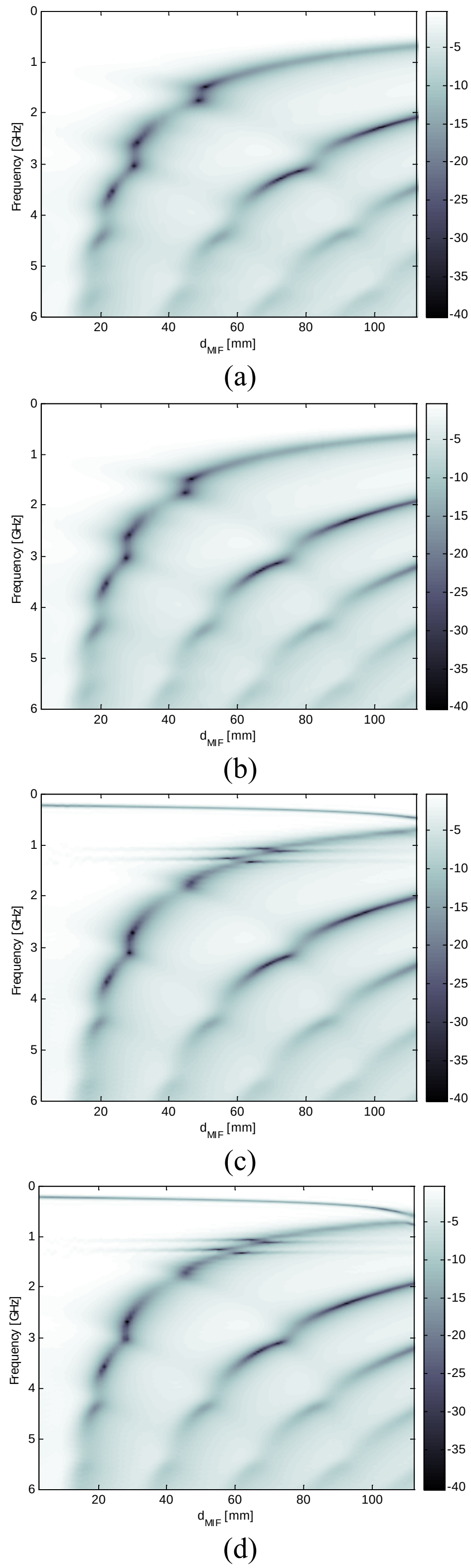

Fig. 2. CST Simulation Results for $|S_{11}|$ [dB], (a) DPS-, (b) MNG-, (c) DNG-, and (d) ENG-inclusions.

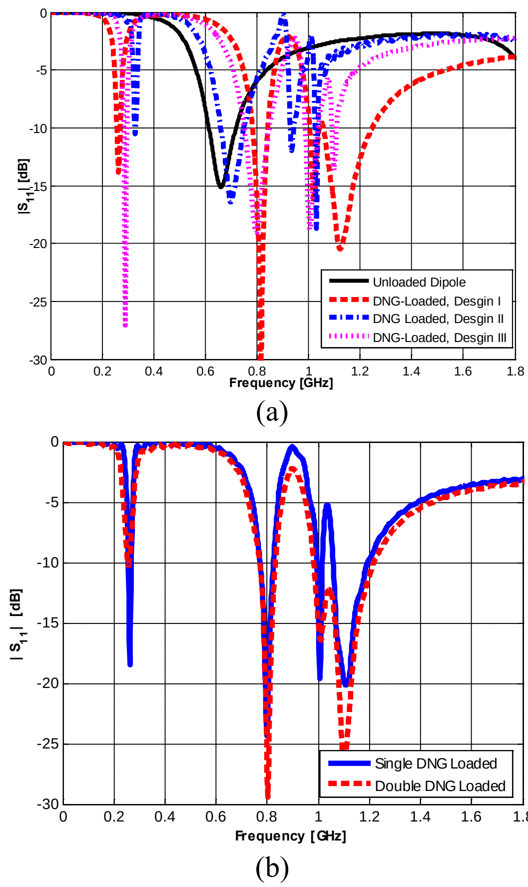

Fig. 3. Magnitude of S_{11} (a) of dipole antennas loaded with different DNG blocks, with Drude model and $\omega_p=1.8\times10^{10}$ rad/s; Design I: d_{MIF}=72mm and, f_c =0.2GHz, Design II: d_{MIF}=100mm, f_c =0.01GHz, and Design III: d_{MIF}=85mm, f_c =0.1GHz. As a reference, an unloaded dipole antenna is also simulated, (b) comparison for single and double loaded DNG materials: The first inclusions are located at d_{MIF}=72mm while the second ones are located at the ends of the arms, f_c=0.1GHz.

The first frequency bands of the proposed loaded dipoles are narrow. These narrow frequency bands are the direct consequence of the resonant nature of the MTM inclusions. The gain, efficiency, and bandwidth of the three loaded dipoles are compared in Table 1. For the first design, the antenna bandwidth at first resonance is quite good but its gain is low. In contrast, for the second design, the antenna has a high gain at the first resonance frequency but at the expense of a narrower bandwidth. As a result, the type of the

DNG-inclusion is a result of a trade-off between the antenna gain and bandwidth (Design III).

2.2. Power reflection coefficient, $|S_{11}|$ as a function of MTM type

In this section, the effects of two different cases of metamaterial inclusion have been investigated.

A. Non-dispersive materials

In Fig. 4, the effect of permittivity and permeability of DPS inclusion on the antenna resonance frequency has been studied. Increasing DPS load permittivity cases resonance frequency decreasing while, for the dipoles loaded with magnetic inclusions, changing permeability causes no resonance frequency change.

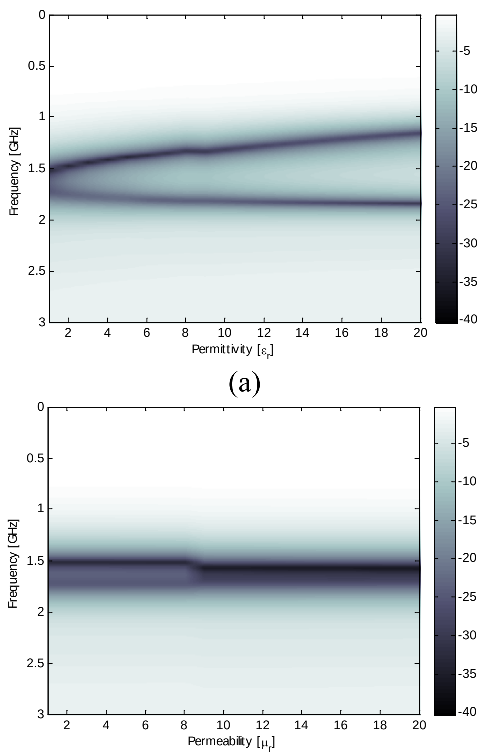

(a)

(b)

Fig. 4. CST simulation results for $|S_{11}|$ [dB], d_{MIF}=45mm, versus material (a) permittivity, μ_r=1, and (b) permeability, ε_r=1.

B. Dispersive materials

The behaviors of the loaded dipole as a function of the plasma frequency for d_{MIF}=72mm, have been studied. Figure 5 shows the antenna return loss for the dipoles loaded with ENG-, DNG-, and MNG-inclusions. It can be concluded from Fig. 5 that for a dipole antenna loaded with DNG- or ENG-inclusions, an additional resonance frequency is introduced at the frequencies lower than the antenna resonant frequency.

As it seems in Fig. 5(b), in DNG-loaded case, an additional resonance occurs while compared with ENG inclusion. In contrast, for the dipoles loaded with MNG-inclusions, changing plasma frequency causes no resonances at lower frequencies, as shown in Fig. 5(c).

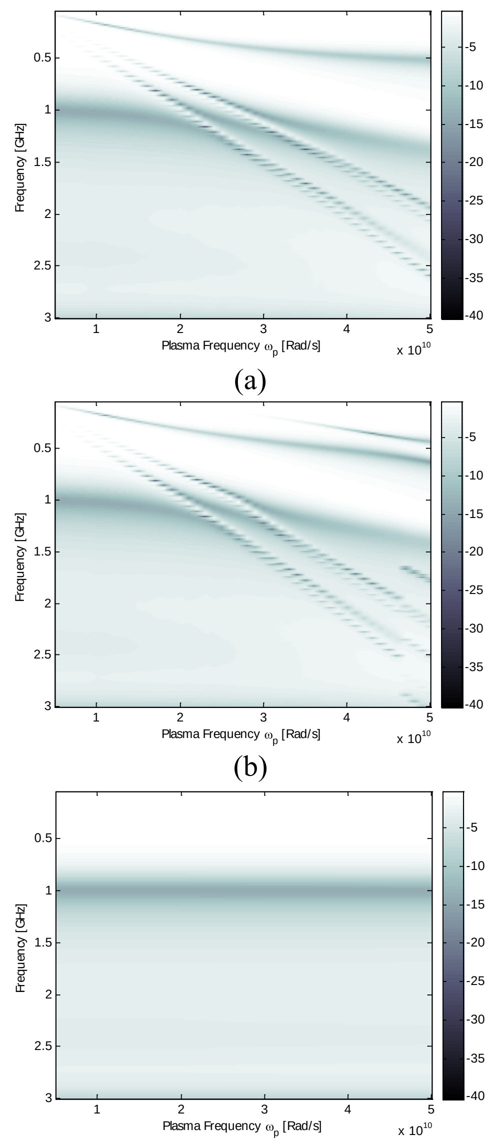

(a)

(b)

(c)

Fig. 5. CST simulation results for $|S_{11}|$ [dB] versus plasma frequency, d_{MIF}=72mm, (a) ENG-, (b) DNG-, (c) MNG-inclusions.

2.3. Power reflection coefficient, $|S_{11}|$ as a function of MTM width

The behaviors of the loaded dipole as a function of the inclusion width for d_{MIF}=45mm, have been studied. Figure 6 shows the antenna return loss for the dipoles loaded with DPS-, ENG-, DNG-, and MNG-inclusions. It can be concluded from Fig. 6 that for the dipole antenna loaded with DNG- or ENG-inclusions, an additional resonance frequency is introduced at the frequencies lower than the antenna resonant frequency. This resonance affects significantly by changing the width of MTM inclusion.

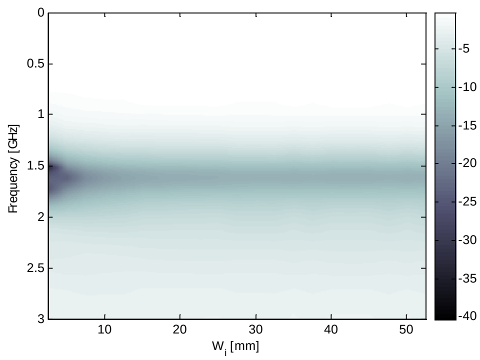

(a)

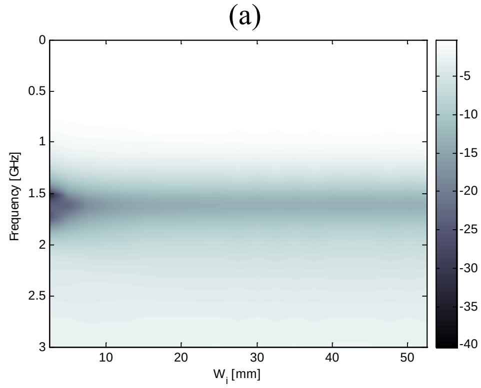

(b)

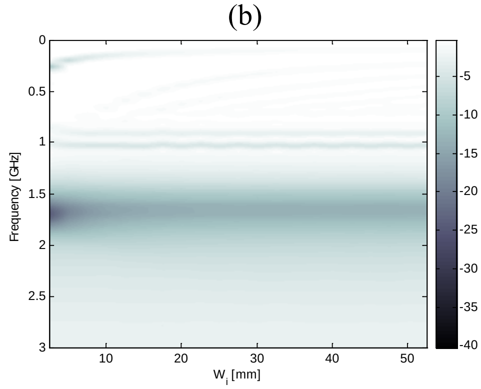

(c)

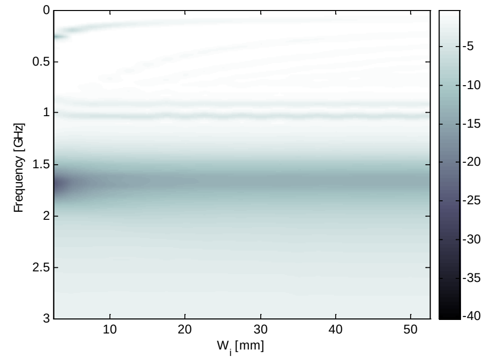

(d)

Fig. 6. CST simulation results for $|S_{11}|$ [dB], d_{MIF}=45mm, versus width of (a) DPS-, (b) MNG-, (c) DNG-, and (d) ENG-inclusions.

Decreasing the width causes more matching condition while increasing width of MTM inclusion makes antenna mismatching in this frequency. Again, in contrast, for the dipoles loaded with DPS- and MNG-inclusions, changing inclusion width causes no additional resonances at lower frequencies, as shown in Figs. 6(a) and 6(b).

III. PROPOSED METAMATERIAL CELL

In the previous section, it was revealed that the use of the ENG- and DNG-inclusions has led to a multi-resonance behavior. In this section, a new printed MTM cell is introduced to realize the ENG-inclusions. Figure 7 shows a schematic of the proposed MTM cell. The proposed MTM cell is printed on a FR4 substrate with a thickness of 0.8mm and a dielectric constant of 4.4. An important feature of the proposed MTM is that it offers more degrees of freedom than conventional MTM cells [14]. In order to retrieve the constitutive parameters of the proposed metamaterial, a unit cell positioned between two perfect electric conductors (PEC) in y direction and two perfect magnetic conductors (PMC) in x direction is simulated, and used to model an infinite periodic structure [15]. The resultant scattering parameters obtained from CST microwave studio are exerted to the Chen's algorithm [15]. Figure 8 shows the retrieved effective parameters of the proposed metamaterial cell. As can be seen, the proposed MTM cell has the permittivity that exhibits Drude behavior at frequencies lower than 1.1GHz and Lorentz behavior [14] at frequencies higher than 1.1GHz.

Thus, this MTM can be approximated via a combination of Lorentz and Drude models.

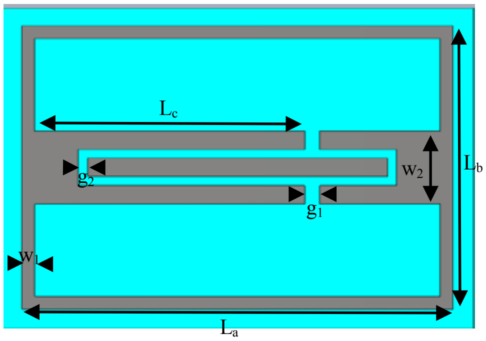

(a)

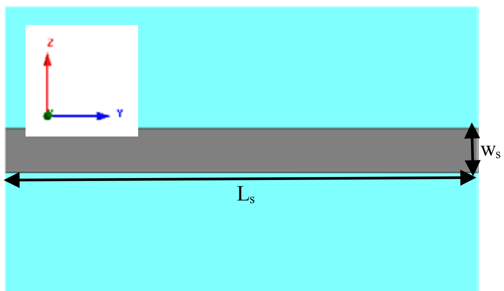

(b)

Fig. 7. Schematic of the proposed MTM unit cell and its design parameters, (a) front view, (b) back view: L_a=23.54mm, L_b=15.55mm, L_c=14.78mm, w_1=0.7mm, g_1=0.8mm, w_2=4mm, g_2= 0.5mm, w_s=2.5mm, and L_s=26.75mm.

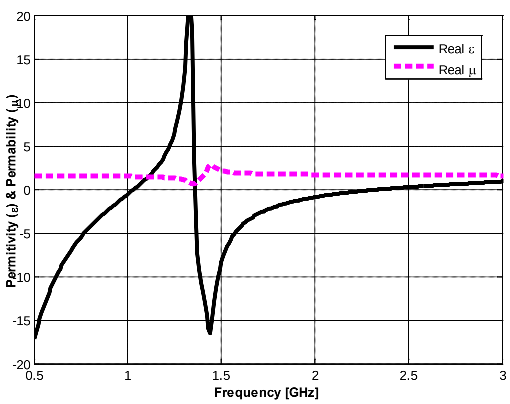

Fig. 8. Retrieved effective parameters of the proposed MTM cell.

IV. COMPACT DIPOLE ANTENNA

In order to realize the miniaturization method described in Section II, a double-sided printed dipole antenna is chosen for its simplicity in implementation and its low profile. Figure 9(a) shows the proposed miniaturized printed dipole, in which a pair of proposed MTM cells is symmetrically added to each side of the printed dipole. The proposed MTM cells and dipole are printed on a FR4 substrate with a thickness of 0.8mm and a dielectric constant of 4.4 to reduce the cost of the antenna and to make it more rigid in construction.

For the MTM cells that are far away from the dipole arms, the coupling levels of them with the dipole arms are low and thus the arrangement of the several MTM cells has no effect on the frequency behaviour of the proposed antenna. As a result, the dipole is just loaded with single cell MTM. Similar to the DNG- [3] and ENG- [17] MTMs, the proposed MTM cell can be modelled as a parallel resonant LC circuit. Thus, the proposed metamaterial cell is modeled as a resonant LC circuit parallel to the dipole, and the radiation into the free space is modelled as a resistor [18]. A prototype of the proposed miniaturized dual-band printed dipole is fabricated to confirm the simulation results. Figure 9(b) shows a photograph of the fabricated antenna.

Figure 10 shows the return loss of the proposed symmetrically loaded dipole with the gap length, g_1, of 0.8mm as well as the unloaded dipole antenna. As can be seen, the dipole antenna along with the loading elements provides good matching at both resonance frequencies. For comparison purposes, a simple dipole antenna loaded with lossy ENG inclusions, with the same retrieved effective parameters of the proposed MTM cell (Fig. 7), is also simulated. As can be seen from Fig. 10, the return loss of the dipole loaded with ENG inclusions correlates nicely to that obtained for the single cell MTM loaded dipole. The co-polarized and cross-polarized radiation patterns of the proposed loaded dipole are measured at the resonant frequencies of 940MHz and 1.7GHz. The measured and simulated radiation patterns at first and second resonant frequencies are shown in Fig. 11. As expected, the radiation patterns at both resonant frequencies are similar to that of the conventional unloaded dipole antenna.

The gain of the proposed antenna at a low resonant frequency is high compared to that of the other miniaturized MTM loaded dipoles [6-9]. The antenna gains at first and second resonant frequencies are -2.679dBi and 1dBi, respectively. The proposed antenna has a broad bandwidth of 15.96% at 940MHz (which is significantly wider than the bandwidth of other miniaturized MTM loaded dipoles [6-9], [19-24]) and 32.35% at 1.7GHz. An important advantage of the proposed antenna is that the dipole length does not need to be increased to lower the resonant frequency. Consequently, a compact antenna is obtained.

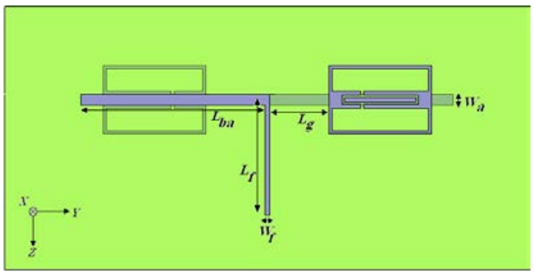

(a)

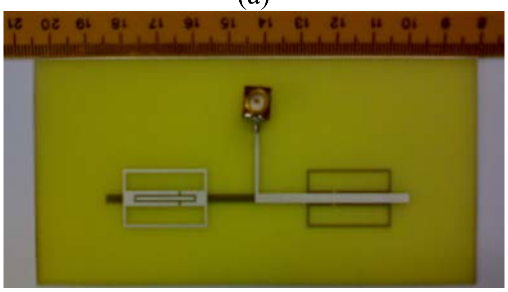

(b)

Fig. 9. (a) Printed dipole symmetrically loaded with single cell MTM: L_{ba}=42.05mm, L_f=27.5mm, L_g=12.52mm, W_a= 2.5mm, W_f=0.8mm, and (b) prototype of proposed miniaturized printed dipole antenna loaded with single cell MTM.

Finally, the effect of the MTM location is investigated to obtain some engineering guidelines for loaded dipole designs. Thus, the loading elements move along the antenna arms and the antenna return loss is plotted in Fig. 12 for each stage. The gain, bandwidth and radiation efficiency of the loaded dipoles with different MTM locations are also compared in Table II. As can be seen, the first resonant frequency remains approximately unchanged while the second one reduces as the MTM cells move away from the antenna feed point. Thus, when the MTM elements move closer to the dipole ends the separation of the two resonances decreases. In addition, when the MTM cells are placed close to the antenna feed point, the proposed antenna cannot match very well to a 50Ω transmission line. Moreover, as can be seen from Figs. 2 and 12, the single cell MTM loaded printed dipole follows closely the frequency behavior of the dipole antenna loaded with cylindrical dispersive ENG-inclusions, as d_{MIF} or L_g increases.

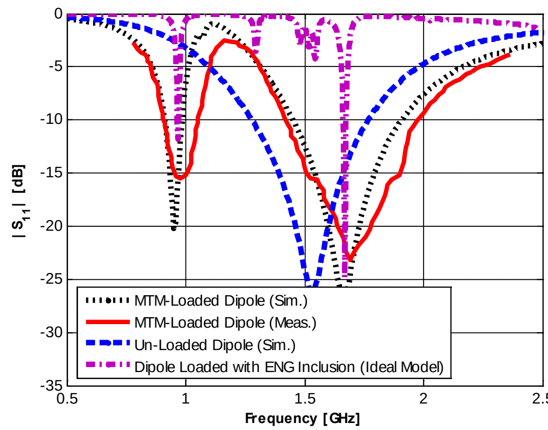

Fig. 10. Return loss of the proposed miniaturized printed dipole antenna loaded with single cell MTM. As a reference, an unloaded dipole and an ideal model of the ENG-Loaded dipole are also simulated.

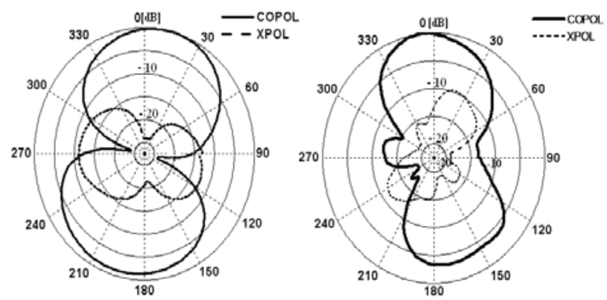

(a) (b)

Fig. 11. Measured radiation patterns of the proposed antenna, (a) 940MHz and (b) 1.7GHz.

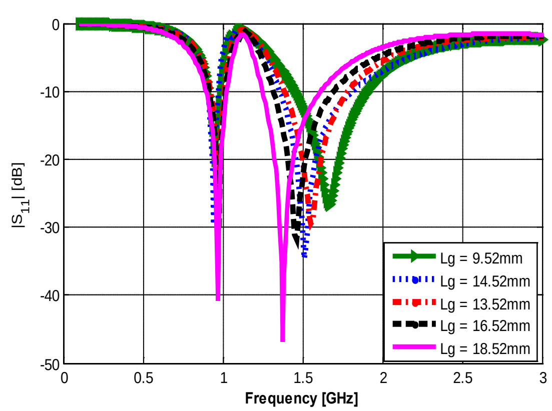

Fig. 12. The effect of the MTM location on the return loss of the printed dipole antenna.

Table 1: Gain, radiation efficiency, and bandwidth characteristics of the dipole antenna loaded with different DNG inclusions

L_g	Design I				Design II				Design III			
	f_{r1}	f_{r2}	f_{r3}	f_{r4}	f_{r1}	f_{r2}	f_{r3}	f_{r4}	f_{r1}	f_{r2}	f_{r3}	f_{r4}
$\boldsymbol{f_0}$ (GHz)	0.26	0.8	1.0	1.1	0.33	0.7	0.93	1.0	0.29	0.8	1.0	1.1
Gain (dBi)	-7.2	1.25	0.0	2.1	1.3	2.1	1.9	3.4	-3.5	2.0	0.5	2.2
$\boldsymbol{\eta}$ (%)	12.2	78	65	91	84	99	100	100	25	91	80	95
BW (%)	5.6	7.5	5.4	21.8	1.1	13.1	2.4	1.5	4.5	12.1	5	1.8

Table 2: Comparison of the gain, bandwidth, and radiation efficiency for the loaded dipole antenna with different MTM Locations

L_g	9.52mm		13.52mm		14.52mm		16.52mm		18.52mm	
	f_{r1}	f_{r2}	f_{r1}	f_{r2}	f_{r1}	f_{r2}	f_{r1}	f_{r2}	f_{r1}	f_{r2}
$\boldsymbol{f_0}$ (GHz)	0.95	1.68	0.96	1.59	0.95	1.51	0.96	1.5	0.94	1.39
Gain (dBi)	-2.38	1	-2.3	0.7	-2.5	0.55	-2.36	0.3	-2.7	0.14
$\boldsymbol{\eta}$ (%)	88	93	97	94	90	93	92	92	87	93
BW (%)	8.1	27	9.7	27	8.9	27	11.5	25	7.3	21

IV. CONCLUSION

The behavior of a dipole antenna loaded with MTM inclusions has been examined. It has been revealed that embedding DNG-/ENG-inclusions in a simple dipole antenna can provide an opportunity to design miniaturized\multi-band antenna. In order to realize this method, a single unit cell of MTM reactive loading has been utilized. Results show that placing proposed MTM cells in close proximity of a printed dipole antenna creates a double resonant antenna, the response of which is a function of MTM dimensions as well as of locations of MTM cells along the dipole arms. A prototype of the proposed miniaturized MTM-loaded printed dipole is fabricated to validate the simulation results. A good agreement between the measured and simulated results is achieved

ACKNOWLEDGMENT

The authors would like to thank Iran Telecommunication Research Centre (ITRC) for its financial supports.

REFERENCES

[1] S. D. Rogers, C. M. Butler, and A. Q. Martin "Design and Realization of GA-Optimized Wire Monopole and Matching Network With 20:1 Bandwidth," *IEEE Trans. Antennas Propag.*, vol. 51, no. 3, 493–502, 2003.

[2] A. Erentok, P. Luljak, and R. W. Ziolkowski, "Antenna Performance Near a Volumetric

Metamaterial Realization of an Artificial Magnetic Conductor," *IEEE Trans. Antennas Propag*., vol. 53, 160–172, 2005.

[3] A. Jafargholi, M. Kamyab, M. Rafaei, and M. Veysi, "A Compact Dual-Band Printed Dipole Antenna Loaded with CLL-Based Metamaterials," *International Review of Electrical Engineering*, vol. 5, no. 6, 2710-2714, 2010.

[4] Q. Liu, P. S. Hall, and A. L. Borja, "Efficiency of Electrically Small Dipole Antennas Loaded with Left-Handed Transmission Lines," *IEEE Trans. Antennas Propag*., vol. 57, no. 10, 3009–3017, 2009.

[5] A. Jafargholi, M. Kamyab, and M. Veysi, "Artificial Magnetic Conductor Loaded Monopole Antenna," *IEEE Antennas Wireless Propag. Lett.*, vol. 9, pp. 211-214, 2010.

[6] H. Iizuka, P. S. Hall, and A. L. Borja, "Dipole Antenna with Left-Handed Loading," *IEEE Antennas Wireless Propag. Lett*., vol. 5, 483–485, 2006.

[7] A. L. Borja, P. S. Hall, Q. Liu, and H. Iizuka, "Omnidirectional Left-Handed Loop Antenna," *IEEE Antennas and Wireless Propagation Lett*., vol. 6, pp. 495-498, 2007.

[8] H. Iizuka and P. S. Hall, "Left-Handed Dipole Antennas and Their Implementations," *IEEE Trans. Antennas Propag*., vol. 55, no. 5, pp. 1246–1253, 2007.

[9] M. Rafaei Booket, M. Kamyab, A. Jafargholi, and S. M. Mousavi, "Analytical Modeling of the Printed Dipole Antenna Loaded with CRLH Structures," *Progress In Electromagnetics Research B*, vol. 20, 167-186, 2010.

[10] J. Zhu, M. A. Antoniades, and G. V. Eleftheriades, "A Compact Tri-Band Monopole Antenna with Single-Cell Metamaterial Loading," *IEEE Trans. Antennas Propag*., vol. 58, no. 4, 1031–1038, 2010.

[11] H. Mosallaei and K. Sarabandi, "Design and Modeling of Patch Antenna Printed on Magneto-Dielectric Embedded-Circuit Metasubstrate," *IEEE Trans. Antennas Propag.*, vol. 55, no. 1, 1031–1038, 2007.

[12] S. A. Tretyakov, S. I. Maslovski, A. A. Sochava, and C. R. Simovski "The Influence of Complex Material Coverings on the Bandwidth of Antennas," Physics. Class-ph, 2004.

[13] C. A. Balanis, *Advanced Engineering Electromagnetics*, Wiley, 1989.

[14] N. Engheta and R. Ziolkowski, *Metamaterials: Physics and Engineering Explorations*, Wiley, 2006.

[15] M. Veysi, M. Kamyab, S. M. Mousavi, and A. Jafargholi "Wideband Miniaturized Polarization-Dependent HIS Incorporating Metamaterials," *IEEE Antennas Wireless Propag. Lett*., vol. 9, 764-766, 2010.

[16] V. Lucarini, J. J. Saarinen, K.-E. peiponen, and E. M. vartiainen, "Kramers-Kronig Relation in Optical Materials Research," *Springer Series in Optical Sciences*, 2004.

[17] Alu and N. Engheta; "Pairing an Epsilon-Negative Slab With a Mu-Negative Slab: Resonance, Tunneling and Transparency," *IEEE Trans. Antennas Propagat*., vol. 51, pp. 2558–2571, 2003.

[18] D. Sievenpiper, "Chapter 11: Review of Theory, Fabrication, and Applications of High Impedance Ground Planes," in *Metamaterials: Physics and Engineering Explorations*, edited by N. Engheta and R. Ziolkowski, Wiley, 2006.

[19] A. K. Iyer and G. V. Eleftheriades, "A Multilayer Negative-Refractive Index Transmission-Line Metamaterial Free-Space Lens at X-Band," *IEEE Trans. Antennas Propag.*, vol. 55, no. 10, pp. 2746–2753, 2007.

[20] D. L. Sounas, N. V. Kantartzis, and T. D. Tsiboukis, "Focusing Efficiency Analysis and Performance Optimization of Arbitrarily Sized DNG Metamaterial Slabs with Losses," *IEEE Trans. Microw. Theory Tech*., vol. 54, no. 12, 4111–4121, 2006.

[21] A. Alù, F. Bilotti, N. Engheta, and L. Vegni, "Subwavelength, Compact, Resonant Patch Antennas Loaded with Metamaterials," *IEEE Trans. Antennas Propag*., vol. 55, no. 1, pp. 13-25, 2007.

[22] N. V. Kantartzis, D. L. Sounas, and T. D. Tsiboukis, "Stencil-Optimized Time-Domain Algorithms for Compact Circular Patch Antennas with Anisotropic Metamaterial Substrates," *IEEE Trans Magn*., vol. 45, no. 3, 1368-1371, 2009.

[23] M. Tang, S. Xiao, D. Wang, J. Xiong, K. Chen, and B. Wang, "Negative Index of Reflection in Planar Metamaterial Composed of Single Split-Ring Resonators," *Applied Computational Electromagnetic Society (ACES) Journal*, vol. 26, no. 3, 250 – 258, 2011.

[24] M. Naghshvarian-Jahromi and N. Komjani-Barchloui, "Analysis of the Behavior of Sierpinski Carpet Monopole Antenna," *Applied Computational Electromagnetic Society (ACES) Journal*, vol. 24, no. 1, pp. 32 – 36, 2009.

Amir Jafargholi received the Ph.D. degree in Electrical Engineering from K.N. Toosi University of Technology, Tehran, Iran, in 2011. He is the coauthor of about 50 scientific contributions published in international books, journals and peer-reviewed conference proceedings. His research interest includes the applications of metamaterials in the analysis and synthesis of antennas.

Dr. Jafargholi was a recipient of a Student's Best Thesis National Festival award for his B.S. thesis, on May 2006. He was a recipient of the 22th Khawarizmi International and 13th Khawarizmi Youth Award on Jan. 2009 and Oct. 2011, respectively. He was also the recipient of Research Grant Awarded in Metamaterial 2010.

Manouchehr Kamyab received the B.S. and M.S. from the University of Tehran, Tehran, Iran, and the Ph.D. degree from Michigan State University, in 1982, in Electrical Engineering. His research interest includes the metamaterials and their applications in antenna engineering, electrically small antennas, microwave and millimeter-wave circuits, and mobile communication systems. He is currently an associate professor in the Department of Electrical Engineering, K.N. Toosi University of Technology, Tehran, Iran.

Dr. Kamyab is leading a group of graduate students in the areas of negative-refraction metamaterials and their microwave applications, integrated antennas and components for broad-band wireless telecommunications, novel antenna beam-steering techniques, millimeter and submillimeter-wave circuits, as well as scattering and inverse scattering problems.

A Simple Synthesis of a High Gain Planar Array Antenna for Volume Scanning Radars

F. Tokan[1], F. Gunes[1], B. Turetken[2], and K. Surmeli[2]

[1] Department of Electronics and Communication Engineering Faculty of Electrics and Electronics
Yıldız Technical University, Yıldız 34349, Istanbul, Turkey
ftokan@yildiz.edu.tr, gunes@yildiz.edu.tr

[2] TÜBİTAK, UEKAE, 41470, Istanbul, Turkey
turetken@uekae.tubitak.gov.tr, koraysurmeli@uekae.tubitak.gov.tr

Abstract **─** This paper describes a simple method of designing a rectangular planar array antenna with a flat top characteristic within the given $0^o \le \phi \le \phi_{\max}$ region in the $\theta = 90^o$ principal plane to be used in the volume scanning radars. In the method, the main beam of each ingredient linear array antenna is collimated to a predetermined direction with a permissible beamwidth within the total coverage region so that the superposition of the far field ingredient phasors can result in the required overall pattern with the flat top characteristic in the region of $0^o \le \phi \le \phi_{\max}$ the principle plane. The main beamwidth requirements of the sub-arrays are met by the excitation amplitudes determined by Dolph-Chebyshev analytical method. Furthermore, the overall main beam characteristic is improved by optimizing the excitation amplitudes using the genetic algorithm. The far field patterns resulted from the half-wave dipole and patch arrays are verified by using the full-wave simulation software, computer simulation technology (CST).

Index Terms **─** Flat top pattern, linear sub-array, optimization, rectangular planar array.

I. INTRODUCTION

The goal of this work is to describe a simple method of synthesizing a rectangular planar array antenna which has a flat top characteristic within the given $0^o \le \phi \le \phi_{\max}$ region in the $\theta = 90^o$ principal plane to be used in volume scanning radars. The volume scanning radar will automatically scan various elevation angels while spinning around 360° of azimuth, rather than scanning along varying azimuth angles then stopping to scan vertically. Thus, it shortens the overall scan time. Rapid air targets which can not be determined by electronically scan but when volume search is used this targets will always be inside the antenna's beam thus targets will be detected. Thus, this radar can be used for long range and rapid surveillance.

In case that the radiation pattern distribution is given in the visible region, in literature, the analytical methods such as Fourier transformation [1], Woodward-Lawson [2-3] or Dolph-Chebyshev [4] are extensively employed in the synthesis process. In our work, the overall far field pattern is built up with the individual participation of each ingredient linear array antenna. The requirements of the individual synthesis of the ingredient linear array is to collimate its main beam to the predetermined direction with a permissible beamwidth within the coverage region so that superposition of the far field ingredients can result in the overall pattern shaped with the flat top characteristic within the $0^o \le \phi \le \phi_{\max}$ region in the principal plane. Main beamwidth requirements of the sub-arrays are met by the excitation amplitudes which are determined using the Dolph-Chebyshev analytical method which is a well-known robust method for a narrow main-beam and low sidelobe level (SLL) array antenna synthesis. Thus, N linear array antennas are built

Submitted On: Jul. 5, 2011
Accepted On: Jan. 22, 2012

1054-4887

up as collimated to the pre-determined directions with the low SLL radiation patterns such that when their far field radiation phasors are super-positioned, a rectangular planar array antenna is resulted having a flat top main beam characteristic covered the specified region. The overall main beam characteristics can be improved by reducing the ripple factor in the flat-top region using an optimization process applied to the excitation coefficients. An ideal radiation pattern has zero ripples which are important drawbacks for target strength measurements and ripple in the antenna patterns presents a large uncertainty in the radio coverage measurements. In fact, we employed the genetic algorithm for this purpose. Furthermore, we applied this method to synthesis of the half-wave dipole and microstrip patch planar array antennas and verified with the full-wave commercial simulator of CST [5] which is based on the FDTD method.

Firstly, array factor of a rectangular planar array antenna in the *x*–*y* plane is formulated as the superposition of the linear arrays along *x*–axis, each of which is symmetrically positioned with respect to the *y*–axis, and collimated in different directions. Then the genetic optimization with its fitness function is given in the third section. Fourth section is devoted to the applications. Finally paper ends with the conclusions.

II. FORMULATION

As well-known, a 3-dimensioned array antenna pattern can be factorized as the array factor and the radiation pattern of a single element, in the case that the array elements are identical and mutual coupling effects between these array elements can be neglected. In any of the $\phi=$ constant planes, the element pattern has a constant value [6], thus the far field radiation pattern of a linear array can be defined as equal to array factor $AF(\theta,\phi)$ as follows [7]:

$$FF(\theta,\phi)=AF(\theta,\phi)$$
$$=\sum_{m=1}^{N_y}\sum_{n=1}^{N_x}A_{mn}e^{-j\beta_{mn}}e^{j\xi_{mn}}\;, \quad (1)$$

$$\xi_{mn}=k\hat{r}.\vec{r}'_{mn}$$
$$=k[x'_{mn}\sin\theta\cos\phi+y'_{mn}\sin\theta\sin\phi]\,, \quad (1.1)$$

$$\beta_{mn}=k[x'_{mn}\sin\theta_o\cos\phi_o+y'_{mn}\sin\theta_o\sin\phi_o]\,, \quad (1.2)$$

where, A_{mn}, β_{mn} and $\vec{r}\,'$ are the excitation amplitude amplitude, phase and the position vector of the *mn*th element, respectively. k is the wave number of the free space and N_x ,N_y are the number of columns and rows in the rectangular planar array, respectively. In (1.1), $\hat{r}$ is the unit vector directed to the observation point from the origin and double summation is especially useful for row and column including geometries such as rectangular plane. If the elements are placed along *x*-axis symmetrically with respect to *y*-axis, x'_{mn} can be expressed as follows:

$$x'_{mn}=\frac{2n-1}{2}d_x\,. \quad (2)$$

Here, d_x is the distance of the element in *x*-axis from the origin. In order to collimate the main beam into $\theta_o=90^o$ the plane, phase vector of the *mn*th element can be defined as follows:

$$\beta_{mn}=k[x'_{mn}\cos\phi_{mo}]\;. \quad (3)$$

Substituting (2) and (3) into (1), we have finally,

$$AF(\theta)=2\sum_{m=1}^{N_y}.$$
$$(\sum_{n=1}^{N_x}A_{mn}\cos[(\frac{2n-1}{2})kd_x(\cos\phi-\cos\phi_{mo})])\;. \quad (4)$$

Thus, according to (4), the synthesis process for the whole planar array can be reduced to synthesize N_y linear arrays directed to ($\phi_{mo},m=1,.........N_y$) so as when their far field phasors are super-positioned, the overall flat top main beam characteristic covered the specified region is resulted.

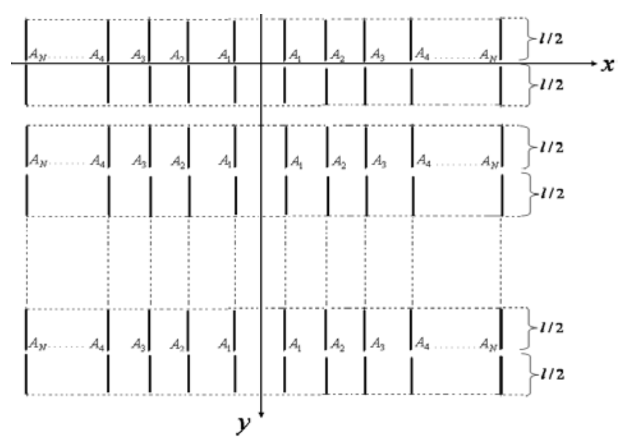

Fig. 1. A rectangular planar half-wave dipole antenna array.

For this purpose, the phase of each element is found from (2) using the pre-specified main beam directions $(\phi_{mo}, m=1,.........N_y)$ and at the same time beam width requirements of a sub-array are also met by determining the $\vec{A}$ amplitude vector dimensioned by (1xN_x/2) using any well-known analytical method in an optimum sidelobe level. In this work, Dolph-Chebyshev method is chosen to synthesize the $\vec{A}$ amplitude vector and (-40 dB) level is determined as the optimum sidelobe level to meet main beam width requirements for the sub-arrays in the worked examples. Furthermore, the main beam characteristic of the whole array antenna is developed by optimizing the Dolph-Chebyshev excitation amplitudes of the whole array. In this work, the genetic algorithm is employed as the optimization tool. Furthermore, the far field patterns resulted from the synthesized half-wave dipole and microstrip patch array antennas are verified using the full-wave simulation software, CST.

III. GENETIC OPTIMIZATION

In fact, the excitation amplitudes are obtained as the result of the Dolph-Chebyshev synthesis process; furthermore the genetic algorithm is used to improve the overall far field characteristics. The reader is referred to [8-10] and the references mentioned therein for a detailed discussion of the basic concepts of the genetic algorithm. Thus, in the optimization process, the Dolph-Chebyshev excitation amplitudes are chosen as the decision variables and the following fitness function is employed:

$$Fitness(\vec{A}) = 20\log\left\{\frac{1}{\Delta\phi}\int_{\phi_l}^{\phi_u}\left|AF(\theta,\vec{A})\right|d\phi\right\} - s*SLL(dB), \quad (5.1)$$

$$SLL = \begin{cases} MSLL, & if \ \max(SLL) \geq -25dB \\ 0, & otherwise \end{cases}, \quad (5.2)$$

where max(SLL) can be expressed in terms of the normalized array factor as follows:

$$\max(SLL) = \max[20\log(\left|AF(\theta,\vec{A})\right|_{\phi=-90^o}^{\phi=\phi_l-\delta\phi_l})] \quad or \quad \max[20\log(\left|AF(\theta,\vec{A})\right|_{\phi=\phi_u+\delta\phi_u}^{\phi=90^o})] \quad (5.3)$$

where $\left|AF(\theta,\vec{A})\right|$ is the normalized form of the array factor given by (4) where $\vec{A}$ is the excitation amplitude vector of a single linear antenna since all the linear array units within the planar array antenna have the same $\vec{A}$ vector. Here $\vec{A}$ has the dimension of 1x N_x/2, N_X is the element number of the single linear array. s is a constant and $s \gg 1$ in order to ensure that the second term of (5.1) will be dominant if *MSLL* is greater than -25 dB. ϕ_u, ϕ_l and $\delta\phi_l$, $\delta\phi_u$ are upper and lower boundaries of the main beam region, and upper and lower tolerances for the boundaries, respectively, and $\Delta\phi = \phi_u - \phi_l$. In the fitness function given by (5.1), the first term is used to maximize the average normalized array factor as dB within the given $\phi_l \leq \phi \leq \phi_u$ region while the second term avoids the maximum sidelobe level in (5.3) to exceed the given maximum level MSLL which is taken (-25 dB) as the suitable value in the following worked examples. For both cases defined by (5.2), the first term acts dominant role in the optimization process.

IV. APPLICATION EXAMPLES

In this section, we have synthesized the 4x10 and 6x20 rectangular planar arrays in the *x*-*y* plane using half-wave dipole and microstrip square patches as the elementary antenna as shown in Figs.1 and 5 to achieve a flat top within the region of $0^o \leq \phi \leq 60^o$ in the $\theta = 90^o$ principal plane to be used in the volume scanning radars. For synthesis of both antennas, Dolph-Chebyshev method is utilized to determine the excitation amplitude vector $\vec{A}$ and the sidelobe level is adjusted so that each ingredient linear array antenna can be collimated to the pre-determined direction with the permissible beamwidth.

In the first worked example, 4 sub-arrays located along the *x*-axis, each including 10 half-wave dipoles which are symmetrically positioned with respect to the *y*-axis with the half-wavelength inter-spacings is considered. Main beams of the sub-arrays are collimated to $7.5^o, 22.5^o, 37.5^o$ and 47^o respectively to form a flat top within the region of $0^o \leq \phi \leq 60^o$ in the principle plane. In this worked example, the main beamwidths of the first three sub-arrays are taken as 15^o, while the last sub-array is directed 47° instead of 52.5° due to the broadening effect. Besides, for the first example the upper and lower tolerances are 3° and 5°,respectively. In the Dolph-Chebyshev synthesis, after a number of trials, (-40) dB is determined to be optimum for the maximum sidelobe level of the ingredient linear array antennas to meet all the direction and beamwidth requirements mentioned above.

After having the Dolph-Chebyshev excitation amplitudes, a genetic optimization process is applied to improve the overall flat top characteristic. A genetic algorithm is adopted with the following parameter suite: population size: number of the excitation amplitudes; crossover probability: 0.75; mutation probability: 0.01. The optimization process takes only a few seconds for both worked examples.

The Dolph-Chebyshev and optimized excitation amplitudes are given in Table 1. Besides, the synthesized far field patterns of the sub-arrays by the Dolph-Chebyshev method are given in Fig. 2. The excitation phases of each element antenna of the symmetrical rectangular array are also given in Table 2.

Table 1: Dolph-Chebyshev excitation amplitudes and the optimized values of the 4x10 rectangular planar array antenna

Each Sub-Array	$A_n(A)$	1.000	0.878	0.669	0.430	0.257
	$A_n(A)$ (optimized)	1.000	0.878	0.818	0.461	0.542

Table 2: Excitation phases of the sub-arrays of the 4x10 rectangular planar array antenna

Excitation Phases of Each Sub-Array			
$\theta_{\max_1} = 7^o$	$\theta_{\max_2} = 22^o$	$\theta_{\max_3} = 37^o$	$\theta_{\max_4} = 47^o$
-10.96	-33.71	-54.16	-65.82
-32.90	-101.14	-162.49	-197.46
-54.84	-168.57	-270.81	-329.1
-76.77	-236	-19.14	-100.75
-98.71	-303.43	-127.47	-232.39

In order to investigate the effects of the number of antennas in a sub-array and the number of antennas in the planar array we have also designed a 120 element rectangular array which is formed by 6 sub-arrays located in *x*-axis each including 20 half-wave dipoles.

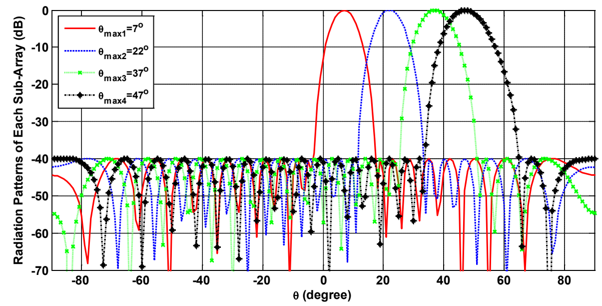

Fig. 2. The far-field patterns of the linear sub-arrays resulted from the Dolph-Chebyshev excitation amplitudes and phases given in Table 1and 2, respectively.

The main beams of sub-arrays are steered to $5^o, 15^o, 25^o, 35^o, 45^o$ and 55^o respectively, allowing 10° beamwidth for each sub-array. Moreover, in this case the upper and lower tolerances are 5° and 20°, respectively. The *MSLL* is again adjusted as -40 dB in order to ensure the main beamwidth requirements. The Dolph-Chebyshev excitation amplitudes and their optimized values are given in Table 3. Excitations phase of each element is calculated using (2). Thus, the resulted far field patterns of the sub-arrays are given with their main beam directions in Fig. 3.

Table 3: Dolph-Chebyshev excitation amplitudes and the optimized values of the 6x20 rectangular planar antenna

Each Sub-Array	
$A_n(A)$	$A_n(A)$ (optimized)
1.000	1.000
0.958	0.868
0.880	1.289
0.772	0.715
0.646	0.114
0.512	0.388
0.381	0.227
0.264	0.444
0.166	0.108
0.118	0.175

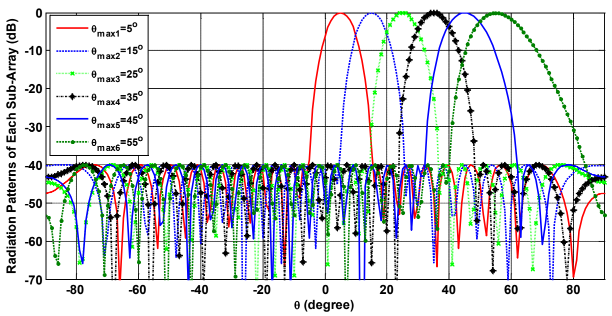

Fig. 3. The far field patterns of each sub-array of the 6x20 rectangular planar antenna using the Dolph-Chebyshev amplitudes given in Table 3.

In Fig. 4, the Dolph-Chebyshev and the optimized far field patterns of the 4x10 planar array are given together to see the effect of the optimization process on the main beam characteristic. It is clear from the Fig. 4 that a lower ripple level, which is crucial in target strength measurements, is achieved by a compromise between the ripple level and the *MSLL*. Furthermore, the far field patterns resulted from the CST full-wave simulations of both the 4x10 and 6x20 planar antennas with their optimized excitation amplitudes and phases are also given in the same figure. From these graphs, one can derive the following results: (i) the proposed synthesis method is a simple, easy and successful method since it is fast and easy to implement and results agree with the full-wave simulations; (ii) optimization process reduces the ripple factor of the top characteristic for the rectangular array of a fixed elements; (iii) increase in the number of elements results in reduce the ripple factor, thus one can obtain flatter main beam characteristic with sharper falling rate; and (iv) full-wave simulations indicate that the upper limit of the flat top region is expected to be smaller in comparison to the value computed while synthesizing the array.

Furthermore, synthesized excitation amplitudes and phases of the 4x10 and 6x20 planar antenna are applied to the planar array with the rectangular patch type element (Fig. 5). In these antennas, a substrate (RT/duroid 5880) with dielectric constant of 2.2, h=1.58 mm is used and W, L dimensions of the patch antennas are 10.136 mm and 8.18, respectively, so as to resonate at 11.7 GHz. The CST simulation software is utilized to obtain results of the total radiation patterns of the sub-arrays having 40 and 120 microstrip elements as given in Fig. 6.

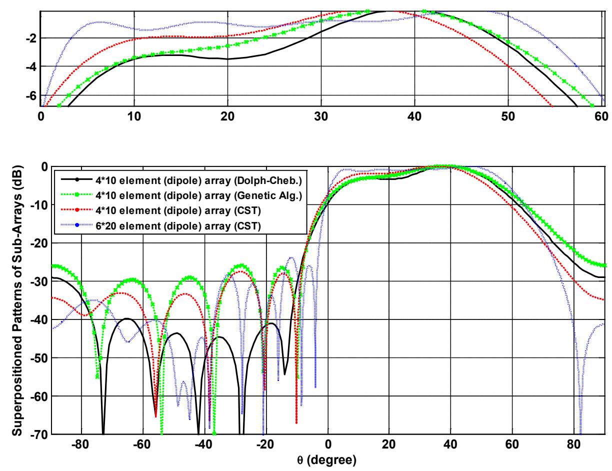

Fig. 4. The Dolph-Chebyshev and optimized far field patterns of the 4x10 element planar array, and the CST simulations of the 4x10 element and 6x20 element planar arrays.

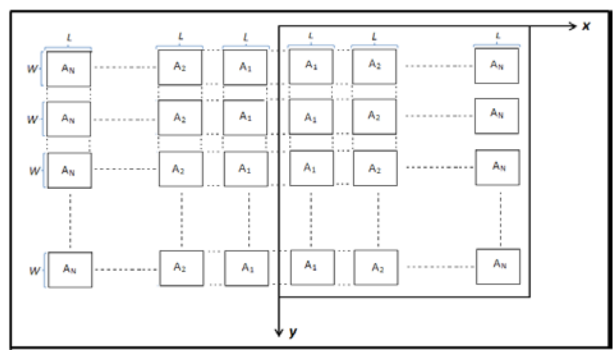

Fig. 5. A rectangular planar patch antenna array.

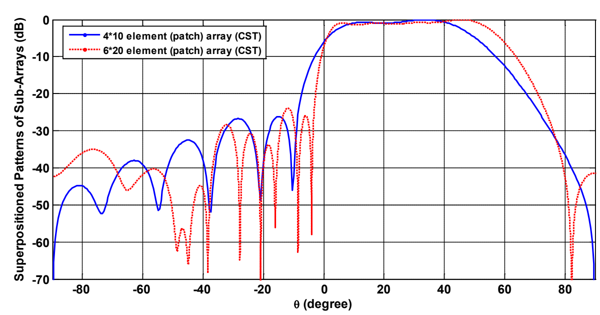

Fig. 6. The simulated radiation patterns of the 4x10 element and 6x20 element planar arrays including microstrip patch antennas.

The desired 60^o main width radiation pattern in $\theta = 90^o$ principal plane is also achieved using the microstrip antennas as the elementary antenna as seen from Fig. 6. It is illustrated that the *MSLL* of the total radiation pattern is restricted with -25 dB. It is obvious that the coverage of 6x20 element rectangular microstrip array in the 60^o width region is better than the coverage of 4x10 element array pattern.

V. CONCLUSION

In this work, a simple method is presented to synthesize a rectangular planar array antenna with a flat top characteristic within the given $0^o \le \phi \le \phi_{\max}$ region in the $\theta = 90^o$ principal plane to be used in the volume scanning radars. In the synthesis process, linear sub-arrays are taken as the units so that each of which main beam is collimated to the pre-determined direction with a permissible beam width so as to cover the overall main beam flat characteristics.

The synthesis process can be shortened with a suitable geometry. In our worked examples, the linear sub-arrays are placed along the *x*-axis symmetrically with respect to the y-axis. Thus the number of the unknowns is reduced half of the original number. All the elementary antennas in the array are excited with Dolph-Chebyshev amplitudes to provide the required beamwidth for the linear sub-array units. Thus, the resulted far field patterns of each sub-array are collimated to the determined directions, rather than collimating the array elements to the different directions [11]. Thus, the desired overall far field pattern characteristic is synthesized as superposition of contribution of each linear sub-array.

The effects of the number of sub-arrays and the number of antennas in each sub-array on the coverage region are investigated by synthesizing the planar array with different number of antennas. Moreover, the excitation amplitudes are optimized by genetic algorithm to obtain more compatible pattern with the desired pattern. Half-wave dipoles and microstrip patches are utilized as the elementary antenna and the simulation results are obtained using CST. The simulation results verify that the proposed simple method can be used successfully in volume scanning arrays.

REFERENCES

[1] H. G. Booker and P. C. Clemmow, "The Concept of an Angular Spectrum of Plane Waves, and its Relation to that of Polar Diagram and Aperture Distribution," *Proc. IEE (London)*, *Paper Radio Section*, vol. 97, pp. 11–17, 1952.

[2] P. M. Woodward, "A Method for Calculating the Field over a Plane Aperture Required to Produce a Given Polar Diagram," *J. IEE*, vol. 93, pp. 1554–1558, 1946.

[3] P. M. Woodward and J. D. Lawson, "The Theoretical Precision with which an Arbitrary Radiation–Pattern may be Obtained from a Source of Finite Size," *J. IEE*, vol. 95, pp. 363–370, 1948.

[4] C. L. Dolph, "A Current Distribution for Broadside Arrays which Optimizes the Relationship between Beamwidth and Sidelobe Level," *Proc. IRE,* vol. 34, pp. 335–345, 1946.

[5] CST Microwave Studio, User Manual Version 5.0, CST GmbH, Darmstadt, Germany.

[6] F. Tokan and F. Güneş, "Interference Suppression by Optimizing the Positions of Selected Elements using Generalised Pattern Search Algorithm," *IET Microwaves, Antennas & Propagation*, vol. 5, pp. 127–135, 2011.

[7] W. L. Stutzman and G. A. Thiele, Antenna Theory and Design, John Wiley & Sons, 1998, New York.

[8] D. E. Goldberg, *Genetic Algorithms in Search Optimization and Machine Learning*, Addison Wesley, 1989, New York.

[9] R. L. Haupt, "Genetic Algorithm Applications for Phased Arrays," *Applied Computational Electromagnetics Society (ACES) Journal*, vol. 21, no. 3, pp. 325–336, 2006.

[10] R. L. Haupt and S. E. Haupt, "Optimum Population Size and Mutation Rate for a Simple Real Genetic Algorithm that Optimizes Array Factors," *Applied Computational Electromagnetics Society (ACES) Journal*, vol. 15, no. 2, pp. 94–102, 2000.

[11] A. Akdagli and K. Guney, "Clonal Selection Algorithm for Design of Reconfigurable Antenna Array with Discrete Phase Shifters," *Journal of Electromagnetic Waves and Appl.,* vol. 21, pp. 215-227, 2007.

Fikret Tokan received the M.S. degree in Electronics and Communications Engineering from the Yıldız Technical University in 2005 and PhD degree from the Yıldız Technical University, Istanbul, in Communications Engineering in 2010.

He has been currently working as a researcher in Yıldız Technical University. His current research interests are UWB antenna design, dielectric lens antennas, electromagnetic waves, propagation, antenna arrays, scattering, and numerical methods.

Filiz Gunes received her M.Sc. degree in Electronic and Communication Engineering from the Istanbul Technical University. She attained her Ph.D. degree in Communication Engineering from the Bradford University in 1979.

She is currently a full professor in Yıldız Technical University. Her current research interests are in the areas of multivariable network theory, device modeling, computer-aided microwave circuit design, monolithic microwave integrated circuits, and antenna arrays.

Bahattin Turetken has received M.Sc. and Ph.D. degrees from Istanbul Technical University, Istanbul, Turkey in 1998 and 2002, respectively. He received associate professor title in 2008. He has been worked as chief researcher at TUBITAK-UEKAE (National Research Institute of Electronics and Cryptology) EMC & TEMPEST Test Center. Now, he manages Electromagnetic and Research Group (EMARG) and the project of Antenna Test and Research Center. He was awarded "Young Scientist Award" by URSI in 1999 and "Young Scientist Paper" by MMET in 2000. His research topics are radar, antenna design and testing, computational electromagnetic, diffraction & scattering EM Problems, civilian and military EMC/EMI problems.

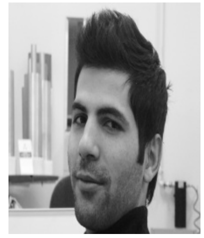

Koray Surmeli has received B.S. degree in electronics and Communication Engineering from Yildiz Technical University, Istanbul, Turkey in 2009 and. He has worked as researcher at TUBITAK-UEKAE (National Research Institute of Electronics and Cryptology) Electromagnetic and Antenna Research Group. His research topics are radar, antenna design and testing, computational electromagnetic, diffraction & scattering EM problems, civilian and military EMC/EMI problems.

Scattering by a 2D Crack: The Meshfree Collocation Approach

B. Honarbakhsh[1] and A. Tavakoli[1, 2]

[1]Department of Electrical Engineering

[2]Institute of Communications Technology and Applied Electromagnetics
Amirkabir University of Technology (Tehran Polytechnic), Tehran, Iran
b_honarbakhsh@aut.ac.ir, tavakoli@aut.ac.ir

Abstract **─** In this paper, the meshfree collocation method is applied to the problem of EM scattering by a 2D crack in a PEC plane. The hybrid PDE-IE formulation is the mathematical statement of the problem. Consequently, the geometry and the filling material of the cavity is arbitrary. Validations are based on convergence analysis, modal solution and measurement results. Furthermore, elliminating numerical integrations has lead to a fast, accurate, and general meshfree solution.

Index Terms **─** Collocation, crack, FFT, mesh free, scattering.

I. INTRODUCTION

Electromagnetic (EM) scattering by a two-dimensional (2D) crack in a perfect electric conductor (PEC) plane is a well-known problem in computational electromagnetics (CEM). The problem is of high value in the fields of radar cross section (RCS) and non-destructive testing (NDT). This problem has two degrees of freedom; the shape of the gap and the gap filled material. When the shape and the gap material distribution are such that the computation of the modal Green's function of the gap is possible, the modal solution is preferable which leads to an integral equation (IE) and can be efficiently solved by the method of moments (MoM) [1]. For an arbitrary shaped but homogeneously filled gap, coupled system of IEs can formulate the problem and again, MoM can be used for numerical solution [2]. The most general case, i.e., an arbitrary shaped gap with arbitrary material distribution, can be well formulated by hybridizing a partial differential equation (PDE) governing the internal gap field (the interior problem) and the boundary integral (BI) governing the field over the PEC plane (the exterior problem), which has been handled by the hybrid FEM-BI method [3]. The problem is also studied by other approaches [4-6].

It is already reported that meshfree methods (MFMs) are more accurate than the FEM [7]. Furthermore, meshfree methods can solve the same problem by considerably fewer unknowns, leading to smaller size coefficient matrices and less memory usage. This advantage is due to the superb fitting capability of meshfree shape functions. Nevertheless, these methods are in general slower but not necessarily, compared to their mesh/grid based counterparts.

Being a weighted residual method, the kind of weighting function plays a key role in the computational cost of a meshfree method. Using the Dirac delta function as weighting leads to the meshfree collocation method which is the most computational efficient type. In comparison to plentiful research in the CEM community by numerical approaches such as FDTD, FEM and MoM, limited studies by meshless approaches are available in the literature such as [8-24].

In the present work, the aforementioned hybrid PDE-IE formulation is solved by the meshfree collocation method [25]. The IE part of the problem can potentially impair the speed of the solution by imposing numerical integration. Here, some suggestions are made to completely by-pass the integrations, leading to a general, accurate and fast meshfree solution for the problem.

Submitted On: Dec. 23, 2011
Accepted On: Feb. 9, 2012

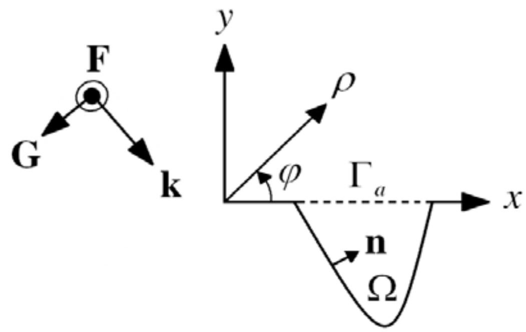

Fig. 1. Geometry description of the problem and definitions. Ω: crack domain, Γ_a: crack opening boundary, **F**/**G**: incident field, **k**: wave vector, **n**: normal vector to the crack wall.

II. MATHEMATICAL STATEMENTE OF THE PROBLEM

Geometry of the problem is depicted in Fig. 1. Based on the polarization of the incident wave, **F** and **G** are either of electric field vector **E** or magnetic field vector **H**. The wave number and intrinsic impedance of the free space are k_0 and Z_0, respectively. In addition, relative electric permittivity and magnetic permeability of the filling material are ε_r and μ_r, which are in general space dependent. Following [3], the mathematical statements of the problem for different incident polarizations are:

A. TE incidence

In this case, $\mathbf{F} = \mathbf{E} = \hat{\mathbf{z}}E,\ \mathbf{G} = \mathbf{H}$, and:

$$\begin{cases} \xi_{TE}\left(E\right) = 0,\ \rho \in \Omega \\ \mu_r^{-1} E_{,y}\Big|_{y=0^-} + \gamma_{TE}\left(E\big|_{y=0^-}\right) = q_{TE},\ \rho \in \Gamma_a\,. \\ E = 0,\ \rho \in \partial\Omega - \Gamma_a \end{cases} \tag{1}$$

where

$$\begin{cases} \xi_{TE}\left(\cdot\right) = \left(\mu_r^{-1}\left(\cdot\right)_{,x}\right)_{,x} + \left(\mu_r^{-1}\left(\cdot\right)_{,y}\right)_{,y} + k_0^2 \varepsilon_r\left(\cdot\right) \\ \gamma_{TE}\left(\cdot\right) = \left(j/2\right)\left(k_0^2 +_{,xx}\right)\int\limits_{\Gamma_a}\left(\cdot\right) H_0^{(2)}\left(k_0\left|x - x'\right|\right)dx'\,. \\ q_{TE}\left(x\right) = -j2k_0 Z_0 H_x^{inc}\left(x\right) \end{cases} \tag{2}$$

B. TM incidence

In this case, $\mathbf{F} = \mathbf{H} = \hat{\mathbf{z}}H,\ \mathbf{G} = \mathbf{E}$, and:

$$\begin{cases} \xi_{TM}\left(H\right) = 0,\ \rho \in \Omega \\ H\Big|_{y=0^-} + \gamma_{TM}\left(H\right) = q_{TM},\ \rho \in \Gamma_a\,. \\ H_{,n} = 0,\ \rho \in \partial\Omega - \Gamma_a \end{cases} \tag{3}$$

where:

$$\begin{cases} \xi_{TM}\left(\cdot\right) = \left(\varepsilon_r^{-1}\left(\cdot\right)_{,x}\right)_x + \left(\varepsilon_r^{-1}\left(\cdot\right)_{,y}\right)_y + k_0^2 \mu_r\left(\cdot\right) \\ \gamma_{TM}\left(\cdot\right) = \left(j2\right)^{-1}\int\limits_{\Gamma_a}\left(\cdot\right)_{,y'}\Big|_{y'=0^-} H_0^{(2)}\left(k_0\left|x - x'\right|\right)dx'\,. \\ q_{TM}\left(x\right) = 2H_z^{inc}\left(x\right) \end{cases} \tag{4}$$

III. MESHFREE DISCRETIZATION

From a mathematical point of view, (1) and (4) are non-local boundary value problems and as stated before, can be decomposed into two parts: interior and exterior. The operator governing the interior problem is purely differential. Alternatively, the exterior operator is integro-differential. In view of intrinsic complexity of meshfree shape functions, improper selection leads to computational inefficiency. Radial interpolants and their partial derivatives are fast to generate with high order of continuity and excellent fitting ability [7, 25]. However, they work well when they are spread over the entire problem domain [26]. On the contrary, Shepard approximants while not as powerful, are still fast and localized on a small portion of the problem [27]. Therefore, we suggest expanding the field variable of the differential and integral parts of the problem over radial bases functions (RBFs) and Shepard functions, respectively.

Here, meshfree discretization of TE polarization is presented. The TM case can be carried out in a similar manner. Let the problem domain Ω and the whole boundary ∂Ω be described by N nodes with the first M nodes placed on Γ_a and the next (N – P) nodes on the crack wall. Assume $\left\{\varphi_i^{(2D)}\right\}_{i=1}^{N}$, $\left\{\varphi_i^{(1D)}\right\}_{i=1}^{M}$ and $\left\{\psi_i^{(1D)}\right\}_{i=1}^{M}$ be sets of shape functions for corresponding nodes where superscripts represent the dimension of each set. In addition, mathematical functions u and v are defined for simplifying meshless discretization as:

$$\begin{cases} u(x) = (j/2)\int\limits_{\Gamma_a} v(x') H_0^{(2)}\left(k_0 |x - x'|\right) dx' \\ v(x) = E(x, 0) \end{cases}. \quad (5)$$

Thus, $\gamma_{TE}\left(E|_{y=0^-}\right) = (j/2)\left(k_0^2 +_{,xx}\right)u(x)$. Following the aforementioned suggestion leads to expanding E and u over interpolants and v over approximants, e.g.:

$$\begin{cases} E^h(\rho) = \mathbf{\Phi}^{(2D)^T}(\rho)\cdot \hat{\mathbf{E}} = \sum_{i=1}^{N} \varphi_i^{(2D)}(\rho)\widehat{E_i} \\ u^h(x) = \mathbf{\Phi}^{(1D)^T}(x)\cdot \hat{\mathbf{u}} = \sum_{i=1}^{M} \varphi_i^{(1D)}(x)\widehat{u_i} \\ v^h(x) = \mathbf{\Psi}^{(1D)^T}(x)\cdot \hat{\mathbf{v}} = \sum_{i=1}^{M} \psi_i^{(1D)}(x)\widehat{v_i} \end{cases}, \quad (6)$$

with:

$$\begin{cases} \hat{\mathbf{E}} = \left[\widehat{\mathbf{E}_G}^T \quad \widehat{\mathbf{E}_W}^T \quad \widehat{\mathbf{E}_C}^T\right] \\ \widehat{\mathbf{E}_G} = \begin{bmatrix} \widehat{E_1} \\ \vdots \\ \widehat{E_M} \end{bmatrix}, \widehat{\mathbf{E}_W} = \begin{bmatrix} \widehat{E_{M+1}} \\ \vdots \\ \widehat{E_P} \end{bmatrix}, \widehat{\mathbf{E}_C} = \begin{bmatrix} \widehat{E_{P+1}} \\ \vdots \\ \widehat{E_N} \end{bmatrix}, \\ \hat{\mathbf{u}} = \left[\widehat{u_1} \ldots \widehat{u_M}\right]^T, \hat{\mathbf{v}} = \left[\widehat{v_1} \ldots \widehat{v_M}\right]^T \end{cases} \quad (7)$$

where E^h and u^h are interpolated values of E and u, respectively, and v^h is the approximated value of v. Subscripts G, W and C denote gap, wall and internal crack nodes. For generating the system of equations, we collocate sides of (1) and (5) at the nodes. Considering the first equations in (1) and (6),

$$\xi_{TE}(E) = 0 \Rightarrow \sum_{q=1}^{N} \xi_{TE}\left[\varphi_q^{(2D)}(\rho_p)\right]\widehat{E_q} = 0, \quad \Rightarrow \mathbf{M}_1 \cdot \hat{\mathbf{E}} = 0. \quad (8)$$

where:

$$\left[\mathbf{M}_1\right]_{pq} = \xi_{TE}\left[\varphi_q^{(2D)}(\rho_p)\right]. \quad (9)$$

Next, substituting the expansion of u represented in (6) in the first equation of (5) leads to:

$$\sum_{q=1}^{M} \varphi_q^{(1D)}(\rho_p)\widehat{u_q} = \sum_{q=1}^{M}\left[(j/2)\int\limits_{\Gamma_a} \psi_q^{(1D)}(x') H_0^{(2)}\left(k_0|\rho_p - x'|\right)dx'\right]\widehat{v_q}, \quad (10)$$

$$\Rightarrow \mathbf{M}_2 \cdot \hat{\mathbf{u}} = \mathbf{M}_3 \cdot \hat{\mathbf{v}}.$$

where:

$$\begin{cases} \left[\mathbf{M}_2\right]_{pq} = \varphi_q^{(1D)}(\rho_p) \\ \left[\mathbf{M}_3\right]_{pq} = (j/2)\int\limits_{\Gamma_a} \psi_q^{(1D)}(x') H_0^{(2)}\left(k_0|\rho_p - x'|\right)dx' \end{cases}. \quad (11)$$

Similarly for v,

$$\sum_{q=1}^{M} \psi_q^{(1D)}(\rho_p)\widehat{v_q} = \sum_{q=1}^{N} \varphi_q^{(2D)}(\rho_p)\widehat{E_q},\ p \le M, \quad \Rightarrow \mathbf{M}_4 \cdot \hat{\mathbf{v}} = \mathbf{M}_5 \cdot \hat{\mathbf{E}}, \quad (12)$$

where:

$$\begin{cases} \left[\mathbf{M}_4\right]_{pq} = \psi_q^{(1D)}(x_p) \\ \left[\mathbf{M}_5\right]_{pq} = \varphi_q^{(2D)}(\rho_p),\ p \le M \end{cases}. \quad (13)$$

Finally, the second equation of (1) gives:

$$\sum_{q=1}^{N}\left[\mu_r^{-1}(\rho_p)\varphi_{q,y}^{(2D)}(\rho_p)\right]\widehat{E_q} + \sum_{q=1}^{M} j/2\left[k_0^2\varphi_q^{(1D)}(\rho_p) + \varphi_{q,xx}^{(1D)}(\rho_p)\right]\widehat{u_q} = q_{TE}, \quad (14)$$

$$\Rightarrow \mathbf{M}_6 \cdot \hat{\mathbf{E}} + \mathbf{M}_7 \hat{\mathbf{u}} = \hat{\mathbf{q}},$$

where:

$$\begin{cases} \left[\mathbf{M}_6\right]_{pq} = \mu_r^{-1}(\rho_p)\varphi_{q,y}^{(2D)}(\rho_p)\Big|_{y=0^-} \\ \mathbf{M}_7 = k_0^2\mathbf{M}_2 + \mathbf{M}_8 \\ \hat{\mathbf{q}} = \left[q_{TE}(x_1) \quad \cdots \quad q_{TE}(x_M)\right]^T \end{cases}, \quad (15)$$

with $\left[\mathbf{M}_8\right]_{pq} = (j/2)\varphi_{q,xx}^{(1D)}(x_p)$.

Therefore, the corresponding system of equation is:

$$\mathbf{M}_1 \cdot \hat{\mathbf{E}} = 0 \quad (16)$$

which can be uniquely solved after imposition of the following linear set of conditions:

$$\begin{cases} \left(\mathbf{M}_6 + \mathbf{M}_7\mathbf{M}_2^{-1}\mathbf{M}_3\mathbf{M}_4^{-1}\mathbf{M}_5\right)\hat{\mathbf{E}} = \hat{\mathbf{q}} \\ \widehat{\mathbf{E}_W} = 0 \end{cases} \quad (17)$$

Once $\hat{\mathbf{E}}$ is computed, the field variable E can be interpolated at any point in the domain and on the problem boundary.

IV. COMPUTING THE ENTRIES OF $\mathbf{M}_3$

Among $\mathbf{M}_i$ matrices, $1 \le i \le 8$, The only time-consuming one is $\mathbf{M}_3$. In this section, two approaches are suggested for this purpose, one in the space domain and the other in the spectral domain. The latter is our proposed method.

A. Space domain

A choice of computing the entries of $\mathbf{M}_3$ in the space domain is performing the following two steps. First, the Green's function is decomposed into singular and oscillatory parts, i.e.:

$$G = G_{Sing} + G_{Oscill}, \tag{18}$$

where:

$$\begin{cases} G = H_0^{(2)}(k_0\rho) \\ G_{Sing} = (2/j\pi)\ln(k_0\rho) \\ G_{Oscill} = H_0^{(2)}(k_0\rho) - (2/j\pi)\ln(k_0\rho) \end{cases}. \tag{19}$$

Second, the oscillatory part is integrated by a standard quadrature, e.g. Gauss-Legendre and the singular part by the quadrature rule given in [28].

B. Spectral domain

This is our suggested method and requires the crack nodes to be arranged equidistance. By doing so, all of the $\psi_i^{(1D)}$ shape functions are shifted version of each other. Furthermore, the study of Shepard functions shows that they can be well approximated by a single Gaussian function. Thus, the mathematical form of the $\mathbf{M}_3$ entries can be approximated by:

$$\begin{cases} P = S * G \\ S(\rho) = \alpha \exp(-\beta\rho^2) \end{cases}, \tag{20}$$

where α and β are positive real constants to be determined by approximating a representative such as the central node approximant by a Gaussian function. Here, "*" stands for linear convolution. Since the spectrum of a Gaussian function is practically band limited, (18) could be efficiently computed by the fast Fourier transform (FFT), i.e.:

$$P = FFT^{-1}\{FFT\{S\} \cdot FFT\{G\}\}. \tag{19}$$

V. NUMERICAL RESUILTS

In this section, we have applied the proposed meshfree method to the same problems addressed in [3], with the geometry as depicted in Fig. 2. The convergence analysis curves are provided for rigorously validating the method [29]. Thin-plate spline (TPS) functions are used for construction of meshfree shape functions [7]. The influence domain of Shepard functions are selected to be $1.5\times(D_x^2 + D_y^2)^{1/2}$ where D_x and D_y are nodal spacing in x and y directions, respectively. Additionally, for error estimate we used:

$$r_e(u_1, u_2) = \|u_1 - u_2\| / \|u_1\|, \tag{20}$$

where $\|u\| = 1/2\left(\int_\Omega |u|^2\, d\Omega\right)^{1/2}$.

Consider a gap with w = 1λ and d = 0.25λ. Two sets of supporting nodes are used for meshless discretization; regular and randomly distributed, as depicted in Fig. 3. Figure 4 depicts the convergence curves for both polarizations and different filling materials at normal incidence based on regular node arrangement. The electric filed distribution at the crack opening for normal TE incidence for both node arrangements are depicted in Fig. 5 and the modal solution that validates the proposed method. Normalized scattering width as a function of incidence angle and frequency for TE and TM polarizations are depicted in Fig. 6, assuming regular node arrangement. Finally, the computational cost of evaluating $\mathbf{M}_3$ entries in space and spectral domains are compared in Fig. 7.

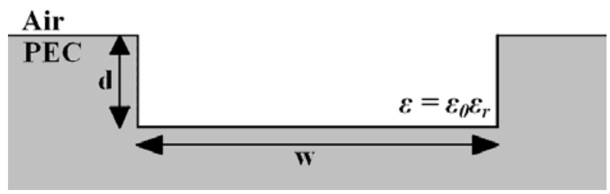

Fig. 2. Geometry of the rectangular crack.

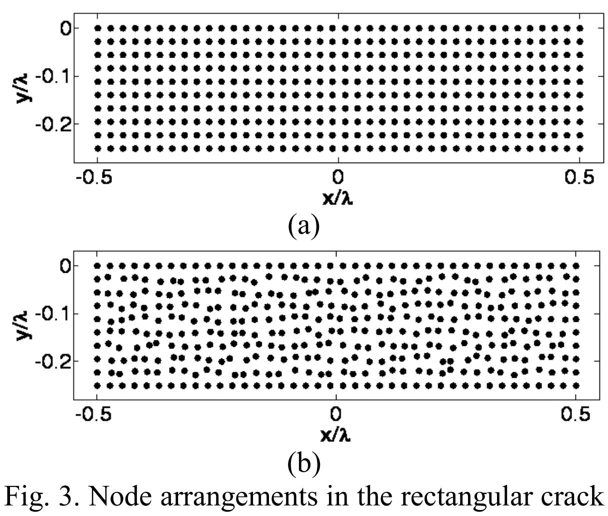

Fig. 3. Node arrangements in the rectangular crack with w = 1λ, d = 0.25λ: (a) regular, (b) random.

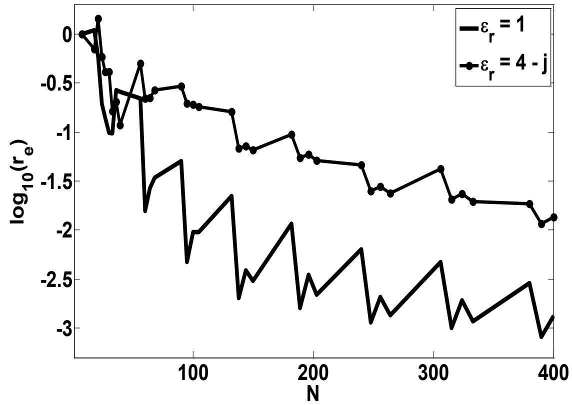

(a)

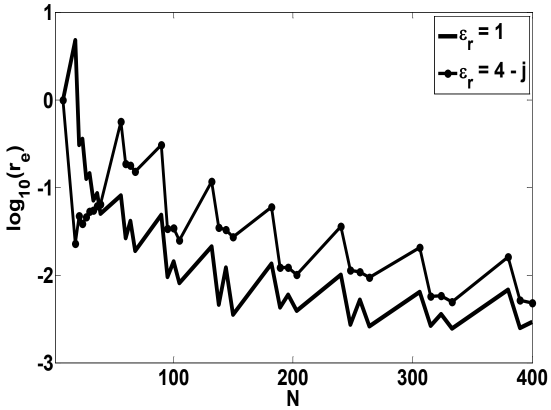

(b)

Fig. 4. Convergence curves for w = 1λ and d = 0.25λ at normal incidence: (a) TE polarization. (b) TM polarization.

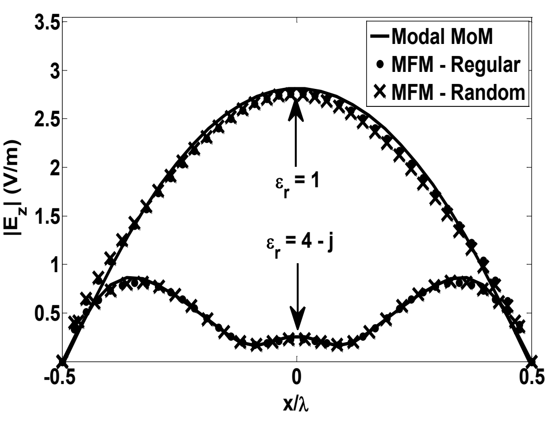

(a)

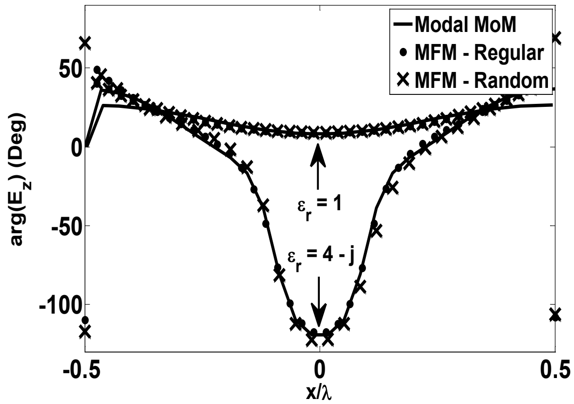

(b)

Fig. 5. Electric filed distribution at the crack opening for w = 1λ and d = 0.25λ at normal TE incidence: (a) magnitude, (b) phase.

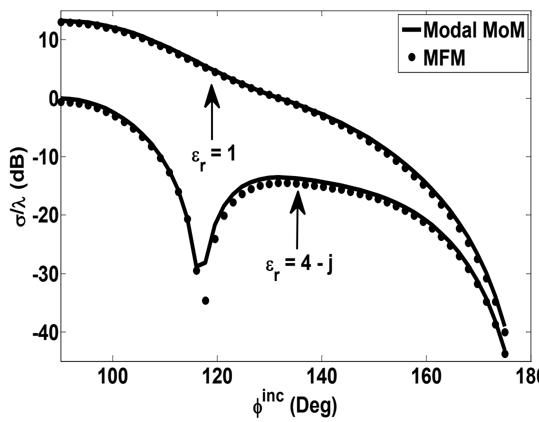

(a)

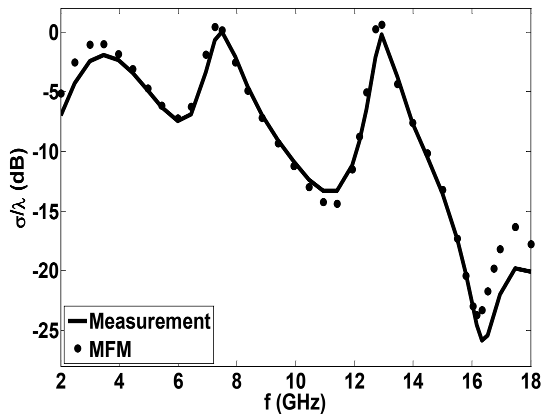

(b)

Fig. 6. Normalized scattering width as a function of (a) angle for w = 1λ and d = 0.25λ for TE incidence, (b) frequency for w = 2.5 cm and d = 1.25 cm for an air filled crack for TM incidence at φ = 10° (measurement results from [3]).

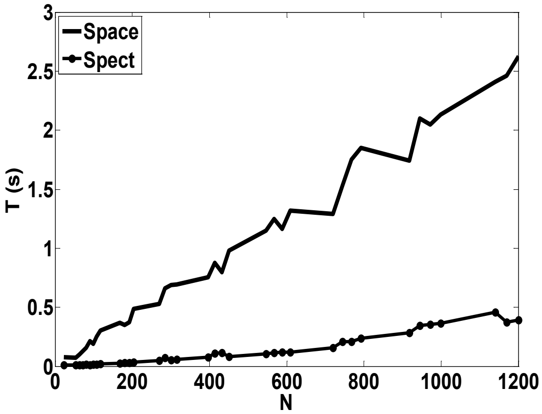

Fig. 7. Computational cost of evaluating $\mathbf{M}_3$ entries in space and spectral domains for a sample simulation.

VI. CONCLUSION

In this paper, the problem of EM scattering by a 2D crack is solved by meshfree collocation method. The selected formulation is hybrid PDE-IE that can handle a general shaped crack filled with an arbitrary material. A proper choice of meshless shape functions for PDE and IE parts are used for efficient meshless discretization. Additionally, a method is proposed to bypass numerical integration by exploiting FFT. Thus, a general, fast, and accurate meshfree method is developed. Convergence analysis, modal solution, and measurement data validate the approach.

ACKNOWLEDGMENT

The authors appreciate Prof. M. Dehghan for inputs in meshfree methods.

REFERENCES

[1] K. Barkeshli, J. L. Volakis, “Scattering by a Two Dimensional Groove in a Ground Plane,” Technical report for NASA grant NAG-2-541, The Radiation Laboratory, Department of Electrical Engineering and Computer Science, The University of Michigan, Ann Arbor, MI, 1989.

[2] T. B. A. Senior, K. Sarabandi, and J. R. Natzke, “Scattering by Narrow Gap,” *IEEE Trans. Antennas Propagat.*, vol. 38, no. 7, pp. 1102-1110, 1990.

[3] J. Jin, *The Finite Element Method in Electromagnetics, Second Edition*. John Wiley & Sons, 2002.

[4] M. Bozorgi and A. Tavakoli, “Polarimetric Scattering from a 3-D Rectangular Crack in a PEC Covered by a Dielectric Layer,” *Applied Computational Electromagnetics Society (ACES) Journal*, vol. 26, no. 6, pp. 502 - 511, June 2011.

[5] F. Deek, M. El-Shenawee, “Microwave Detection of Cracks in Buried Pipes using the Complex frequency Technique,” *Applied Computational Electromagnetics Society (ACES) Journal*, vol. 25, no. 10, pp. 894 - 902, October 2010.

[6] Richard K. Gordon, W. Elliott Hutchcraft, “The Use of Multiquadric Radial Basis Functions in Open Region Problems,” *Applied Computational Electromagnetics Society (ACES) Journal*, vol. 21, no. 2, pp. 127 - 134, July 2006.

[7] G. R. Liu, *Mesh Free Methods*. CRC Press, 2003.

[8] Y. Marechal, “Some Meshless Methods for Electromagnetic Field Computations,” *IEEE Trans. Magn.*, vol. 34, no. 5, pp. 3351-3354, 1998.

[9] C. Herault and Y. Marechal, “Boundary and Interface Conditions in Meshless Methods,” *IEEE Trans. Magn.*, vol. 35, no. 3, pp. 1450-1453, 1999.

[10] S. L. Ho, S. Yang, J. M. Machado, and H. C. Wong, “Application of a Meshless Method in Electromagnetics,” *IEEE Trans. Magn.*, vol. 37, no. 5, pp. 3198-3201, 2001.

[11] L. Xuan, Z. Zeng, B. Shanker, and L. Udpa, “Meshless Method for Numerical Modeling of Pulsed Eddy Currents,” *IEEE Trans. Magn.*, vol. 40, no. 6, pp. 3457-3462, 2004.

[12] S. L. Ho, S. Shiyou Yang, H. C. Wong, and G. Ni, “Meshless Collocation Method Based on Radial Basis Functions and Wavelets,” *IEEE Trans. Magn.*, vol. 40, no. 2, pp. 1021-1024, 2004.

[13] S. L. Ho, S. Shiyou Yang, G. Ni , H. C. Wong, and Y. Wang, “Numerical Analysis of Thin Skin Depths of 3-D Eddy-Current Problems using a Combination of Finite Element and Meshless Methods,” *IEEE Trans. Magn.*, vol. 40, no. 2, pp. 1354-1357, 2004.

[14] S. L. Ho, S. Shiyou Yang, H. C. Wong, E. W. C. Lo, and G. Ni, “Refinement Computations of Electromagnetic Fields using FE and Meshless Methods,” *IEEE Trans. Magn.*, vol. 41, no. 5, pp. 1456-1459, 2005.

[15] Y. Zhang, K. R. Shao, D. X. Xie, and J. D. Lavers, “Meshless Method Based on Orthogonal Basis for Electromagnetics,” *IEEE Trans. Magn.*, vol. 41, no. 5, pp. 1432-1435, 2005.

[16] Q. Li and K. Lee, “Adaptive Meshless Method for Magnetic Field Computation,” *IEEE Trans. Magn.*, vol. 42, no. 8, pp. 1996-2003, 2006.

[17] Y. Zhang, K. R. Shao, J. Zhu, D. X. Xie, and J. D. Lavers, “A Comparison of Point Interpolative Boundary Meshless Method Based on PBF and RBF for Transient Eddy-Current Analysis,” *IEEE Trans. Magn.*, vol. 43, no. 4, pp. 1497-1500, 2007.

[18] F. G. Guimaraes, R. R. Saldanha, R. C. Mesquita, D. A. Lowther, and J. A. Ramirez, “A Meshless

Method for Electromagnetic Field Computation Based on the Multiquadratic Technique," *IEEE Trans. Magn.*, vol. 43, no. 4, pp. 1281-1284, 2007.

[19] S. Ikuno, K. Takakura, and A. Kamitani, "Influence of Method for Imposing Essential Boundary Condition on Meshless Galerkin/Petrov-Galerkin Approaches," *IEEE Trans. Magn.*, vol. 43, no. 4, pp. 1501-1504, 2007.

[20] S. McFee, D. Ma, and M. Golshayan, "A Parallel Meshless Formulation for *h-p* Adaptive Finite Element Analysis," *IEEE Trans. Magn.*, vol. 44, no. 6, pp. 786-789, 2008.

[21] Y. Yu and Z. Chen, "Towards the Development of an Unconditionally Stable Time-Domain Meshless Method," *IEEE Trans. Microwave Theory Tech*., vol. 58, no. 3, pp. 578- 586, 2010.

[22] Y. Yu and Z. Chen, "A 3-D Radial Point Interpolation Method for Meshless Time-Domain Modeling," *IEEE Trans. Microwave Theory Tech.*, vol. 57, no. 8, pp.2015-202, 2009.

[23] T. Kaufmann, C. Fumeaux, and R. Vahldieck, "The Meshless Radial Point Interpolation Method for Time-Domain Electromagnetics," *IEEE MTT-S Int. Microwave Symp. Dig.*, Atlanta, pp. 61 - 64, 2008.

[24] T. Kaufmann, C. Engström, C. Fumeaux, and R. Vahldieck, "Eigenvalue Analysis and Longtime Stability of Resonant Structures for the Meshless Radial Point Interpolation Method in Time Domain," *IEEE Trans. Microwave Theory Tech*, vol. 58, pp. 3399 - 3408, 2010.

[25] G. R. Liu and Y. T. Gu, *An Introduction to MeshFree Methods and Their Programming*. Springer, 2005.

[26] R. Schaback, "Limit problems for interpolation by analytic radial base functions," *Comp. Appl. Math.*, vol. 212, no. 2, pp. 127-149, 2008.

[27] D. Shepard, "A Two Dimensional Interpolation Function for Irregularly Spaced Data," in *Proc. 23rd Nat. Conf. ACM*, 1968, pp. 517–523.

[28] A. H. Stroud and D. Secrest, *Gaussian Quadrature Formulas*, Prentice Hall, N.Y., 1966.

[29] J. C. Rautio, "The Microwava Point of View on Software Validation," *IEEE Antennas Propagat. Mag*., vol. 38, no. 2, pp. 68-71, 1996.

Babak Honarbakhsh was born in Tehran, Iran. He received his B.S. and M.S. degrees in Electrical Engineering from Amirkabir University of Technology where he is currently working toward his Ph.D. degree. His current research interest is numerical solution of electromagnetic problems by mesh free methods.

Ahad Tavakoli was born in Tehran, Iran, on March 8, 1959. He received B.S. and M.S. degrees from the University of Kansas, Lawrence, and the Ph.D. degree from the University of Michigan, Ann Arbor, all in Electrical Engineering, in 1982, 1984, and 1991, respectively.

He is currently a Professor in the Department of Electrical Engineering at Amirkabir University of Technology. His research interests include EMC, scattering of electromagnetic waves and microstrip antennas.

Efficient Analysis of Switchable FSS Structure using the WCIP Method

N. Sboui[1], A. Salouha[1], L. Latrach[1], A. Gharsallah[1], A. Gharbi[1], and H. Baudrand[2]

[1]Laboratoire d'Electronique Département de Physique
Faculté des Sciences de Tunis, 2092 El Manar Tunisia
noureddine.sboui@fst.rnu.tn

[2]Laboratoire d'Electronique
EN SEEIHT de Toulouse France

Abstract**—**A precise technique based on the wave concept iterative procedure (WCIP) and a fast mode transformation (FMT) is used to adjust the frequency selective surface (FSS) response. This adjustment is achieved by integrating RF-MEMS switches. These systems use the manufacturing processes of integrated circuits. In order to initialize the iterative procedure, an incident wave is defined in spectral domain. The numerical results are compared to those obtained with the finite element method (FEM). The good agreement between simulated and published data justifies the design procedure.

Index Terms — FSS, MEMS RF, 2D-FFT algorithm.

I. INTRODUCTION

The frequency selective surfaces (FSS) are printed by surfaces composed of a periodic metallic circuit or openings in a circuit plane. They can be periodic along one or two directions [1-3]. They provide a reflection or total transmission of signals in certain frequency bands [4-5]. We can adjust this frequency of resonance by integrating a PIN diode, FET, or RF MEMS switch. The semiconductor switches are used first. They present some limitation in terms of energy consumption, insertion loss and cut-off frequency. The RF-MEMS switches are devices that use a mechanical movement to assign a switching of the RF transmission line [6-8]. The principal advantages of the RF-MEMS switches are low consumption, low insertion loss and quality factor [3]. Their application areas are extensive and always tend to grow. The most used switching techniques are the air bridge technology and technique of micro beam [9-10].

The contact switch is the equivalent of the RF-MEMS switch. It has two states of commutation: the state ‘‘off’’ and the state ‘‘on’’. In a blocked state, the switch has a capacitive behavior, with the state passing; it is comparable to a resistance representing the losses of a metal/metal contact.

We can distinguish several categories of components from this technology; our study will focus on the resistive switch (cantilever). Indeed these components have many advantages compared to their direct competitors, semi-conductors: reduced losses, more compact and passive components.

Simulation is an essential step in modeling this type of circuit. In this framework, several analytical methods have been developed. Among these methods that already exist, we present in what follows a new iterative method based on the wave concept. This method has major advantages over other methods. These advantages are concerning, in special, the execution velocity of the resolution procedure and the arbitrary form of the under studied structure. Besides this iterative technique uses a rapid transformation FMT which ensures a rapid transition between the spectral and spatial domain [11-12]. We combine the wave concept with the two dimensions fast Fourier transformation (2D-FFT) algorithm to change the domain. The use of the 2D-FFT algorithm is required to mesh the circuit plane into 2D small rectangular pixels. Hence, the boundary conditions are satisfied at each pixel. By using the 2D-FFT algorithm, a high computational speed can be achieved [13].

The purpose of this paper is to extend the wave concept iterative process (WCIP) method to the analysis of the integration of microsystems

Submitted On: Oct. 8, 2010
Accepted On: Feb. 11, 2011

1054-4887

performance (MEMS) in circuit materials periodic FSS (infinite number of unit cells) with arbitrary angle of incidence in the one layer configuration of dielectrics [3]. Two different examples are studied, switchable split-ring FSS and switched-beam antenna. For both cases, our simulation results are validated with published data.

II. THEORY

Let us consider a periodic arbitrary one-layer structure, Fig. 1 shows the unit cell of periodic circuit.

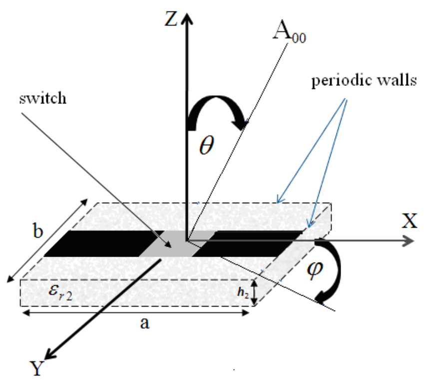

Fig. 1. Unit cell of the periodic structure with arbitrary incidence A_{00}.

This interface can support the circuit and includes three sub-domains metal M_i, dielectric D_i, and switch SW_i. We consider that the electromagnetic field is known on all points of the plane interface [7]. The solution of the problem has to satisfy the following boundary conditions:

$$\begin{cases} E_{T1} = E_{T2} = 0 & Metal(M) \\ J_T = J_{T1} + J_{T2} & Dielectric(D) \\ J_{sw} = y_{sw} E_{sw} & Switch(SW) \end{cases} \quad (1)$$

In equation (1), E_{T1} and E_{T2} are the tangential components of the electric field at media (1) and (2), respectively, and JT1 and JT2 are the corresponding current density. E_{SW}, J_{SW}, and y_{SW} are the electric field, the current density, and the admittance equivalent circuit of the switch domain respectively.

In the last domain, the electric field and the current density are related to the potential and electric current as follows:

$$E_{sw} = \frac{V_1}{G} \quad ; \quad J_{sw} = \frac{I}{W} \,. \quad (2)$$

This enables us to write

$$\frac{J_{sw}}{E_{sw}} = \frac{I}{V_1}\left(\frac{G}{W}\right) = Y_{sw}\left(\frac{G}{W}\right) = y_{sw} \,. \quad (3)$$

As shown on Fig. 2, the incident waves A_i and the scattering waves B_i are given in the terms of the transverse electric E_{Ti} and magnetic fields H_{Ti} at the circuit interface (**Ω**). This leads to the following set of equations:

$$\begin{cases} A_i = \dfrac{\sqrt{y_{0i}}}{2}\left(E_{Ti} + \dfrac{1}{y_{0i}}(H_{Ti} \times n)\right) \\ B_i = \dfrac{\sqrt{y_{0i}}}{2}\left(E_{Ti} - \dfrac{1}{y_{0i}}(H_{Ti} \times n)\right) \end{cases} \quad (4)$$

where y_{0i} is an intrinsic admittance characterizing the medium, i denotes the two media beside **Ω** (i=1 and 2), which can be defined as: $y_{0i} = \sqrt{\dfrac{\varepsilon_0 \varepsilon_{ri}}{\mu}}$ with ε_0, μ_0, and ε_{ri} are the permittivity and permeability of the vacuum and the relative permittivity of the medium 'i' respectively. n is the outward vector normal to the interface.

The surface current density is introduced as being $J_{Ti} = H_{Ti} \times n$.

On the dielectric:

$$\left\{ \begin{vmatrix} B_1 \\ B_2 \end{vmatrix} = \left[S_D \right] \begin{vmatrix} A_1 \\ A_2 \end{vmatrix} \right\}_{x,y} , \quad (5)$$

$$\left[S_D \right] = \begin{bmatrix} \dfrac{1-n_{12}}{1+n_{12}} & \dfrac{2n_{12}}{1+n_{12}} \\ \dfrac{2n_{12}}{1+n_{12}} & -\dfrac{1-n_{12}}{1+n_{12}} \end{bmatrix}, \quad (6)$$

where $n_{12} = \dfrac{y_{01}}{y_{02}}$.

On the switch:

$$\left\{ \begin{vmatrix} B_1 \\ B_2 \end{vmatrix} = \left[S_{SW} \right] \begin{vmatrix} A_1 \\ A_2 \end{vmatrix} \right\}_{x,y} , \quad (7)$$

$$\left[S_{SW} \right] = \begin{bmatrix} \dfrac{-1-n_{s1}+n_{s2}}{1+n_{s1}+n_{s2}} & \dfrac{2n_s}{1+n_{s1}+n_{s2}} \\ \dfrac{2n_s}{1+n_{s1}+n_{s2}} & -\dfrac{1+n_{s1}-n_{s2}}{1+n_{s1}+n_{s2}} \end{bmatrix},$$

$$n_{s1} = \frac{y_{sw}}{y_{01}},\ n_{s2} = \frac{y_{sw}}{y_{02}} \ and \ n_s = \frac{\sqrt{y_{01} y_{02}}}{y_{sw}} \,.$$

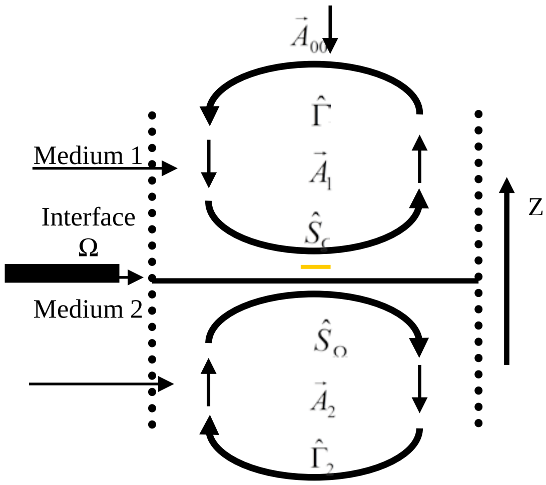

Fig. 2. Definition of waves for the single-layer structure.

With equations (5), (6), and (7), we deduce the global spatial equation that relates the incident waves on all the interfaces.

$$\left\{ \begin{vmatrix} B_1 \\ B_1^{'} \end{vmatrix} = [S] \begin{vmatrix} A_1 \\ A_1^{'} \end{vmatrix} \right\}_{x,y}, \tag{8}$$

where:

$$[S] = \hat{H}_M [S_M] + \hat{H}_D [S_D] + \hat{H}_{SW} [S_{SW}] + A_{00},$$

and

$$\hat{H}_\pi = \begin{cases} 1 & if \quad \pi = M_i, D_i \ or \ SW_i \\ 0 & else\ where \end{cases}.$$

Between medium 1 and 2, the waves are defined in the spectral domain (TE and TM modes). Then, the spectral equations describe the waves behaviour is defined as [4].

$$\left\{ A_i = \hat{\Gamma}_i B_i \right\}_\alpha, \tag{9}$$

$$\hat{\Gamma}_{i\alpha} = \frac{Z_{mni\,\alpha} - z_{0i}}{Z_{mni\,\alpha} + z_{0i}}, \tag{10}$$

where, i=1,or 2 and $Z_{mni\,\alpha}$ is the impedance of the mn-th mode at the medium i and α stands for the modes TE or TM.

where: $Z_{mni\,TE} = \frac{j\omega\mu_0}{\gamma_{mni}}$, $Z_{mni\,TM} = \frac{\gamma_{mni}}{j\omega\varepsilon_0\varepsilon_{ri}}$

γ_{mni} being the propagation constant of the medium i and it is given by

$$\gamma_{mni} = \sqrt{\beta_{xm}^2 + \beta_{yn}^2 - k_0^2 \varepsilon_{ri}},$$

$$k_0 = \omega\sqrt{\mu_0\varepsilon_0}, \omega = 2\pi\frac{c}{\lambda},$$

$$\beta_{xm} = \beta_x + \frac{2m\pi}{a}, \ \beta_{yn} = \beta_y + \frac{2n\pi}{b}.$$

$$\beta_x = \omega\sqrt{\varepsilon_{r1}\mu_{r1}}\sqrt{\varepsilon_0\mu_0}\sin\theta\cos\varphi,$$

$$\beta_y = \omega\sqrt{\varepsilon_{r1}\mu_{r1}}\sqrt{\varepsilon_0\mu_0}\sin\phi\cos\theta.$$

(a) and (b) are the periodicity along (ox) and (oy), respectively, θ and φ define the angle of incidence.

We deduce that the global spectral equation relates the diffracted wave A_i to incident B_i one in the spectral domain.

$$A_i^{k+1} = \hat{\Gamma}_i B_i^{(k)} + A_0. \tag{11}$$

In the above equation, we have included the excitation wave $A_{00} = \begin{vmatrix} A_{ox} \\ A_{oy} \end{vmatrix}$. A_{00} is defined in the spectral domain and has the following expression:

For TE polarization:

$$\begin{cases} A_{0x} = \dfrac{1}{2\sqrt{Z_{oi}}} \dfrac{\beta_y}{\sqrt{|\beta_x|^2 + |\beta_y|^2}} \dfrac{1}{\sqrt{ab}} e^{-j(\beta_x x + \beta_y y)} \\ A_{0y} = \dfrac{-1}{2\sqrt{Z_{oi}}} \dfrac{\beta_x}{\sqrt{|\beta_x|^2 + |\beta_y|^2}} \dfrac{1}{\sqrt{ab}} e^{-j(\beta_x x + \beta_y y)} \end{cases}. \tag{12}$$

For TM polarization:

$$\begin{cases} A_{0x} = \dfrac{-1}{2\sqrt{Z_{oi}}} \dfrac{\beta_x}{\sqrt{|\beta_x|^2 + |\beta_y|^2}} \dfrac{1}{\sqrt{ab}} e^{-j(\beta_x x + \beta_y y)} \\ A_{0y} = \dfrac{1}{2\sqrt{Z_{oi}}} \dfrac{\beta_y}{\sqrt{|\beta_x|^2 + |\beta_y|^2}} \dfrac{1}{\sqrt{ab}} e^{-j(\beta_x x + \beta_y y)} \end{cases}. \tag{13}$$

III. APPLICATIONS

The RF MEMS switches are mechanically deformable micro switches. In the first step of this first example, we studied FSS a screen which integrates a PIN diode into two borderline cases (short-circuit and open circuit), as shown in Fig. 3.

The structure is excited by a plane wave with normal incidence. The physical parameters are the following: height of the substrate h=0.6mm its permittivity ε_r=3. The unit cell dimension are a=b=40mm. The microstrip line length L=40mm and its width W=1mm, as shown in Fig. 3.

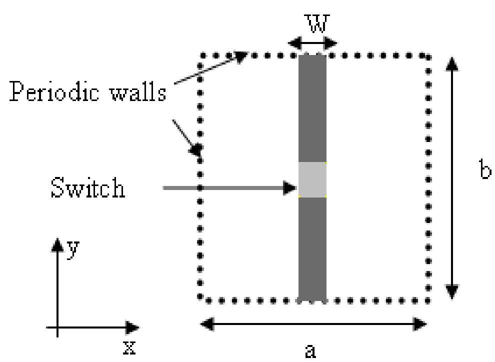

Fig. 3. Resistive switch inserted on a microstrip line.

The convergence according to the iteration count presented in Fig. 4 is obtained from 50 iterations.

For the short circuit case, the simulation results of the transmission coefficient, as a function of frequency, is shown in Fig. 5. This shows that there is a total transmission signal. This result compared to [15], shows there is a good agreement with the iterative method.

In the open circuit case, one can conclude from the simulation result presented in Fig. 6 that the gap has given rise to a band gap in a well determined frequency. In fact in our simulation, we use only a gap where a pin diode in the gap state is used [15]. This explains the difference in bandwidth between the two results.

As a consequence of this important aspect, elements are inserted into the gap to achieve switching DC-electric and have thereby controlling electronic structures, FSS, changing their behavior between the response of discontinuous and continuous elements.

For different values of the capacitor, we present, in Figs. 7 to 9, the results of simulations of transmission coefficients as a function of frequency. In these figures, we clearly distinguish the effect of integration of the switch to the off state. We notice the changes in the resonant frequency when the capacitance changes.

The results presented by the iterative method are in agreement with those published by the finite element method (FEM).

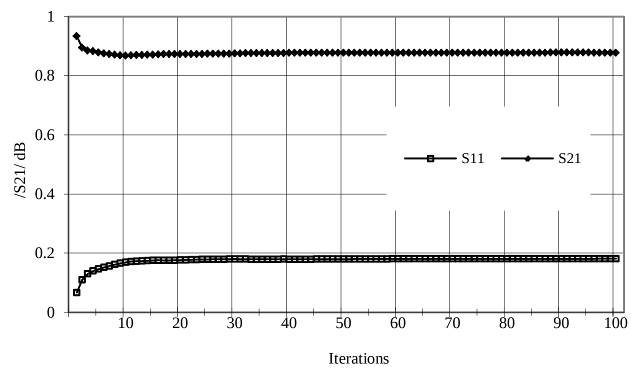

Fig. 4. Convergence of the S parameters as function of iterations number at 7 GHz.

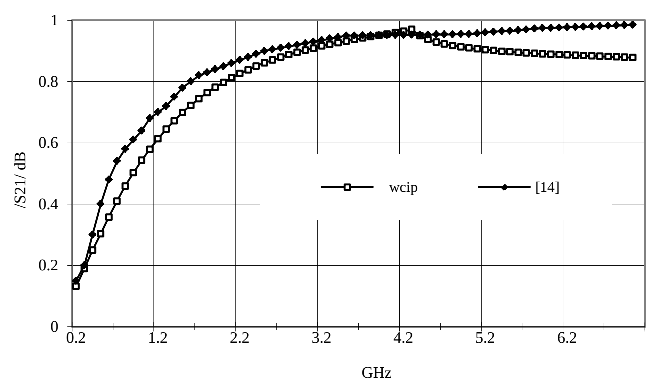

Fig. 5. Variation of transmission coefficient as function of frequency (short circuit case).

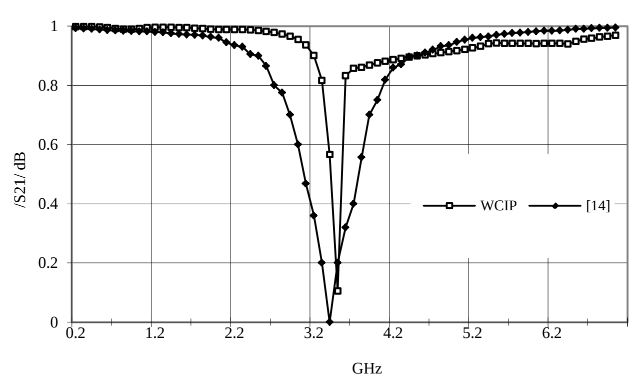

Fig. 6. Variation of transmission coefficient as function of frequency (open circuit case).

In the second example, we integrate three capacitive switches between two rings of split-ring resonator (SRR), as shown in Fig. 10. At first, we consider the ON state of all of the three switches.

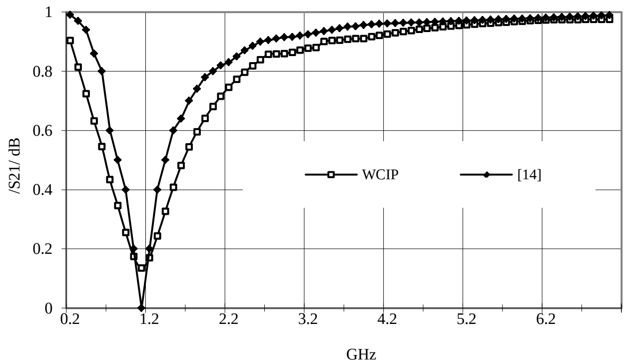

Fig. 7. Variation of transmission coefficient as a function of frequency c=1pF.

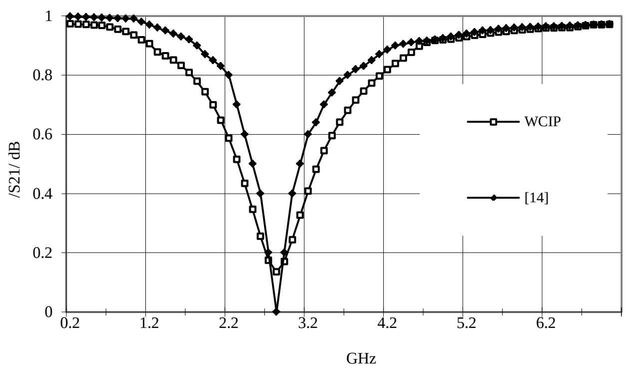

Fig. 8. Variation of transmission coefficient as a function of frequency c=100pF.

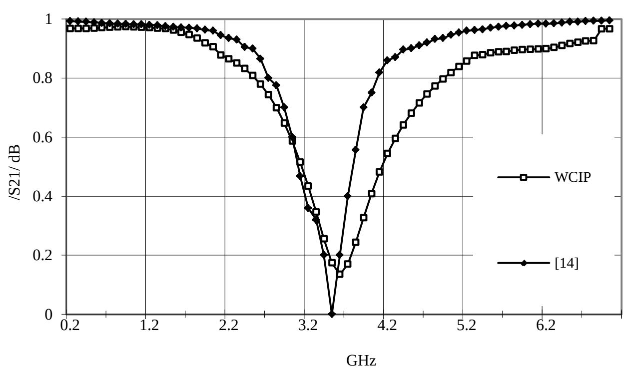

Fig. 9. Variation of transmission coefficient S_{21} as a function of frequency c=0pF.

As shown in Fig. 11, we find that the transmission coefficient obtained using the iterative method is about -22 dB at 4.64GHz. These results refer to those obtained by the FEM [15].

The second phase consists of integrating two capacitors' switches and a resistive switch into the place of the metal packing, to be able to distinguish the effect of integration from the switches between the rings of the resonator. Two cases will be presented, the first case or the three switches has state off, and the three switches (S1, S2, and S3) take the values, respectively, (0.3pf, 0.3pf, and 1 Ω).

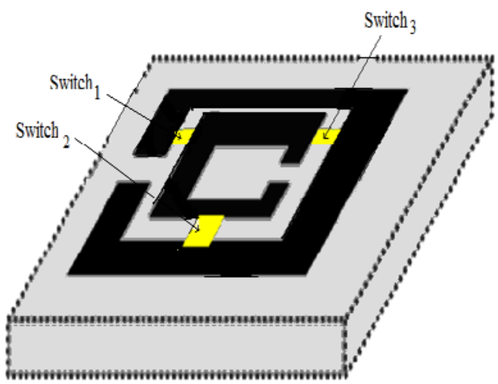

Fig. 10. Two enclosed rings with three switches (S1, S2, S3).

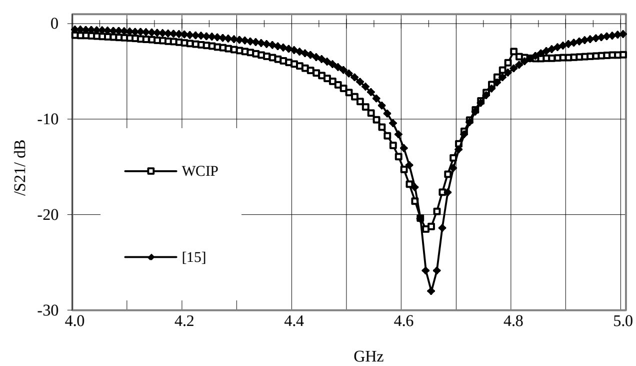

Fig. 11. Variation of transmission coefficient as a function of frequency.

Figure 12 presents the coefficient of transmission in dB and suggests the frequency of resonance to 4.57 GHz with a transmission of about -28 dB. The state ''ON'' the three switches (S1, S2, and S3) takes successively the values (1pf, 1pf, and 5 Ω).

Figure 13 presents the coefficient of transmission in dB and shows a frequency of resonance to 4.57 GHz with a transmission of about -23 dB.

Figure 14 enables us to distinguish the difference between the various cases from commutations (S1, S2, and S3) compared to the answer of metal modeling obtained by the iterative method.

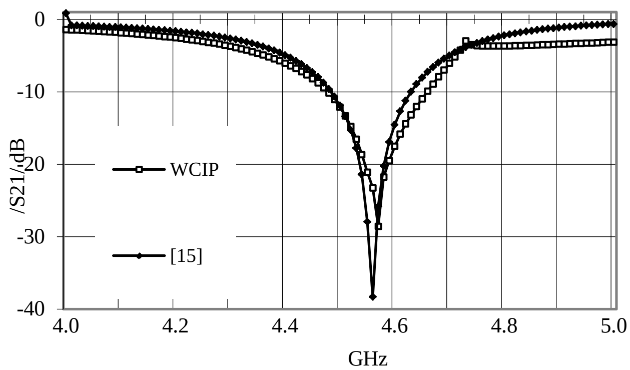

Fig. 12. Variation of transmission coefficient as a function of frequency with C1=C2=0.3pF and R=1Ω.

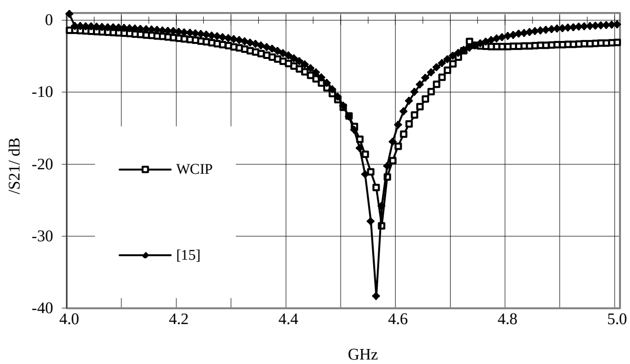

Fig. 13. Variation of transmission coefficient as a function of frequency with C1=C2=1pF and R=5Ω.

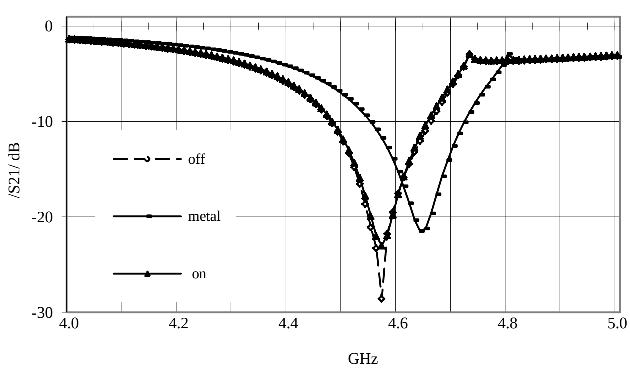

Fig. 14. Variation of transmission coefficient as a function of frequency.

IV. CONCLUSION

In this paper, a reformulation of the wave concept iterative method is reformulated to the integrated RF-MEMS switch. The convergence of the procedure is about 100 iterations. The comparison of numerical results with the measurement published data verified the validation of the WCIP method to integrating the RF Switch. This method has the advantage of simplicity and its conjunction with the 2D-FFT allows a high computational speed and memory consumption.

REFERENCES

[1] B. A. Munk, *Frequency Selective Surfaces: Theory and Design*, John Wiley & Sons, New York, 2000.

[2] R. Mittra, C. H. Chan, and T. Cwik, "Techniques for Analysing Frequency Selective Surfaces - A Review," *Proc. IEEE*, vol. 76, pp. 1593-1615, 1988.

[3] G. M. Rebeiz, *RF MEMS: Theory, Design, and Thechnologie*, Wiley-Interscience, 1st Edition, June 2002.

[4] L. Latrach, N. Sboui, A. Gharsallah, A. Gharbi, and H. Baudrand, "Analysis and Design of a Planar Multilayered FSS with Arbitrary Incidence," *Applied Computational Electromagnetics Society (ACES) Journal*, vol. 23, no. 2, pp. 149-154, 2008.

[5] H. Oraizi and M. Afsahi, "Analysis of Planar Dielectric Multilayers as FSS by Transmission Line Transfer Matrix Method (TLTMM)," *Progress In Electromagnetics Research*, vol. 74, pp. 217-240, 2007.

[6] M. Hosseini, A. Pirhadi, and M. Hakkak, "A Novel AMC with Little Sensitivity to the Angle of Incidence Using 2-Layer Jerusalem Cross FSS," *Progress In Electromagnetics Research*, PIER 64, pp. 43-51, 2006.

[7] N. Sboui, A. Gharsallah, H. Baudrand, and A. Gharbi, "Design and Modeling of RF MEMS Switch by Reducing the Number of Interfaces," *Microwave and Optical Technology Letters*, vol. 4913, no. 5, pp. 1166-1170, May 2007.

[8] H-P. Tsai, Y. Wang, and T. Itoh, "An Unconditionally Stable Extended (USE) Finite-Element Time-Domain Solution of Active Nonlinear Microwave Circuits using Perfectly Matched Layers," *IEEE Trans. Microwave Theory and Techniques*, vol. 50, pp. 2226-2232, Oct. 2002.

[9] A. Abbaspour-Tarnijani, L. Dussopt, and G.M. Rebeiz, "A High Performance MEMS Miniature Tuneable Bandpass Filter," *IEEE MTT-S International Microwave Symposium Digest*, vol. 3, pp. 1785-1788, 2003.

[10] M. A. Habib, M. N. Jazi, A. Djaiz, M. Nedil, and T. A. Denidni, "Switched-Beam Antenna Based on EBG Periodic Structures," *Microwave Symposium Digest, IEEE MTT-S International*, 2009.

[11] N. Sboui. A. Gharsallah, H. Baudrand, and A. Gharbi, "Analysis of Double Loop Meander Line by using Iterative Process," *Micro. and Opt. Techn. Lett.*, vol. 26, no. 6, pp. 396-399, Sep. 2000.

[12] H. Baudrand, N. Raveu, N. Sboui, and G. Fontgalland, "Applications of Multiscale Waves Concept Iterative

Procedure," *Inter. Microw. and Opt. Conference*, Salvador, Brazil, October 29-November 1, 2007.

[13] L. Latrach, N. Sboui, A. Gharsallah, A. Gharbi, and Henri Baudrand, "Design and Modelling of Microwave Active Screen Using a Combination of the Rectangular and Periodic Waveguides Modes," *Journal of Electromagnetic Waves and Applications*, vol. 23, no. 11-12, pp. 1639-1648, 2009.

[14] M. A. Habib, M. N. Jazi, A. Djaiz, M. Nedil, and T. A. Denidni, "Switched-Beam Antenna Based on EBG Periodic Structures," *Microwave Symposium Digest, IEEE MTT-S International*, 2009.

[15] M. H. B. Ucar, A. Sondas, and Y. E. Erdemli, "Switchable Splitring Frequency Selective Surface," *Progress In Electromagnetics Research B*, vol. 6, pp. 65-79, 2008.

2012 INSTITUTIONAL MEMBERS

DTIC-OCP LIBRARY
8725 John J. Kingman Rd, Ste 0944
Fort Belvoir, VA 22060-6218

AUSTRALIAN DEFENCE LIBRARY
Northcott Drive
Canberra, A.C.T. 2600 Australia

BEIJING BOOK CO, INC
701 E Linden Avenue
Linden, NJ 07036-2495

DARTMOUTH COLLEGE
6025 Baker/Berry Library
Hanover, NH 03755-3560

DSTO EDINBURGH
AU/33851-AP, PO Box 830470
Birmingham, AL 35283

SIMEON J. EARL – BAE SYSTEMS
W432A, Warton Aerodome
Preston, Lancs., UK PR4 1AX

ENGINEERING INFORMATION, INC
PO Box 543
Amsterdam, Netherlands 1000 Am

ETSE TELECOMUNICACION
Biblioteca, Campus Lagoas
Vigo, 36200 Spain

GA INSTITUTE OF TECHNOLOGY
EBS-Lib Mail code 0900
74 Cherry Street
Atlanta, GA 30332

TIMOTHY HOLZHEIMER
Raytheon
PO Box 1044
Rockwall, TX 75087

HRL LABS, RESEARCH LIBRARY
3011 Malibu Canyon
Malibu, CA 90265

IEE INSPEC
Michael Faraday House
6 Hills Way
Stevenage, Herts UK SG1 2AY

INSTITUTE FOR SCIENTIFIC INFO.
Publication Processing Dept.
3501 Market St.
Philadelphia, PA 19104-3302

LIBRARY – DRDC OTTAWA
3701 Carling Avenue
Ottawa, Ontario, Canada K1A OZ4

LIBRARY of CONGRESS
Reg. Of Copyrights
Attn: 407 Deposits
Washington DC, 20559

LINDA HALL LIBRARY
5109 Cherry Street
Kansas City, MO 64110-2498

MISSOURI S&T
400 W 14^{th} Street
Rolla, MO 56409

MIT LINCOLN LABORATORY
Periodicals Library
244 Wood Street
Lexington, MA 02420

NATIONAL CHI NAN UNIVERSITY
Lily Journal & Book Co, Ltd
20920 Glenbrook Drive
Walnut, CA 91789-3809

JOHN NORGARD
UCCS
20340 Pine Shadow Drive
Colorado Springs, CO 80908

OSAMA MOHAMMED
Florida International University
10555 W Flagler Street
Miami, FL 33174

NAVAL POSTGRADUATE SCHOOL
Attn:J. Rozdal/411 Dyer Rd./ Rm 111
Monterey, CA 93943-5101

NDL KAGAKU
C/0 KWE-ACCESS
PO Box 300613 (JFK A/P)
Jamaica, NY 11430-0613

OVIEDO LIBRARY
PO BOX 830679
Birmingham, AL 35283

DAVID PAULSEN
E3Compliance
1523 North Joe Wilson Road
Cedr Hill, TX 75104-1437

PENN STATE UNIVERSITY
126 Paterno Library
University Park, PA 16802-1808

DAVID J. PINION
1122 E Pike Street #1217
SEATTLE, WA 98122

KATHERINE SIAKAVARA
Gymnasiou 8
Thessaloniki, Greece 55236

SWETS INFORMATION SERVICES
160 Ninth Avenue, Suite A
Runnemede, NJ 08078

YUTAKA TANGE
Maizuru Natl College of Technology
234 Shiroya
Maizuru, Kyoto, Japan 625-8511

TIB & UNIV. BIB. HANNOVER
DE/5100/G1/0001
Welfengarten 1B
Hannover, Germany 30167

UEKAE
PO Box 830470
Birmingham, AL 35283

UNIV OF CENTRAL FLORIDA
4000 Central Florida Boulevard
Orlando, FL 32816-8005

UNIVERSITY OF COLORADO
1720 Pleasant Street, 184 UCB
Boulder, CO 80309-0184

UNIVERSITY OF KANSAS –
WATSON
1425 Jayhawk Blvd 210S
Lawrence, KS 66045-7594

UNIVERSITY OF MISSISSIPPI
JD Williams Library
University, MS 38677-1848

UNIVERSITY LIBRARY/HKUST
Clear Water Bay Road
Kowloon, Honk Kong

CHUAN CHENG WANG
8F, No. 31, Lane 546
MingCheng 2nd Road, Zuoying Dist
Kaoshiung City, Taiwan 813

THOMAS WEILAND
TU Darmstadt
Schlossgartenstrasse 8
Darmstadt, Hessen, Germany 64289

STEVEN WEISS
US Army Research Lab
2800 Powder Mill Road
Adelphi, MD 20783

YOSHIHIDE YAMADA
NATIONAL DEFENSE ACADEMY
1-10-20 Hashirimizu
Yokosuka, Kanagawa,
Japan 239-8686

APPLIED COMPUTATIONAL ELECTROMAGNETICS SOCIETY JOURNAL
http://aces.ee.olemiss.edu

INFORMATION FOR AUTHORS

PUBLICATION CRITERIA

Each paper is required to manifest some relation to applied computational electromagnetics. **Papers may address general issues in applied computational electromagnetics, or they may focus on specific applications, techniques, codes, or computational issues.** While the following list is not exhaustive, each paper will generally relate to at least one of these areas:

1. **Code validation.** This is done using internal checks or experimental, analytical or other computational data. Measured data of potential utility to code validation efforts will also be considered for publication.

2. **Code performance analysis.** This usually involves identification of numerical accuracy or other limitations, solution convergence, numerical and physical modeling error, and parameter tradeoffs. However, it is also permissible to address issues such as ease-of-use, set-up time, run time, special outputs, or other special features.

3. **Computational studies of basic physics.** This involves using a code, algorithm, or computational technique to simulate reality in such a way that better, or new physical insight or understanding, is achieved.

4. **New computational techniques** or new applications for existing computational techniques or codes.

5. **"Tricks of the trade"** in selecting and applying codes and techniques.

6. **New codes, algorithms, code enhancement, and code fixes.** This category is self-explanatory, but includes significant changes to existing codes, such as applicability extensions, algorithm optimization, problem correction, limitation removal, or other performance improvement. **Note: Code (or algorithm) capability descriptions are not acceptable, unless they contain sufficient technical material to justify consideration.**

7. **Code input/output issues.** This normally involves innovations in input (such as input geometry standardization, automatic mesh generation, or computer-aided design) or in output (whether it be tabular, graphical, statistical, Fourier-transformed, or otherwise signal-processed). Material dealing with input/output database management, output interpretation, or other input/output issues will also be considered for publication.

8. **Computer hardware issues.** This is the category for analysis of hardware capabilities and limitations of various types of electromagnetics computational requirements. Vector and parallel computational techniques and implementation are of particular interest.

Applications of interest include, but are not limited to, antennas (and their electromagnetic environments), networks, static fields, radar cross section, inverse scattering, shielding, radiation hazards, biological effects, biomedical applications, electromagnetic pulse (EMP), electromagnetic interference (EMI), electromagnetic compatibility (EMC), power transmission, charge transport, dielectric, magnetic and nonlinear materials, microwave components, MEMS, RFID, and MMIC technologies, remote sensing and geometrical and physical optics, radar and communications systems, sensors, fiber optics, plasmas, particle accelerators, generators and motors, electromagnetic wave propagation, non-destructive evaluation, eddy currents, and inverse scattering.

Techniques of interest include but not limited to frequency-domain and time-domain techniques, integral equation and differential equation techniques, diffraction theories, physical and geometrical optics, method of moments, finite differences and finite element techniques, transmission line method, modal expansions, perturbation methods, and hybrid methods.

Where possible and appropriate, authors are required to provide statements of quantitative accuracy for measured and/or computed data. This issue is discussed in "Accuracy & Publication: Requiring, quantitative accuracy statements to accompany data," by E. K. Miller, *ACES Newsletter,* Vol. 9, No. 3, pp. 23-29, 1994, ISBN 1056-9170.

SUBMITTAL PROCEDURE

All submissions should be uploaded to ACES server through ACES web site (http://aces.ee.olemiss.edu) by using the upload button, journal section. Only pdf files are accepted for submission. The file size should not be larger than 5MB, otherwise permission from the Editor-in-Chief should be obtained first. Automated acknowledgment of the electronic submission, after the upload process is successfully completed, will be sent to the corresponding author only. It is the responsibility of the corresponding author to keep the remaining authors, if applicable, informed. Email submission is not accepted and will not be processed.

EDITORIAL REVIEW

In order to ensure an appropriate level of quality control, papers are peer reviewed. They are reviewed both for technical correctness and for adherence to the listed guidelines regarding information content and format.

PAPER FORMAT

Only camera-ready electronic files are accepted for publication. The term **"camera-ready" means that the material is neat, legible, reproducible, and in accordance with the final version format listed below.**

The following requirements are in effect for the final version of an ACES Journal paper:

1. The paper title should not be placed on a separate page.

The title, author(s), abstract, and (space permitting) beginning of the paper itself should all be on the first page. The title, author(s), and author affiliations should be centered (center-justified) on the first page. The title should be of font size 16 and bolded, the author names should be of font size 12 and bolded, and the author affiliation should be of font size 12 (regular font, neither italic nor bolded).

2. An abstract is required. The abstract should be a brief summary of the work described in the paper. It should state the computer codes, computational techniques, and applications discussed in the paper (as applicable) and should otherwise be usable by technical abstracting and indexing services. The word "Abstract" has to be placed at the left margin of the paper, and should be bolded and italic. It also should be followed by a hyphen (—) with the main text of the abstract starting on the same line.

3. All section titles have to be centered and all the title letters should be written in caps. The section titles need to be numbered using roman numbering (I. II. ….)

4. Either British English or American English spellings may be used, provided that each word is spelled consistently throughout the paper.

5. Internal consistency of references format should be maintained. As a guideline for authors, we recommend that references be given using numerical numbering in the body of the paper (with numerical listing of all references at the end of the paper). The first letter of the authors' first name should be listed followed by a period, which in turn, followed by the authors' complete last name. Use a coma (,) to separate between the authors' names. Titles of papers or articles should be in quotation marks (" "), followed by the title of journal, which should be in italic font. The journal volume (vol.), issue number (no.), page numbering (pp.), month and year of publication should come after the journal title in the sequence listed here.

6. Internal consistency shall also be maintained for other elements of style, such as equation numbering. Equation numbers should be placed in parentheses at the right column margin. All symbols in any equation have to be defined before the equation appears or right immediately following the equation.

7. The use of SI units is strongly encouraged. English units may be used as secondary units (in parentheses).

8. Figures and tables should be formatted appropriately (centered within the column, side-by-side, etc.) on the page such that the presented data appears close to and after it is being referenced in the text. When including figures and tables, all care should be taken so that they will appear appropriately when printed in black and white. For better visibility of paper on computer screen, it is good to make color figures with different line styles for figures with multiple curves. Colors should also be tested to insure their ability to be distinguished after black and white printing. Avoid the use of large symbols with curves in a figure. It is always better to use different line styles such as solid, dotted, dashed, etc.

9. A figure caption should be located directly beneath the corresponding figure, and should be fully justified.

10. The intent and meaning of all text must be clear. For authors who are not masters of the English language, the ACES Editorial Staff will provide assistance with grammar (subject to clarity of intent and meaning). However, this may delay the scheduled publication date.

11. Unused space should be minimized. Sections and subsections should not normally begin on a new page.

ACES reserves the right to edit any uploaded material, however, this is not generally done. It is the author(s) responsibility to provide acceptable camera-ready files in pdf and MSWord formats. Incompatible or incomplete files will not be processed for publication, and authors will be requested to re-upload a revised acceptable version.

COPYRIGHTS AND RELEASES

Each primary author must execute the online copyright form and obtain a release from his/her organization vesting the copyright with ACES. Both the author(s) and affiliated organization(s) are allowed to use the copyrighted material freely for their own private purposes.

Permission is granted to quote short passages and reproduce figures and tables from and ACES Journal issue provided the source is cited. Copies of ACES Journal articles may be made in accordance with usage permitted by Sections 107 or 108 of the U.S. Copyright Law. This consent does not extend to other kinds of copying, such as for general distribution, for advertising or promotional purposes, for creating new collective works, or for resale. The reproduction of multiple copies and the use of articles or extracts for commercial purposes require the consent of the author and specific permission from ACES. Institutional members are allowed to copy any ACES Journal issue for their internal distribution only.

PUBLICATION CHARGES

All authors are allowed for 8 printed pages per paper without charge. Mandatory page charges of $75 a page apply to all pages in excess of 8 printed pages. Authors are entitled to one, free of charge, copy of the printed journal issue in which their paper was published. Additional reprints are available for $ 50. Requests for additional re-prints should be submitted to the managing editor or ACES Secretary.

Corresponding author is required to complete the online form for the over page charge payment right after the initial acceptance of the paper is conveyed to the corresponding author by email.

ACES Journal is abstracted in INSPEC, in Engineering Index, DTIC, Science Citation Index Expanded, the Research Alert, and to Current Contents/Engineering, Computing & Technology.